

DIRECT NUMERICAL SIMULATION OF GAS
TRANSFER AT THE AIR-WATER INTERFACE
IN A BUOYANT-CONVECTIVE FLOW
ENVIRONMENT

A thesis submitted for the degree of Doctor of Philosophy

by

BORIS KUBRAK

School of Engineering and Design Brunel University February 2014

Abstract

The gas transfer process across the air-water interface in a buoyant-convective environment has been investigated by Direct Numerical Simulation (DNS) to gain improved understanding of the mechanisms that control the process. The process is controlled by a combination of molecular diffusion and turbulent transport by natural convection. The convection when a water surface is cooled is combination of the Rayleigh-Bénard convection and the Rayleigh-Taylor instability. It is therefore necessary to accurately resolve the flow field as well as the molecular diffusion and the turbulent transport which contribute to the total flux. One of the challenges from a numerical point of view is to handle the very different levels of diffusion when solving the convection-diffusion equation. The temperature diffusion in water is relatively high whereas the molecular diffusion for most environmentally important gases is very low. This low molecular diffusion leads to steep gradients in the gas concentration, especially near the interface. Resolving the steep gradients is the limiting factor for an accurate resolution of the gas concentration field. Therefore a detailed study has been carried out to find the limits of an accurate resolution of the transport for a low diffusivity scalar.

This problem of diffusive scalar transport was studied in numerous 1D, 2D and 3D numerical simulations. A fifth-order weighted non-oscillatory scheme (WENO) was deployed to solve the convection of the scalars, in this case gas concentration and temperature. The WENO-scheme was modified and tested in 1D scalar transport to work on non-uniform meshes. To solve the 2D and 3D velocity field the incompressible Navier-Stokes equations were solved on a staggered mesh. The convective terms were solved using a fourth-order accurate kinetic energy conserving discretization while the diffusive terms were solved using a fourth-order central method. The diffusive terms were discretized using a fourth-order central finite difference method for the second derivative. For the time-integration of the velocity field a second-order Adams-Bashworth method was employed. The Boussinesq approximation was employed to model the buoyancy due to temperature differences in the water. A linear relationship between temperature and density was assumed. A mesh sensitivity study

found that the velocity field is fully resolved on a relatively coarse mesh as the level of turbulence is relatively low. However a finer mesh for the gas concentration field is required to fully capture the steep gradients that occur because of its low diffusivity. A combined dual meshing approach was used where the velocity field was solved on a coarser mesh and the scalar field (gas concentration and temperature) was solved on an overlaying finer sub-mesh. The velocities were interpolated by a second-order method onto the finer sub-mesh. A mesh sensitivity study identified a minimum mesh size required for an accurate solution of the scalar field for a range of Schmidt numbers from $Sc = 20$ to $Sc = 500$. Initially the Rayleigh-Bénard convection leads to very fine plumes of cold liquid of high gas concentration that penetrate the deeper regions. High concentration areas remain in fine tubes that are fed from the surface. The temperature however diffuses much stronger and faster over time and the results show that temperature alone is not a good identifier for detailed high concentration areas when the gas transfer is investigated experimentally. For large timescales the temperature field becomes much more homogeneous whereas the concentration field stays more heterogeneous. However, the temperature can be used to estimate the overall transfer velocity K_L . If the temperature behaves like a passive scalar a relation between Schmidt or Prandtl number and K_L is evident.

A qualitative comparison of the numerical results from this work to existing experiments was also carried out. Laser Induced Fluorescence (LIF) images of the oxygen concentration field and Schlieren photography has been compared to the results from the 3D simulations, which were found to be in good agreement. A detailed quantitative analysis of the process was carried out. A study of the horizontally averaged convective and diffusive mass flux enabled the calculation of transfer velocity K_L at the interface. With K_L known the renewal rate r for the so called surface renewal model could be determined. It was found that the renewal rates are higher than in experiments in a grid stirred tank. The horizontally averaged mean and fluctuating concentration profiles were analysed and from that the boundary layer thickness could be accurately monitored over time. A lot of this new DNS data obtained in this research might be inaccessible in experiments and reveal previously unknown details of the gas transfer at the air water interface.

Contents

1	Introduction	1
1.1	Background	1
1.2	Objective and the numerical challenges	3
1.3	Methodology	5
2	Theoretical Background & Literature Review	7
2.1	Fundamental Concepts	7
2.2	Governing Equations	8
2.2.1	Mass Transfer	8
2.2.2	Transfer velocity K_L	8
2.2.3	Important non-dimensional parameters	9
2.3	Conceptual models for the Transfer velocity (K_L)	10
2.4	Numerical investigations of scalar transfer at air-water interfaces	12
2.4.1	Wind-shear-induced flows	13
2.4.2	Bottom-shear-induced flows	16
2.4.3	Buoyant-convective-induced flows	19
2.5	Experimental investigations of gas transfer processes	22
2.5.1	Wind-shear-induced flows	22
2.5.2	Bottom-sheared-induced flows	23
2.5.3	Buoyant-convective-induced flows	24
2.6	WENO schemes	25

3	Numerical Method	27
3.1	Governing equations	27
3.1.1	The Navier-Stokes equations	28
3.1.2	The convection-diffusion equation of the scalar φ	29
3.2	The non-dimensionalization	29
3.3	Physical Assumptions	32
3.4	Flow Solver	33
3.5	Discretization of the convection-diffusion equation of the scalar φ with WENO scheme	38
3.6	Dual Mesh Approach	41
3.7	Implementation of Boundary Conditions	42
3.8	Parallelization	43
4	Numerical Experiments	46
4.1	1D Numerical Experiments	47
4.1.1	Scalar transport by convection on a uniform grid	47
4.1.2	Scalar transport by convection on non-uniform meshes	49
4.1.3	Scalar transport: pure diffusion	50
4.2	Two dimensional sheared scalar distribution	52
4.3	Two-dimensional low-diffusivity scalar transport in buoyancy driven flow	54
4.3.1	Comparison of scalar convection methods in 2D	56
4.3.2	Mesh sensitivity test : Flow-field	58
4.3.3	Mesh sensitivity test: gas concentration field	59
5	Simulations in a 3D domain	64
5.1	Boundary and Initial Conditions	65
5.2	Results and Discussion	66
5.2.1	Qualitative Mesh Sensitivity of 3D Gas Concentration Field	66
5.2.2	3D isosurfaces	69
5.2.3	Temperature and Convective Vertical Gas Flux Relation	73

5.2.4	Transfer Velocity K_L	76
5.2.5	Renewal rates and transfer Velocity (K_L)	80
5.2.6	Total Gas Concentration	81
5.2.7	Heat Transfer	82
5.2.8	Convective cell pattern merging	83
5.2.9	Vorticity	89
5.2.10	Mean and fluctuating concentration	93
5.2.11	Boundary Layer Thickness	95
5.3	Comparison to Experiments	101
5.3.1	Concentration Field	102
5.3.2	Temperature Field	104
6	Conclusions and Recommendations	110
6.1	Conclusions	110
6.2	Recommendations for further studies	114

List of Figures

1.1	Schematic illustration of the turbulence mechanisms driving gas transfer at the air-water interface in the environment. Type A is investigated in this study [38].	2
2.1	principal conditions of wind-shear driven flows	14
2.2	Flow regime for sheared wavy interfaces [56]	15
2.3	Bottom-sheared channel flow	17
3.1	Variables on a staggered mesh [96].	35
3.2	Schematic illustration of the weighted 5 point convex combination composed of three 3-points stencils S_0, S_1, S_2 and their respective weights a_0, a_1, a_2 used in the classical WENO5 scheme. [82].	40
3.3	Variables on the new dual mesh. The flow field is solved on the outer coarse mesh, whilst the scalar is computed on a refined subgrid. For the transport of the scalar the velocities are interpolated onto the midpoints of the subgrid	42
3.4	Schematic parallelization procedure	44
4.1	The sine wave used for 1D convection test on a 10-point mesh	48
4.2	A detail of the sheared scalar distribution. a) at $t=0$ second and b) at $t=1.1$ seconds.	53
4.3	Schematic representation of the computational domain. The scatter shows every 10^{th} grid line of the major grid used for the velocity field. The mesh for the scalar was further refined by factors of $R = 2, 3$ and 5	55

4.4	Comparison of WENO5 schemes (JS2, JS3, LOC) and the fifth-order central scheme (C5), showing profiles of the scalar distribution φ at $z = 4.5\text{cm}$ and $t = 45$ seconds using a Schmidt number of $Sc = 500$	57
4.5	A grid refinement showed that the velocity field is fully resolved on a 400×256 grid.	58
4.6	Comparison of the gas concentration field after $t = 45$ seconds on standard mesh $n_x = 400$ and $n_z = 256$ and with a dual subgrid in place three times as fine (see Fig. 3.3c). The gas concentration field is resolved in sharper detail with less smearing.	60
4.7	Comparison of scalar field after $t = 45$ seconds on different levels of subgrid mesh refinement. The two locations are vertical lines at $x = 2.0L$ and $x = 1.3L$ along the downwards plumes as seen on Fig. 4.6a.	61
4.8	Comparison of scalar field after $t = 45$ seconds on different levels of subgrid mesh refinement. The location is a horizontal line at various depths z across the downwards plumes as seen on Fig. 4.6d and 4.6c.	62
4.9	Comparison of the total non-dimensional scalar concentration and temperature T^* over time for different levels of subgrid refinement	63
5.1	Schematic of the 3D domain	65
5.2	Contour plots of gas concentration	68
5.3	Sequence of isosurfaces of 25% gas concentration viewed from below	70
5.4	Sequence of isosurfaces of 25% gas concentration viewed from above	71
5.5	Comparison of isosurfaces of 25% gas concentration (left) and temperature (right)	72
5.6	Comparison of vertical flux and temperature at horizontal planes after 50 seconds	75
5.7	K_L over time	77
5.8	Schmidt number scaling for K_L at $t = 90s$	78
5.9	Vertical Convective and Diffusive Mass Fluxes at $t = 90s$ below the interface	78

5.10	Power scaling for K_L over time	79
5.11	Surface renewal rates r over time	81
5.12	Volume integral of φ over time	82
5.13	K_L versus Thermal Heat flux \dot{q}	84
5.14	K_L versus Thermal Heat flux \dot{q}	84
5.15	velocity magnitude at interface in 4 second intervals in cm/s	86
5.16	velocity vectors at interface in 4 second intervals	87
5.17	temperature plot 1 mm below interface	88
5.18	vorticity magnitude at $y = 2.5cm$ in 4 second intervals	90
5.19	vorticity magnitude on 25% isosurface in 4 second intervals	91
5.20	average vorticity magnitude over time; total and in plane sections near the interface	92
5.21	sequence of vertical mean and fluctuating concentration profiles	94
5.22	definition of the boundary layer thickness	96
5.23	boundary layer thickness over time	97
5.24	unscaled fluctuations at $t = 37.5s$	98
5.25	Definition of the isosurface thickness δ_{iso}	99
5.26	depth δ_{iso} plotted on the isosurface	100
5.27	Minimum and average δ_{iso} over time for $Sc = 500$	101
5.28	Comparison of flow structures. High oxygen concentration plumes of LIF measurements conducted by Jirka et al. [46] (Fig. 5.28a) and DNS results (Fig. 5.28b). The dark and light colour scaling indicate regions with high and low scalar concentration, respectively. In both cases the surface temperature was 3°C colder than the bulk temperature.	103
5.29	comparison of gas concentration boundary layer just at the beginning of the convection. Numerical results (left), Experimental results conducted by Jirka et al. [46] (right).	104
5.30	Principle of Schlieren Photography	105

5.31 Comparison of (a) experimental Schlieren photographs and (b) numerical results of temperature field.	107
5.32 Comparison of (a) experimental Schlieren photographs and (b) numerical results of temperature field.	108

List of Tables

4.1	Absolute error and order of convergence on uniform meshes with $\varepsilon = 10^{-6}$. . .	49
4.2	Absolute error and order of convergence on uniform meshes with $\varepsilon = 1$	50
4.3	Absolute error and order of convergence on non-uniform meshes with $\varepsilon = 10^{-6}$. . .	51
4.4	Absolute error and order of convergence on non-uniform meshes for pure dif- fusion case.	52
4.5	Absolute error and order of convergence resulting from the 2D sheared scalar distribution test on uniform meshes using the WENO scheme of Liu et al. [61] with $\varepsilon = 10^{-6}$	54
4.6	The time difference found between the development of disturbances.	56

Nomenclature

α	Thermal diffusivity
δ	Concentration Boundary Layer Thickness
δ_s	stretching parameter for non uniform meshes
δ_{iso}	Depth of Isosurface
\dot{q}	Heat Flux [J/s]
Γ	Diffusion coefficient for mass diffusion
Γ_T	Diffusion coefficient for temperature diffusion
μ	dynamic viscosity
ν	kinematic viscosity
ω	Vorticity
$\bar{\varphi}$	spatially horizontal mean concentration
ρ	Density
φ	gas concentration in the field
φ^*	non-dimensional gas concentration in the field
$\varphi_{B,0}$	gas concentration in the bulk

φ_s	gas concentration boundary condition at the interface
ξ	vertical flux velocity
A_{int}	Area of interface
$C_{x,y,z}(u, v, w)$	Convective terms
D	Mass diffusivity
d_c	Diffusion coefficient for Fick's law
$D_{x,y,z}(u, v, w)$	Diffusive terms (for velocity diffusion)
g	gravity = $9.81[\frac{m}{s^2}]$
g'	reduced gravity
Gr	Grashof number
J	Mass Flux
k	thermal conductivity
K_L	transfer velocity
L	characteristic length-scale $[L] = cm$
n	time step
p	Pressure
Pr	Prandtl number
R	factor for dual mesh refinement
Ra	Rayleigh number
Ra_c	critical Rayleigh number ≈ 657
Sc	Schmidt number

T	Temperature
t	time unit $[t] = L/U = s$
T^*	non-dimensional temperature
$T_{B,0}$	Temperature in the bulk
T_{ran}	random temperature magnitude
T_s	Temperature at the interface
U	characteristic velocity scale $[U] = \frac{cm}{s}$
u	horizontal velocity component in x -direction
v	horizontal velocity component in y -direction
w	vertical velocity component in z -direction
x	spatial horizontal variable
y	spatial horizontal variable
z	spatial vertical variable

Acronyms

AWF Analytical Wall-Function

CFD Computational Fluid Dynamics

CFL CourantFriedrichsLewy

DNS Direct Numerical Simulation

ENO Essentially Non-Oscillatory

LES Large Eddy Simulation

LIF Laser-induced Fluorescence

MPI Message Passing Interface

PIV Particle Image Velocimetry

RANS Reynolds averaged Navier-Stokes Simulation

RB Rayleigh-Bénard

WENO Weighted Essentially Non-Oscillatory

Acknowledgments

Foremost, I would like to express my sincere gratitude and appreciation to my advisor Dr Jan G. Wissink for the continuous support, guidance, immense knowledge and encouragement during my research. I could have not have imagined to have a better advisor and mentor. I also wish to thank my co-advisors, Dr Tze Pei Chong and Dr Mark Jabbal.

I wish to thank Dr Xi Jiang for initial support to secure an Isambard Scholarship from Brunel University to fund this research. Special thanks go to Dr Herlina from the Karlsruhe Institute of Technology for her great support. Her connections to the Leibniz Supercomputer Centre in Munich provided an excellent platform to perform computational simulations on such a scale. I also like to thank Friedrich Greve and my fellow PhD students at Brunel University for their support and friendship during this research.

I am deeply grateful to my family and friends for their loving support and constant encouragement throughout the time that this work was in progress.

Chapter 1

Introduction

1.1 Background

THE gas transfer through the air-water interface plays an important role in environmental and chemical engineering. One typical process is the absorption of oxygen into natural water bodies such as lakes and oceans. It is vital to sustain aquatic life. Oxygen enters the water through the air-water interface and dissolved oxygen is subsequently distributed through the water. This process is controlled by interaction of molecular diffusion and turbulent transport. The level of molecular diffusion is very low for soluble gases contained in air (i.e. oxygen and carbon dioxide). The turbulent diffusion depends on the flow characteristics. In the case of convectively driven flow, for small temperature differences the flow is predominantly laminar. It is well known that the level of turbulence plays an important role in the gas transfer process and is the dominant driving mechanism. Natural sources of turbulence can be classified into three major types which are surface-shear-induced turbulence (e.g. wind shear on open waters), bottom-shear-induced turbulence (e.g. in rivers) and buoyant-convective turbulence (e.g. in lakes due to surface cooling). Fig 1.1 shows a schematic illustration of the turbulence sources and their interaction [38]. Wind-shear and bottom-shear driven turbulence has been investigated numerically in a number of studies [34, 35, 79, 23]. In those cases the level of turbulence is high and the influence of the water temperature is not considered.

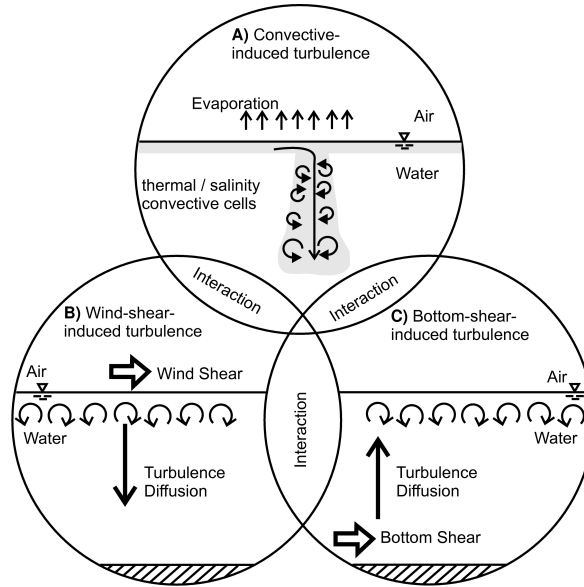


Figure 1.1: Schematic illustration of the turbulence mechanisms driving gas transfer at the air-water interface in the environment. Type A is investigated in this study [38].

There is relatively little known about the detailed physical mechanisms of convectively driven gas transfer. If the surface layer is cooled it becomes slightly heavier than the water underneath triggering a Rayleigh instability resulting in a downwards penetration of the upper layer that is saturated with gas. Typical non-dimensional quantities characterising the gas transfer are the ratio of the momentum diffusivity and mass diffusivity, represented by the Schmidt number Sc , the ratio of viscosity and thermal diffusivity, represented by the Prandtl number Pr and the Rayleigh number Ra . The convection is obviously driven by temperature differences within the water body introduced from the cooled free surface on the top. The temperature diffusion, however, is much higher than the relatively low molecular diffusion of the gas. The thickness of the thermal and concentration boundary layer is very different. For environmentally important gases such as O_2 , N_2 , CO_2 the Schmidt number is $Sc \approx 500$. This results in a concentration boundary layer of only ten to hundreds of μm thickness. This makes experimental measurements at the interface very difficult. Quantities of interest such as the gas concentration or the mass flux are very difficult to measure in great detail. Researchers tried to visualize and measure the oxygen concentration field with

fluorescence methods (Jirka et al. [46], Schladow et al. [78]), however the resolution remains a problem. The objective of this study is to gain a more detailed understanding of the mechanisms that control the oxygen absorption in water dominated by convectively-induced turbulence on a scale where experimental measurements of the gas concentration field are nearly impossible. Detailed high resolution Direct Numerical Simulation is required to gain an improved knowledge of the transfer and distribution of dissolved gas in convectively driven flow.

1.2 Objective and the numerical challenges

The gas transfer across the air-water interface represents a scalar convection-diffusion problem. Let the gas concentration be represented by a scalar φ . A combination of two physical mechanisms contribute to the transport of the gas through the system (the water body). These two processes are convection and diffusion. Convection arises simply from the motion of the fluid. A fluid particle with a certain gas concentration is simply moved along by the flow. On the other hand there is the process of (molecular) diffusion. Even if the fluid were completely stationary there would still be a mass transfer into the fluid by means of diffusion. In one dimension this combination of convection and diffusion of a scalar φ can be described by the 1D linear convection-diffusion equation,

$$\frac{\partial \varphi}{\partial t} + w \frac{\partial \varphi}{\partial z} = \Gamma \left(\frac{\partial^2 \varphi}{\partial z^2} \right). \quad (1.1)$$

The convective term $w \frac{\partial \varphi}{\partial z}$ on the left hand side arises because of the presence of the velocity w . The diffusive term $\Gamma \left(\frac{\partial^2 \varphi}{\partial z^2} \right)$ on the right hand side is essentially Fick's second law of diffusion that states that describes the concentration change with time caused by diffusion.

$$\frac{\partial \varphi}{\partial t} = d_c \left(\frac{\partial^2 \varphi}{\partial z^2} \right). \quad (1.2)$$

The term d_c in Fick's second law above is the diffusion coefficient or diffusivity. It is a measure for the resistance of the substance (here the water) against the diffusion of a scalar

quantity φ (let this be gas concentration or temperature). The diffusion coefficient in (1.1) is $d_c = \Gamma = \frac{1}{ReSc}$ (where Re is the Reynolds number and Sc is the Schmidt number, see Section 3.2). The higher the Schmidt numbers become the weaker the diffusion gets which leads to a thinner concentration boundary layer as mentioned in Section 1.1. For the temperature, T , the same equation is valid with the Schmidt number, Sc , replaced by the Prandtl number, Pr , (see Section 3.2 for definition of Sc and Pr). For the diffusion of most soluble gases (such as oxygen) into water the Schmidt number is $Sc \approx 500$. This leads to a very low diffusion of the gas concentration. As a result, very high concentration areas will be in close proximity to low concentration areas with a steep gradient between them. Hence the concentration level might jump from 0% to 100% over just a few gridpoints. Furthermore, the gas concentration field moves by means of (scalar) convection. To capture accurately the advancing steep gradient 'fronts' with high resolution is *the main* numerical challenge. The low level of mass diffusivity requires a numerical method that is capable of capturing the steep gradients only within a couple of gridpoints without losing accuracy because of numerical error or smearing.

The diffusion of the gas concentration is also influenced by the level of turbulence. For instance a small eddy would transfer a fluid particle quickly elsewhere and, if located in an area between high and low gas concentration, enhance the mixing. However the level of turbulence is relatively low in a convectively driven flow. One can imagine that if a lake's surface cools down at night, causing natural convection, the motion of the water is much less turbulent than for example in a river with bottom-shear (see Fig. 1.1). In fact the flow can be considered laminar if the surface is cooled by only a few degrees °C. The smallest flow structures are significantly larger than the smallest structures in the scalar field (i.e. thickness of gas concentration boundary layer). Considering that the temperature dependent density drives the flow it becomes evident that there is a coupling between the scalar field and the velocity field. The difference in diffusive length scales for the velocity field and scalar concentration field imposes different resolution requirements to the problem. Whilst the flow field might be fully resolved on a certain grid size the scalar field might be underresolved.

The nature of the mass transfer over an interface entails the fact that important mech-

anism happen near the interface itself. The scalar diffusive transport is determined by the gradients present in the scalar field (Fick's law). On the other hand the structure of the velocity field near the interface determines the convective transport of the scalar φ within the boundary layer. The formation of the concentration and temperature boundary layer (which will also scale very differently) and their different gradients are crucial processes. It is therefore necessary to pay special attention to the resolution of the near interface region by refining the numerical grid near the interface. This means that the numerical methods need to be accurate on non-uniform meshes.

In summary the numerical challenges outlined above are

- to resolve the convective transport of the low-diffusive scalar field containing very steep gradients without smearing or oscillations,
- the different scaling of velocity and scalar field,
- the presence of a non-uniform refined mesh near the interface.

1.3 Methodology

As mentioned in Section 1.2 the main numerical challenge is the convective transport of a scalar field containing steep gradients. This problem is addressed by the deployment of a weighted non-oscillatory (WENO) scheme to discretize the scalar convection. The development of WENO schemes began with Harten's ENO scheme (essentially non-oscillatory) in 1987 [32] (see literature review Chapter 2). Up to now a variety of WENO schemes has been developed. They are based on the idea of taking a weighted combination of interpolation polynomials to replicate a discontinuity or sudden change in the solution. This constructed 'step function' than allows to predict the location of the step when it is moved. A discontinuity or step function could also be captured with spectral methods using, for instance, Fourier series expansions. Such highly accurate methods, however, may lead to spontaneous oscillations occurring near steep gradients (Gibbs phenomenon). The advantage of the WENO schemes is the steep-gradient capturing capability without exhibiting oscillations or wiggles.

The different resolution requirements of velocity field and scalar field are addressed with a dual meshing strategy. Here the velocity field is solved on a coarser mesh than the scalar field. The velocity field is solved by a finite-difference discretization of the convective terms using a fourth-order unconditionally kinetic energy conserving method combined with a fourth-order accurate central method for the diffusive terms [96]. The 2D incompressible Navier-Stokes equation is discretized on a non-uniform, staggered mesh in combination with a second-order accurate Adams-Bashforth time integration. The velocities are then interpolated onto the finer grid, where the transport of the scalar field is resolved by a fourth-order interpolation. This dual meshing strategy improves the computational efficiency. The mesh for the scalar field could be refined to various levels *without* more computational effort to solve the velocity field. It is the unique steep gradient capturing capability of the WENO scheme and the dual meshing approach to separate the solving of the velocity field and the scalar field that sets this numerical method apart from commercially available codes and gives it its high order of accuracy. The common scalar convection-diffusion problems to be solved with commercial codes in industrial applications are heat transfer in a single phase flow where the Prandtl/Schmidt number is usually below 10. Such high diffusivity can be resolved with ordinary gradient reconstructions, hence commercial codes are lacking an advanced gradient reconstruction method such as the WENO schemes. A detailed description of the numerical method can be found in Chapter 3.

Chapter 2

Theoretical Background & Literature Review

THE theoretical background on gas exchange at air-water interfaces is provided in the first part of this chapter, providing fundamental concepts and some governing equations. The following sections review literature on investigations in the laboratory, in field studies, and numerical simulations. Special focus has been put on the numerical studies and the methods used. Numerical work featuring different physical conditions such as shear-driven flow and wavy interfaces are reviewed. A review on experimental investigations as well as WENO schemes is given.

2.1 Fundamental Concepts

The gas transfer process at the air-water interface with low soluble gases (such as Oxygen) is controlled by resistance on the liquid side. If the liquid is stationary without any disturbances molecular diffusion governs the process. In natural cases, however, the fluid may be in motion by a combination, or exclusively, of wind-shear, bottom shear or buoyant convection due to surface cooling (see figure 1.1). The fluid motion introduces convective mass transfer, so that the process becomes a combination of convection and diffusion. Near the interface molecular diffusion dominates whereas further away from the interface the convective transport is

dominant. In the case of convective instability, that is studied in this work, the interaction of gravity with thermal effects on density are driving the flow and the subsequent mixing enhances the convective mass transfer. For convective instability to occur the buoyancy effect has to be dominant and overcome the viscous forces. Liquid at the surface cools and becomes heavier than a light warm layer below, thus it has a tendency to move downwards and to be replaced by warmer liquid from the lower layer.

2.2 Governing Equations

2.2.1 Mass Transfer

In Section 1.2 Fick's law is stated which describes the mass flux of a solute due to molecular diffusion. Let the solute be the scalar quantity φ then Fick's second law in one dimensional form can be written as,

$$J = -d_c \frac{\partial^2 \varphi}{\partial z^2}. \quad (2.1)$$

The minus sign in (2.1) indicates that the flux is from high concentration to low concentration in the vertical z -direction. Taking advection (the moving fluid) and the conservation of mass also into consideration, the unsteady mass flux J reads

$$J = w \frac{\partial \varphi}{\partial z} + (-d_c \frac{\partial^2 \varphi}{\partial z^2}) \quad (2.2)$$

where t is the time and w is the instantaneous velocity vector w in z -direction. The first term on the right describes the convective transport and the second term the molecular diffusion process in the vertical direction.

2.2.2 Transfer velocity K_L

The gas transfer rate is usually parameterized by the transfer velocity K_L . Based on the empirical argument that the mass transfer is proportional to the concentration difference the common definition is,

$$K_L = \frac{j}{\Delta c} \quad (2.3)$$

where j is the mass flux rate and Δc is the concentration difference between bulk region and interface. Applying equation (2.2) for the mass flux of a scalar φ equation (2.3) can be written as,

$$K_L = \frac{J}{\Delta\varphi^*} = \frac{J}{\varphi_s^* - \varphi_b^*} \quad (2.4)$$

where φ_s^* is the saturated concentration and φ_b^* is the bulk concentration. Considering a low soluble gas to be transferred the normalized bulk concentration stays at $\varphi_b^* \approx 0$. Using the normalized concentration it is evident that $\Delta\varphi^* \approx 1$ and hence $K_L \approx J$.

2.2.3 Important non-dimensional parameters

The gas transfer process in a convective flow environment can be described by non-dimensional parameters. These relate to the three main physical processes which are involved namely, mass transfer, heat transfer, and buoyant convection. The Schmidt number Sc is defined as the ratio of momentum diffusivity ν to mass diffusivity D , hence

$$Sc = \frac{\nu}{D}. \quad (2.5)$$

The Schmidt number relates the relative thickness of the hydrodynamic boundary layer and the mass-transfer boundary layer. Based on similar principles the Prandtl number Pr is the ratio of momentum diffusivity ν and thermal diffusivity α ,

$$Pr = \frac{\nu}{\alpha} \quad (2.6)$$

relating the relative thickness of the hydrodynamic boundary layer and the thermal boundary layer. Because of the similar concept of Pr and Sc the Schmidt number Sc is sometimes called 'mass transfer Prandtl number' in the literature.

Buoyancy driven flows can be characterized by the Rayleigh number Ra which is a product of the Grashof number Gr and the Prandtl number Pr .

$$Ra = GrPr = \frac{\Delta\rho g L^3}{\alpha\mu} \quad (2.7)$$

where $\Delta\rho$ is the density difference of the fluid between the two temperatures T_B and T_0 and μ is the dynamic viscosity and g is gravity. The Rayleigh number basically is the ratio of buoyancy forces and viscosity forces times the ratio of momentum and thermal diffusivities. A further detailed description on how these and other parameters are used for the non-dimensionalization of the numerical method is given in Section 3.2.

The Nusselt number Nu quantifies the heat transfer across a boundary. It is the ratio of the convective heat flux and conductive heat flux.

$$Nu = \frac{\dot{q}_{conv}}{\dot{q}_{cond}}. \quad (2.8)$$

The conductive heat flux \dot{q}_{cond} in (2.8) is the heat flux which is present when the fluid is stationary and the only mode of heat transfer is conduction (diffusion). The convective heat flux \dot{q}_{conv} in (2.8) is the total heat flux when the fluid is in motion including both, advection and diffusion.

In similar fashion the mass transfer is quantified by the Sherwood number Sh

$$Sh = \frac{J_{conv}}{J_{diff}} \quad (2.9)$$

where J_{conv} and J_{diff} are the convective and diffusive mass flux, respectively.

2.3 Conceptual models for the Transfer velocity (K_L)

There have been efforts to describe the transfer velocity K_L with models. So called *conceptual models* are “simple solutions of the vertically one-dimensional diffusion equation without any explicit advective flow field. The effects of advection are incorporated by initial and boundary conditions, which are characterized by time and spatial scales ”[13]. The following gives an overview over the most common conceptual models.

Film model

The first conceptual model was developed by Lewis and Whitman [59] who assumed a linear profile in the concentration boundary layer. Hence the linear relation

$$K_L = \frac{D}{\delta}. \quad (2.10)$$

was assumed where D is the molecular diffusivity and δ is the boundary layer thickness. D is also often referred as the Gas Diffusion Coefficient (usually in cm^2/s). The film model oversimplifies the actual mechanism as it is clear there are no flow characteristics or time scales considered. In numerical experiments it could be found that the relation between K_L and D is not linear [65]. It might be a good estimate for processes where diffusion is the dominant mechanism.

Penetration model

Higbie [42] introduced the concept of the so called 'surface renewal effect', which is based on the idea that the motion in the bulk region of the fluid would bring packages of 'fresh' fluid to the surface. This takes place at a certain renewal time t_r . Higbie showed that

$$K_L = \sqrt{\frac{D}{\pi t_r}}. \quad (2.11)$$

Surface renewal model

Dankwerts [21] modified the penetration model by introducing the renewal rate r where t_r follows an exponential probability distribution. He derived

$$K_L = \sqrt{Dr}. \quad (2.12)$$

where $1/r$ can be interpreted as the mean time between surface renewal events.

Film-renewal model

O'Connor and Dobbins [75] combined the linear film model with Dankwert's model. They proposed

$$K_L = \sqrt{Dr} \coth \left[\frac{\delta}{\sqrt{D/r}} \right] \quad (2.13)$$

which is asymptotic to the film model for small values of r and the surface renewal model for large values of r .

Random eddy model

Harriott [31] developed the random eddy model which suggests that eddies have a random lifetime and will approach the interface within a random distance. He derived the following relation

$$K_L = \frac{\sqrt{Dr}}{1 + \delta \sqrt{D/r}} \quad (2.14)$$

The conceptual models show that K_L depends on \sqrt{D} . Although these conceptual models were developed for various sources of turbulence (the film-renewal model was in the context of bottom induced turbulence) they are not limited to a certain flow mechanism. The influence of the flow conditions are hidden in the term r which often remains unknown in experiments. The numerical results of this study enable an exact determination of the transfer velocity K_L and δ .

2.4 Numerical investigations of scalar transfer at air-water interfaces

The problem of the gas transfer is essentially a scalar transport problem. When neglecting radiation and evaporation, it can be assumed that the mass and heat transfer are dominated by convection and diffusion. The only difference is that the Prandtl number Pr is the ratio

of momentum diffusivity (kinematic viscosity) to thermal diffusivity, whereas the Schmidt number Sc is the ratio of momentum diffusivity (viscosity) and mass diffusivity (see equation (2.5)). The terminology in the literature varies also depending on the context or the aim of the particular paper. In journals that focus more on fluid dynamics often the physical terms 'mass transfer' and 'heat transfer' are used. In papers with a focus on numerics often the broader term 'scalar transport' is used (not defining what the scalar quantity represents). It is important to be aware when reviewing papers that either terminology describes the same problem and there is an analogy between Pr and Sc . In the following review the notation is given as nominated by the appropriate authors so Pr and Sc compare directly. Up to now, a number of numerical studies of scalar transfer across the air-water interfaces have been carried out. Many more numerical simulations have been carried out on heat transfer problems than on mass transfer problems, as heat transfer plays an important role in many industrial applications. The majority of the works studied wind-shear driven and stirred flow situations which have a higher turbulence content than the convectively driven flows. The review covers the three principal mixing mechanisms of wind-shear-driven flows, bottom-shear driven flows and buoyant flows (see figure 1.1). Where applicable, a brief description of the numerical methods used for the scalar transport in the reviewed work is also given.

2.4.1 Wind-shear-induced flows

It is well known that wind-shear enhances the gas exchange near the air-water interface. In nature, especially on larger scales like an ocean's surface, wind is the main driving force for gas transfer. In numerical investigations there are several boundary conditions that can be considered. Two common cases are counter-flow wind-shear and free wind-shear. In a counter-flow the liquid flows in opposite direction to the air above as illustrated in Fig. 2.1a. Both flow fields are driven by pressure boundary conditions. In the case of free wind-shear the water body is passive. There is no driving pressure condition for the water and the flow is entirely driven by the wind-shear at the interface. Both, water and air, move in the same direction. The shear at the interface and hence the turbulence levels on both sides of the interface is obviously stronger when the velocities are opposed. The boundary conditions

in the vertical directions are usually periodic. Another matter is whether the interface is

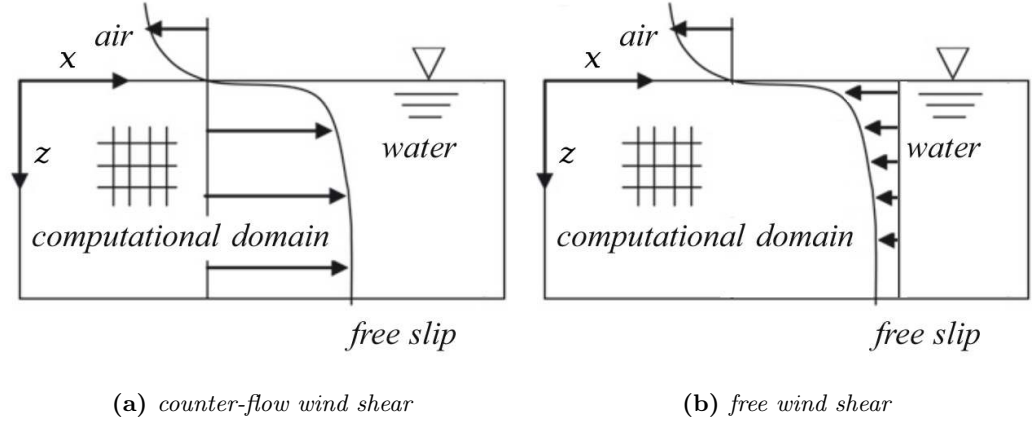


Figure 2.1: principal conditions of wind-shear driven flows

deformable or not. In nature almost all wind conditions cause waves on the water surface in some magnitude. A number of early numerical investigations do not consider a deformable interface.

Campbell and Hanratty [16] pioneered the class of shear driven DNS. McCready et al. [65] followed but also considered only a flat non-deformable interface. They could show that the average mass transfer coefficient is found to depend on Schmidt number to the 0.5 power, in agreement with classical theories. It is related to the velocity field in the liquid primarily through the mean-square value of the gradient of normal velocity fluctuations at the interface. Calmet and Magnaudet [15] used Large Eddy Simulations (LES) to simulate the scalar transport at a sheared and a shear-free interface (see Section 2.4.2). Their results show that the concentration field is greatly affected by the structure of the turbulence in the diffusive sublayer located just below the interface. The model of McCready et al. involving the surface divergence could be identified as most suitable to predict the mass transfer coefficient through the gas-liquid interface. Hasegawa and Kasagi [34, 35] studied wind-shear driven mass transfer across the turbulent interface at a Schmidt number of $Sc = 100$ and showed that various concentration statistics reveal that the transport mechanism at a highly contaminated interface becomes dynamically equivalent to that at a solid surface. They used

a pseudo-spectral Fourier method for the spatial discretization in the horizontal directions, whereas a finite volume method was employed in the normal direction in which turbulent and molecular mass fluxes were evaluated at a cell surface with second-order accuracy. The interface was not deformable in their work so it acted like a solid wall for the air side. The turbulent structures were resolved on both, the air and water sides of the sheared interface. A hybrid DNS-LES model was used with DNS near the interface and LES in the field further away.

More recently the study of scalar transfer across sheared gas-liquid interfaces was extended in complexity by introducing the deformation of the interface caused by wind. The wave formation and turbulence mechanisms of the sheared gas-liquid interface has developed into a whole new field of numerical fluid dynamics. For further information the works of Angelis et al. [2] and Lombardi et al. [62] and references therein are a good starting point. In the context of scalar transport, the presence of waves adds a new source of motion to the liquid (and gas) side that influences the scalar transport in the liquid domain. As high shear is beneficial for the wave formation these studies usually comprise the counter flow regime where liquid and gas flow in opposite direction as illustrated in Fig. 2.2.

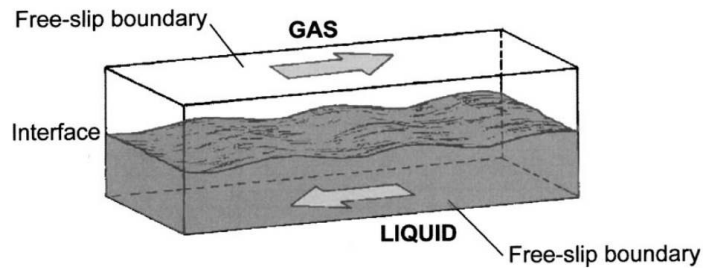


Figure 2.2: *Flow regime for sheared wavy interfaces [56]*

Kunugi et al. [55] carried out a Direct Numerical Simulation of carbon-dioxide gas absorption caused by turbulent flow over a free deformable interface. They found the exchange coefficient of carbon-dioxide gas at the turbulent free surface estimated in their study was in good agreement with existing experimental data. Henry's law was applied to the evaluation of the solubility. They used a second-order scheme for the spatial differencing terms on a staggered grid system and the Euler implicit scheme to solve the momentum equation.

Lakehal et al. [56] carried out Direct Numerical Simulation of turbulent heat transfer across a mobile, sheared gas-liquid interface. They showed that high-frequency fluctuating fields play a minor role in scalar transport across the interface. The flow system comprised a gas and a liquid phase flowing in opposite directions with a deformable wavy interface (Fig. 2.2). Prandtl numbers of $Pr = 1, 4$ and 10 were covered. The scalar reconstruction procedure used a collocation pseudo-spectral technique employing Fourier series in the homogeneous, streamwise and spanwise directions, and Chebychev polynomials in the non-uniform direction normal to the interface.

Similarly, Banerjee also used a pseudo-spectral method to extensively study the mechanisms of turbulence and scalar exchange at the air-water interface in several publications (see [7, 6] and references therein). Schwertfirm and Manhart [79] also studied passive scalar transport in a turbulent channel flow for Schmidt numbers up to $Sc = 49$. They used a similar approach to the present work by solving the scalar on a finer grid than the velocity which was mapped by a conservative interpolation to the fine-grid. An explicit iterative finite-volume scheme of sixth-order accuracy was employed to calculate all convective and diffusive fluxes, while for the time-integration a third order Runge-Kutta method was used [80].

2.4.2 Bottom-shear-induced flows

For flows in channels the dominant source of turbulence is the shear of the fluid with its surroundings. Considering periodic boundary conditions on the sides the shear profile is schematically illustrated in Figure 2.3. In contrast to the illustration of the wind-shear driven case in Figure 2.1 the gas-liquid interface at the top is now shear free. Some numerical investigations consider channels with shear introduced at the side walls. Another possible scenario is a stationary fluid where turbulence is generated by grid or surface oscillations at the bottom. In general this section reviews previous studies of scenarios where the turbulence generation takes place in the flow field away from the shear free interface. The bottom shear may be generated by a fixed wall and moving fluid over it or a stirring in an otherwise stationary fluid. As in the previous section (see 2.4) the research reviewed here covers

general passive scalar transport which is modelled by using an unsteady convection-diffusion equation. The scalar may be mass or heat with its different notation of Schmidt and Prandtl numbers.

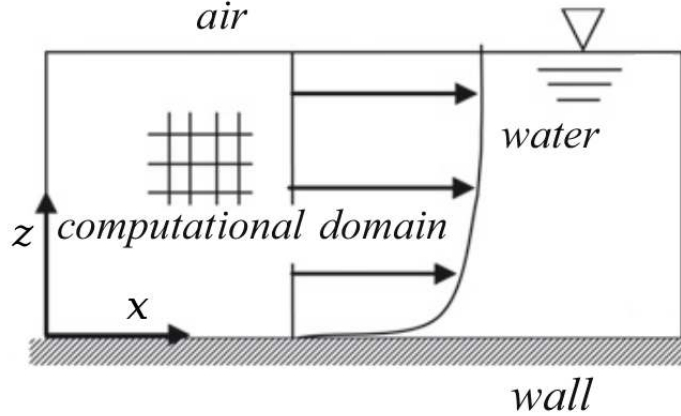


Figure 2.3: *Bottom-sheared channel flow*

Early numerical investigations of the problem were carried out by Komori et al. [54] who studied scalar transfer across a zero-shear gas-liquid interface in a three-dimensional direct numerical simulation (DNS). They found the mass transfer coefficient in good agreement with experimental data and turbulent quantities were also compared to results from two-colour laser Doppler velocimetry. The non-linear terms in the Navier-Stokes equation were discretized with a fifth-order upwind scheme. Other spatial derivatives and base vectors were approximated by a second-order central difference.

Nagaosa [73], Nagaosa and Saito [74] studied scalar transfer at a Prandtl number of $Pr = 1$ across a shear-free, non-wavy gas-liquid interface (top wall) in fully developed channel flow. They were using a second-order central finite-difference approximation for all terms.

Na et al. [72] carried out DNS of fully developed flow in a channel for which the bottom wall was heated and the top wall was cooled for Prandtl numbers up to $Pr = 10$. They concluded the use of a turbulent Prandtl number to relate scalar transport to the velocity field could be a sensible approach, as the correlation between velocity and temperature

fluctuations was independent of Pr .

Handler et al. [30] used a pseudo-spectral approach with Fourier expansions to carry out direct numerical simulations for the transport of a passive scalar at a shear-free boundary in fully developed channel flow. They found that patterns of patches of warm fluid near the air-water interface were in good agreement with infrared imagery. A pseudo-spectral approach was developed in which the velocity and temperature fields were expanded in Fourier modes in the horizontal directions and Chebyshev modes in the vertical direction normal to the interface. The Prandtl number for the passive scalar transport was $Pr = 2$.

Kawamura et al. [51] carried out a direct numerical simulation (DNS) of turbulent heat transfer for various Prandtl numbers ranging from 0.025 to 5. The configuration here was fully developed channel but with uniform heating (scalar transport) from both the bottom and top walls, using no-slip velocity boundary conditions. More recently, the contribution of Piller et al. [76] examines the influence of low Prandtl numbers between $0.025 \leq Pr \leq 1.0$ on turbulent transport in channel flow, again using a no-slip velocity boundary condition and a constant temperature along the top and bottom walls. They found that high-frequency velocity fluctuations are ineffective in transporting heat. They also used the common pseudo-spectral technique to solve the full three-dimensional time-dependent Navier-Stokes and advection-diffusion equations.

The Schmidt/Prandtl numbers increased significantly with the application of Large Eddy Simulation. Calmet and Magnaudet carried out Large Eddy Simulations (LES) for both sheared and shear-free interfaces in channel flow for Schmidt numbers up to $Sc = 200$ [15, 63, 14]. However the LES technique means a loss of detail in the subgrid scale where the fluxes are not forced to align with the resolved concentration gradient. Wang and Lu [95] carried out LES for stratified turbulent open channel flows with low- to high-Prandtl numbers ranging from $Pr = 0.1$ to $Pr = 100$.

Suga and Kubo [86] employed an extended version of the analytical wall-function (AWF) that is designed for Reynolds averaged Navier Stokes simulations (RANS) to predict surface mass transfer rates and turbulent concentration fields across undeformable air-water interfaces at Schmidt numbers ranging from $1 \leq Sc \leq 1000$. It has to be stressed that RANS

uses a subscale model and does *not* resolve any near-interface structures.

2.4.3 Buoyant-convective-induced flows

Buoyancy driven flow problems have always attracted large interest in the fluid dynamics research community as they are crucial to a large field of processes in nature and technical applications. Buoyant flows are present almost everywhere in everyday life on various scales, from very large scales such as the natural convection in the Earth's atmosphere, to very small scales such as (passive) cooling of electronic microchips. Wherever density differences in a fluid are sufficiently high, less dense liquid will start to rise and denser liquid will start to sink, respectively. Even though buoyant flows are omnipresent, they are also often very complex and hard to predict. For instance, air rising from an infinite heated horizontal plate shows complicated structures of rising hot plumes with velocities varying in strength and direction that can exhibit chaotic behaviour, whereas a sheared flow over an infinite horizontal plate is predictable and the velocity boundary layer is well known. A classical problem in fluid dynamics that has been investigated intensively is the Rayleigh-Bénard (RB) convection, a buoyancy driven flow of a fluid heated from below and cooled from above. There is a large variety of interesting aspects for research that can be derived from that basic problem. Even the simple case of RB-convection in a rectangular domain can exhibit a large spectrum of flow patterns, from laminar to turbulent, from totally steady flows to chaotic behaviour, all depending on various parameters such as Rayleigh-number, aspect ratio, fluid properties, etc. Even though the discovery and early study of the problem traces back over 100 years to Bénard (1900) and Lord Rayleigh (1916) the RB-convection remains a field of very active research. When looking at the problem numerically there is one major difference from the wind-shear and bottom-sheared cases. To solve the flow field the temperature of the fluid has to be known so the problem of convective-diffusive scalar transport is inevitable.

The problem of RB convection is still attracting large attention of research. Ahlers et al. [1] gives a good review. Early numerical investigations were focused on the Rayleigh-Bénard convection in the atmosphere. Deardorff [24, 25] studied an atmospheric flow in a domain of $5 \times 5 \times 2$ km containing $40 \times 40 \times 40$ grid points using a second-order finite difference

method for all advective terms. Grotzbach [28] followed with Direct Numerical Simulation of RB-convection of air ($Pr = 0.71$) in the atmosphere for a range of Rayleigh numbers from $Ra = 1500$ to $Ra = 381225$. A Large Eddy Simulation (LES) approach is used by Eidson [27] with Rayleigh numbers up to $Ra = 2.5 \times 10^6$ and a Prandtl number of $Pr = 0.71$ (air). All the works above used air as fluid which has a very low Prandtl number. The velocity and temperature field agreed largely with experimental data. They all used finite difference methods by some means to discretize the diffusive and convective terms of the scalar transport, in this case the sole scalar quantity is the temperature.

Balachandar et al. [4] studied RB-convection with very high Rayleigh numbers of $Ra \approx 1.7 \times 10^7$ and a Prandtl number of $Pr = 0.71$ using a pseudo-spectral method with a Fourier series expansions on a $96 \times 96 \times 97$ grid [17]. The flow regime was found to be within the 'hard turbulence' and compared well to experiments. The time integration is using a Crank-Nicholson scheme for the dissipative terms and a second-order Adams-Bashforth method for the advection and buoyancy terms. Deane and Sirovich [22] used a similar approach to study moderate Rayleigh numbers of $Ra = 46000$ on a grid of $32 \times 32 \times 32$ points using also the Prandtl number of air. They used a pseudo-spectral method based on Herring and Wyngaard [41]. Kerr [53] studied the Rayleigh number scaling using a pseudo-spectral method with Fourier expansions in the horizontal directions and Chebyshev polynomials in the vertical directions at large aspect ratio (6:6:1) domain on meshes up to $288 \times 288 \times 96$ points. The typical non-dimensional parameters were $Pr = 0.7$ and a Rayleigh number between $Ra = 5 \times 10^4$ and $Ra = 2 \times 10^7$. The follow up [52] increased the Prandtl number in various steps between $Pr = 0.7$ (air) and $Pr = 7$ (water). Curry et al. [20] studied the transition to chaos as the Rayleigh number is increased for the case with free slip boundary conditions at the top and bottom, which is the boundary condition for a free surface that is also used in this present research.

Verzicco studied Rayleigh-Bénard convection in a cylindrical geometry in several publications. Verzicco and Camussi [92] carried out numerical simulations for a low Prandtl-number regime in a cylinder ($Pr = 0.022$, Mercury) and the transition to chaos when the Rayleigh number is varied from $Ra = 3.75 \times 10^3$ to $Ra = 3.75 \times 10^4$. The effects of the Prandtl number

in a cylinder was studied in Verzicco and Camussi [93]. The cylinder had an aspect ratio of 1 where the top wall was cooled and the bottom heated. The side wall was adiabatic. The instability was triggered by adding a small random noise to the temperature field. They carried out three series of numerical experiments where they set $Pr = 0.022$ (mercury) for $Ra \leq 10^6$ and $Pr = 0.7$ (air) for $Ra = 10^7$. In a third series the Rayleigh number was fixed at $Ra = 10^5$ and the Prandtl number was varied from $Pr = 0.0022$ up to $Pr = 15$. The variables have been discretized using second-order-accurate finite-difference approximations in space and time. In Verzicco and Camussi [94] the Rayleigh number ranged up to $Ra = 10^{11}$ but the Prandtl number remained relatively low at $Pr = 0.7$ (air).

In the recent research, where only the top surface is being cooled, the boundary condition for Rayleigh-Bénard convection by its definition is only really met at the initial state. The Rayleigh number does change over time as there is only heat extracted from the fluid. Theoretically, if the fluid had cooled down sufficiently it would eventually become stationary. From a numerical point of view the process of interest is solving the convection-diffusion of a scalar introduced at a boundary. Whether this happens only at one (cooled) boundary at the top or at two boundaries with opposite boundary conditions (cooled at top, heated from below) is, for the numerical procedure, not relevant. In the studies of buoyancy-driven-flow mentioned above, the temperature is the sole transported scalar (besides the pressure). It is normally the only scalar of interest as the studies focus usually on flow regimes and heat transfer. The temperature is a non-passive scalar as it drives the Boussinesq flow and is obviously crucial for the heat transfer. The question what happens when *another*, passive, scalar is introduced has remained an open question, especially when the diffusivity of the newly introduced passive scalar (in this case the gas concentration) is much lower than the temperature diffusivity. This is the case for the transfer of soluble gases into water. For instance, the Prandtl number for water is $Pr \approx 7$ whereas the Schmidt number for oxygen diffusion into water is $Sc \approx 500$. This work is trying to close that gap.

2.5 Experimental investigations of gas transfer processes

Gas transfer processes at the air-water interface at different turbulence conditions have been investigated experimentally by many researchers. Near-interface measurements, however, are difficult because of the small scaling of the concentration boundary layer and, in some cases, the movement of the water surface (i.e. waves created by wind shear). Even in simplified experiments direct measurements of the dissolved gas concentration field can be very difficult. As turbulence is the dominating mechanism that controls the gas transfer, researchers therefore often tried to link turbulence quantities, which are easier to measure, to the gas transfer. More recently, advanced techniques such as Laser-Induced-Fluorescence (LIF) made non-intrusive measurements of the gas concentration field possible. This section gives a review of the experimental studies carried out for the three main driving mechanisms of turbulence, wind-shear, bottom-shear and buoyant convection.

2.5.1 Wind-shear-induced flows

It is well known that in nature wind-shear is the most effective way of enhancing the gas exchange process near the air-water interface. Wind speeds above 3 m/s induce considerable wave growth which increases the effectiveness of the gas transfer. Early works studied the correlation between wind-shear and gas transfer coefficient K_L [60, 10, 44, 43]. Wolff et al. [98] used a fluorescence technique to measure the concentration gradients near the interface. Subsequently, Wolff and Hanratty [97] studied the absorption of oxygen from air to water for a stratified flow by measuring the instantaneous concentration profiles close to the interface. They used oxygen quenching of the fluorescence from pyrenebutyric acid first introduced by Vaughan and Weber [91]. Münsterer et. al used the Laser-induced fluorescence (LIF) technique in several studies [71, 70, 69]. In [70] they measured the concentration boundary layer thickness at a wind speed of 3.6 m/s. They could clearly show that the thickness varies significantly over time and supports the surface renewal models. The basic idea of the surface renewal model is that eddy motions overcome the resistance near the interface by impinging upon the relatively thin concentration boundary layer, periodically renewing it by

exchanging the saturated fluid at the top with unsaturated fluid from the bulk.

Woodrow Jr and Duke [99] carried out a detailed study also using a LIF technique that images planar oxygen concentration fields near air-water interfaces. They observed detached high concentration layers when waves are present. Researchers also tried to investigate the interaction between eddy structures and gas transfer. Takehara and Etoh [87], for instance, visualized the transfer of CO₂ at water surfaces under wind wave conditions and could indicate that the eddy structure plays a role in the transfer process.

2.5.2 Bottom-sheared-induced flows

In nature the most common occurrences of bottom-sheared flows are rivers and streams. These flows are characterized by certain stream parameters, such as the mean velocity, surface roughness or water depths. Early works tried to find empirical relationships between the gas transfer and the stream parameters (e.g. Gulliver and Halverson [29], Thackston and Krenkel [88], Bansal [8], Gulliver and Halverson [29]). Researchers then recognized that eddies near the interface enhance the gas transfer. In various experiments in open channel flows [66, 67, 18, 68] the channel roughness has been related to the gas exchange. Their results were in good agreement with the surface renewal theory and small eddy models. The gas transfer coefficient K_L was determined by measuring the oxygen levels in samples at various times starting with deoxygenated water. The near surface processes still remained unknown as direct measurements near the surface were difficult to perform.

Bottom-sheared turbulence can also be generated by stirring in a tank which makes the experimental setup a bit easier than when using a channel. Brumley and Jirka [12] were amongst the first to perform detailed near surface measurements of the hydrodynamics. They could produce a detailed mapping of the horizontal and vertical velocity fluctuations within 0.4 mm of the surface.

This insight into the near surface hydrodynamics led to the measurements of the oxygen concentration fluctuations with a gas probe. Jirka and Ho [47], Chu and Jirka [19] could estimate the thickness of the concentration boundary layer. Atmane and George [3] conducted similar results but the turbulence was generated by micro-jets placed at the bottom

of the tank. Herlina and Jirka [39] used the laser-induced fluorescence (LIF) technique to investigate the interaction between oxygen absorption into liquids and bottom shear-induced turbulence in a grid-stirred tank. The LIF technique enabled a more detailed visualization as well as quantification of planar concentration fields of the dissolved oxygen near the air-water interface. Qualitative observation of the images provided more insight into the physical mechanism controlling the gas transfer process. Even more recently, Jirka et al. [45] were the first to use a combination of Particle-Image-Velocimetry (PIV) and the LIF technique to visualize instantaneous vector and oxygen concentration contour maps.

2.5.3 Buoyant-convective-induced flows

There are two main scenarios for penetrative buoyant convection where only one surface is imposed with a temperature and the convection is penetrating a bulk fluid further afield. One could either heat the bottom surface or cool the top surface. Penetrative convective instability is omnipresent in the atmosphere where the ground is heated by the sun. A similar scenario is a container full of liquid that is heated from the bottom. However, also the opposite scenario (which is the focus of this work) occurs in nature where the top surface is cooled (for instance in lakes at night exposed to cooler temperatures at the top). Both scenarios, heated bottom or cooled top, have been investigated by researchers. Most early works studied the heat transfer but more recent works also related the problem to gas exchange.

Spangenberg and Rowland [85] took Schlieren photographs of the convection currents from the top and side of a tank of water induced by surface cooling. They could visualize that cooled liquid plunges down in sheets in a reticulated pattern. Deardorff et al. [26] studied non-steady penetrative convection in a cylindrical water tank where the bottom surface was suddenly heated. Vertical profiles of horizontally averaged temperature and heat flux were measured and interpreted. Similar experiments studied the thermal structure in the boundary layer and its relation to the heat flux from the cooling and evaporating surface of a deep tank of water [50]. Field experiments investigated the thermal boundary layer even in lakes [11, 77, 49].

None of these investigations has related the problem to gas transfer. Soloviev and Schlüssel [84] tried to estimate the gas transfer coefficient at the air-sea interface in buoyant convection, however wind-shear was also present in that case. Only more recently the usage of the LIF technique enabled a more detailed visualization and measurements of the oxygen field near to the interface [58, 57, 78]. Only recently, Jirka et al. [46] used the combined PIV-LIF technique to give a detailed insight into the oxygen concentration and velocity field near the cooled free surface in a water tank. Their results provide an experimental comparison with the numerical results obtained in the present work. Both have been found to be in very good agreement with each other.

2.6 WENO schemes

Weighted essentially non-oscillatory (WENO) schemes are high-order accurate numerical schemes that are used in a large field of application. They are based on essentially non-oscillatory (ENO) schemes which were first published in the meanwhile classic paper of Harten et al. in 1987,[32]. Liu et al. [61] introduced the idea of taking a convex combination to construct a stencil using nonlinear weights with a high order-of-accuracy in smooth regions while weighing out the nonsmooth stencils in regions containing steep gradients or discontinuities. Their work studied WENO($2r - 1$) schemes for different stencil size $r = 2$ (WENO3) and for $r = 3$ (WENO5). In the meantime a large variety of WENO schemes has been developed. Many improvements were made by modifying the smoothness determination. Jiang and Shu [81] introduced a new smoothness indicator that was used to evaluate the nonlinear weights. The size of the stencil has also been further increased by Balsara and Shu [5] extending it up to $r = 6$ (WENO11). The WENO5 scheme is used most widely [37, 64, 48]. Henrick et al. [37] could show that the weights generated by the classical choice of smoothness indicators in [81] failed to recover the maximum order of the scheme at critical points of the solution where the first derivatives are zero. They developed the so called WENOM schemes where a mapping procedure is introduced to keep the weights of the stencils as near as possible to the optimal weights. The resulting mapped WENOM

scheme of [37] presented more accurate results close to discontinuities. Even more recently, Borges et al. [9] achieved the same results as mapped WENO schemes without mapping but by improving the accuracy of the classical WENO5 scheme by devising a new smoothness indicator and nonlinear weights using the whole 5-points stencil and not the classical smoothness indicator by Jiang and Shu [81] which uses a composition of three 3-points stencils. The schemes of Borges et al. are known as WENO-Z schemes.

Aim of this work: The direct numerical simulations conducted up until present lack to represent realistic Schmidt numbers to predict the gas transfer across the air-water interface. Most studies so far cover only a range of theoretical Schmidt (or Prandtl) numbers ranging from 1 to 10. Even in the LES studies of Calmet and Magnaudet [15], MAGNAUDET and CALMET [63], Calmet and Magnaudet [14] the maximum Schmidt number is only $Sc = 200$. The Schmidt number for typically soluble gases from air into water such as oxygen and carbon-dioxide is around $Sc \approx 500$. Whilst it is well known that the flow field can be accurately resolved with DNS the limitations of the currently available DNS studies of gas transfer problems lay in resolving the *convection* of such low-diffusive scalars in that flow field with acceptable accuracy. In addition to the unsolved challenge of high Schmidt number numerical simulations the physical mechanisms are of such small scale that detailed quantifiable experimental analysis is nearly impossible. There is currently no method to measure, say, the instantaneous distributed oxygen concentration in a water tank. This lack of gaining detailed insight into the gas transfer process makes reliable numerical results with realistic Schmidt numbers more desirable. This study aims to solve the convection-diffusion of the low-diffusive scalar field for Schmidt numbers up to $Sc = 500$. For the first time a WENO scheme in conjunction with a dual mesh approach was deployed to solve the scalar convection in such a flow problem and through a number of 1D and 2D numerical experiments it could be demonstrated that at least second order accuracy could be achieved for the $Sc = 500$ case. This work serves as excellent reference for future experiments and numerical analysis to achieve high Schmidt number resolution.

Chapter 3

Numerical Method

THIS chapter outlines the numerical scheme deployed. The gas transfer across the air-water interface in a buoyant convective flow represents a low diffusive passive scalar transport problem. The scalar quantity is the gas concentration which is represented by the variable φ . The fluid temperature, T , acts as an active scalar as it drives the convection. The horizontal spatial directions are x and y while z corresponds to the vertical direction. The respective velocities in these directions are u, v and w .

In the following the discretization method for the convection-diffusion equations on a stretched grid will be discussed. The method to discretize the incompressible Navier-Stokes equation to resolve the flow field is described as well as the modified WENO scheme that is employed to discretize the convection of the scalar quantities.

3.1 Governing equations

The mass transfer into a fluid is a convection-diffusion problem that weakly couples two general systems of differential equations. One is the well known Navier-Stokes equations which describe the motion of fluids and are based on the conservation of momentum (Newton's second law of motion) and mass. The other system is the convection-diffusion equation that describes the transport of mass (or any other physical quantity such as temperature or energy) within a fluid. A further equation is needed in the set which is the continuity equation,

which states that the rate of change for a scalar quantity in a differential control volume is given by convection and diffusion into and out of that part of the system. These scalar fluxes have two sources, convection and diffusion. The convection depends on the velocity of which the dynamics are described by the Navier-Stokes equations and the gradient of the scalar. The second source of transfer is diffusion which depends on changes in the concentration gradient.

3.1.1 The Navier-Stokes equations

Newtonian fluid flow is described by the Navier-Stokes equations which essentially consist of the principle of conservation of mass and the conservation of momentum. If the density ρ is constant the three-dimensional Navier-Stokes equations with the convection in a conservative form reads,

$$\frac{\partial u}{\partial t} + \frac{\partial u^2}{\partial x} + \frac{\partial(uv)}{\partial y} + \frac{\partial(uw)}{\partial z} = -\frac{1}{\rho} \frac{\partial p}{\partial x} + \nu \left\{ \frac{\partial^2 u}{\partial x^2} + \frac{\partial^2 u}{\partial y^2} + \frac{\partial^2 u}{\partial z^2} \right\} \quad (3.1)$$

and

$$\frac{\partial v}{\partial t} + \frac{\partial(uv)}{\partial x} + \frac{\partial v^2}{\partial y} + \frac{\partial(vw)}{\partial z} = -\frac{1}{\rho} \frac{\partial p}{\partial y} + \nu \left\{ \frac{\partial^2 v}{\partial x^2} + \frac{\partial^2 v}{\partial y^2} + \frac{\partial^2 v}{\partial z^2} \right\} \quad (3.2)$$

and

$$\frac{\partial w}{\partial t} + \frac{\partial(uw)}{\partial x} + \frac{\partial(vw)}{\partial y} + \frac{\partial w^2}{\partial z} = -\frac{1}{\rho} \frac{\partial p}{\partial z} + \nu \left\{ \frac{\partial^2 w}{\partial x^2} + \frac{\partial^2 w}{\partial y^2} + \frac{\partial^2 w}{\partial z^2} \right\} \quad (3.3)$$

where u is the velocity in x -direction, v is the velocity in y -direction, w is the velocity in z -direction, p is pressure, t is time and ν the kinematic viscosity (see Section 3.2 for the non-dimensionalization). The continuity equation for incompressible flow is given by

$$\frac{\partial u}{\partial x} + \frac{\partial v}{\partial y} + \frac{\partial w}{\partial z} = 0. \quad (3.4)$$

The three equations above constitute a non-linear system of partial differential equations which are discretized as described in Section 3.4 to obtain the velocity field which drives the convective transport of the scalar φ through the domain.

3.1.2 The convection-diffusion equation of the scalar φ

The entire process of the scalar transport is a combination of convection and diffusion described by the convection-diffusion equation. The three-dimensional convection-diffusion equation of $\varphi = \varphi(x, y, z, t)$ reads

$$\frac{\partial \varphi}{\partial t} + u \frac{\partial \varphi}{\partial x} + v \frac{\partial \varphi}{\partial y} + w \frac{\partial \varphi}{\partial z} = \Gamma \left(\frac{\partial^2 \varphi}{\partial x^2} + \frac{\partial^2 \varphi}{\partial y^2} + \frac{\partial^2 \varphi}{\partial z^2} \right). \quad (3.5)$$

The convective terms on the left hand side arise because of the presence of the velocities u , v and w . The diffusive terms on the right hand side are essentially Fick's second law that states that the diffusive flux is proportional to the local concentration gradient (see (1.2)) The diffusion coefficient is $\Gamma = \frac{1}{ReSc}$ (where Re is the Reynolds number and Sc is the Schmidt number, see Section 3.2). The diffusive term on the right is discretized using a fourth-order accurate central scheme, while the convective term is discretized using a variant of the fifth-order WENO scheme developed by Liu et al. [61] (see section 3.5).

3.2 The non-dimensionalization

The governing equations in Section 3.1 can be made non-dimensional by selecting a characteristic velocity scale U and a characteristic length-scale L . We define the Reynolds number Re by

$$Re = \frac{UL}{\nu}, \quad (3.6)$$

where ν is the kinematic viscosity. This dimensionless number represents the relative importance of the convective and diffusive terms in the Navier-Stokes equations (3.1) and (3.3).

The scalar φ is non-dimensionalized using the scalar magnitude φ_s at the interface and the magnitude in the bulk $\varphi_{B,0}$ so that

$$\varphi^* = \frac{\varphi - \varphi_{B,0}}{\varphi_s - \varphi_{B,0}}. \quad (3.7)$$

The fluid temperature T is an active scalar as temperature differences are causing natural convection to occur in the presence of a gravity field. The fluid temperature T is discretized

in the same way as φ and is made non-dimensional with,

$$T^* = \frac{T - T_s}{T_{B,0} - T_s}. \quad (3.8)$$

where T_s is the temperature at the interface and $T_{B,0}$ the temperature in the bulk.

A very important non-dimensional parameter for the gas transfer process at the air water interface is the Schmidt number Sc . It is defined as the ratio of momentum diffusivity (viscosity ν) and mass diffusivity D .

$$Sc = \frac{\nu}{D} \quad (3.9)$$

Similarly the Prandtl number Pr is the ratio of kinematic viscosity ν to thermal diffusivity α ,

$$Pr = \frac{\nu}{\alpha} \quad (3.10)$$

Subsequently the diffusion coefficient Γ in (3.5) is simply,

$$\Gamma = \frac{1}{ReSc} \quad (3.11)$$

when considering the mass transfer of gas into water. For the heat transfer into water, which is also a convection-diffusion problem the Schmidt number Sc in (3.11) is replaced with the Prandtl number Pr . The temperature diffusion coefficient Γ_T reads,

$$\Gamma_T = \frac{1}{RePr}. \quad (3.12)$$

For water at $T_B = 23$ °C the dimensions for the physical quantities above are $[\nu] = 9.122 \times 10^{-7} \frac{m^2}{s}$ and $[\alpha] = 0.15 \times 10^{-6} \frac{m^2}{s}$, hence $Pr = 6$. The characteristic velocity scale is $[U] = 1 \frac{cm}{s}$ and the length scale $[L] = 1cm$. Up to four gas concentration fields are solved simultaneously. The mass diffusivity D has various values so that $Sc = 20, 50, 200$ and 500 . For the transfer of typical soluble gases like CO_2 and oxygen in to water the Schmidt number

is around $Sc \approx 500$. The temperature T_0 at the air-water interface at the top is $T_0 = 20^\circ\text{C}$ and the bulk temperature is $T_B = 23^\circ\text{C}$.

The Rayleigh number, Ra , for a fluid is a dimensionless parameter associated with buoyancy driven flow which describes the relationship between viscosity and buoyancy and is defined as

$$Ra = \frac{\Delta\rho g L^3}{\alpha\mu} \quad (3.13)$$

where $\Delta\rho$ is the density difference of the fluid between the two temperatures T_B and T_0 and μ is the dynamic viscosity and g is the gravity. When the Rayleigh number is below the critical value $Ra_c \approx 657$, the fluid remains stationary as the viscous forces outweigh the buoyancy forces. When the Rayleigh number exceeds the critical value natural convection sets in and a buoyancy driven flow is present. The density difference of water with a temperature between T_B and T_0 is $\Delta\rho = 0.69 \frac{\text{kg}}{\text{m}^3}$ and the dynamic viscosity at $T_B = 23^\circ\text{C}$ is $\mu = 9.0957 \times 10^{-4} \frac{\text{kg}}{\text{m}\cdot\text{s}}$. Using the values for the characteristic length scale L and the thermal diffusivity α as defined above the Rayleigh number in this case is $Ra \approx 49600$ which is significantly above the critical value. This shows that the temperature induced density distribution is definitely unstable and natural convection may occur.

The buoyancy term $\beta(T^*)$ in (3.22) represents the well known Boussinesq approximation which is used to model gravity forces due to small changes in density in an incompressible flow. Other influences of the density changes such as influences on the conservation of mass and momentum are neglected. The Boussinesq approximation introduces momentum in the vertical z -direction only when density differences in the fluid are present. This is achieved by using the reduced gravity g' . The buoyancy term $\beta(T^*)$ in (3.22) is non-dimensionalized so that

$$\beta(T^*) = g' = g \frac{\rho_{23} - \rho_{20}}{\rho_{23}} \times T^* \quad (3.14)$$

where ρ_{23} and ρ_{20} are the densities at the respective reference temperatures $T_B = 23^\circ\text{C}$ (in the bulk) and $T_0 = 20^\circ\text{C}$ (at the interface), T^* is the non-dimensional fluid temperature (see (3.8)) and $g = 9.81 \frac{\text{m}}{\text{s}^2}$ (the gravity constant).

3.3 Physical Assumptions

The mathematical model described here adopts physical assumptions which are outlined and justified in this section.

Boussinesq Approximation: The term $\beta(T^*)$ in (3.22) represents the well known Boussinesq approximation which is used to model buoyant convection in incompressible flow. It is understood to consist of the following:

1. Density is assumed constant except when it causes buoyant forces
2. All other fluid properties are assumed constant
3. Viscous dissipation is assumed negligible

The first point means that the fluid is assumed incompressible and that density is only variable when the reduced acceleration due to gravity in the momentum equation is calculated (see (3.22) and (3.14)) The second and third point mean that other fluid properties such as viscosity and thermophysical quantities like thermal conductivity or diffusivity are assumed to be constant (Essentially Schmidt number Sc , Prandtl number Pr , etc... are not a function of temperature). The validity of the Boussinesq approximation for buoyant flows in water is well known but a good review is given by Zeytounian [100].

Gas concentration is treated passive: The gas concentration is treated as a passive scalar. None of the fluid properties, especially the density, is assumed to be influenced by the gas concentration level in the fluid. Harvey et al. [33] studied the effect of dissolved air on the density of water. They show that the density difference of water saturated with dissolved air compared to pure water at 20°C is $\Delta\delta = 0.00244kg/m^3$. Considering the density of water as $\approx 1000kg/m^3$ this is less than 3 parts per million, which makes it obvious that this minimal density change can be neglected in the flow equations.

Mass Conservation: The assumptions stated above imply that the mass in the fluid domain is assumed to stay constant. The small amount of gas dissolving into the water

body is negligible when considering the entire system. It must be noted that the effect of evaporation is also not modeled as the temperature difference between air and water is only 3°C .

3.4 Flow Solver

This section outlines the numerical method of the flow solver used in the buoyancy driven flow. The velocity field is solved by a finite-difference discretization of the convective terms using a fourth-order unconditionally kinetic energy conserving method combined with a fourth-order accurate central method for the diffusive terms. The flow solver was previously validated in various works. Wissink [96] used the code to determine the growth rate of a Kelvin-Helmholtz instability in a mixing layer. The results were found to converge upon grid refinement and the final growth rate of the instability was found to closely match the growth rate predicted by theory. Smith and Wissink [83] applied the code to simulate the growth and limiting behaviour of travelling waves in plane Poiseuille flow. The simulation results were verified against existing theory and a grid refinement study was carried out. More recently Herlina and Wissink [40] used this flow solver to simulate turbulence diffusing from the lower boundary towards a free-slip surface. A grid refinement study was carried out to proof that the results were time-accurate and grid-independent and the results produced where shown to match existing theory.

The 3D incompressible Navier-Stokes equations are discretized on a non-uniform, staggered mesh in combination with a second-order accurate Adams-Bashforth time integration. The Boussinesq approximation is applied in order to account for the effects of buoyancy. For three-dimensional incompressible flow the continuity equation reads,

$$\frac{\partial u}{\partial x} + \frac{\partial v}{\partial y} + \frac{\partial w}{\partial z} = 0, \quad (3.15)$$

which in discretized form on a staggered mesh as shown in Fig. 3.1 reads

$$\frac{u_{i+\frac{1}{2},j,k}^{(n+1)} - u_{i-\frac{1}{2},j,k}^{(n+1)}}{x_{i+\frac{1}{2}} - x_{i-\frac{1}{2}}} + \frac{v_{i,j+\frac{1}{2},k}^{(n+1)} - v_{i,j-\frac{1}{2},k}^{(n+1)}}{y_{j+\frac{1}{2}} - y_{j-\frac{1}{2}}} + \frac{w_{i,k+\frac{1}{2}}^{(n+1)} - w_{i,k-\frac{1}{2}}^{(n+1)}}{z_{k+\frac{1}{2}} - z_{k-\frac{1}{2}}} = 0 \quad (3.16)$$

The momentum equations are given by

$$\frac{\partial u}{\partial t} = -\frac{\partial p}{\partial x} + a \quad (3.17)$$

$$\frac{\partial v}{\partial t} = -\frac{\partial p}{\partial z} + b \quad (3.18)$$

$$\frac{\partial w}{\partial t} = -\frac{\partial p}{\partial z} + c. \quad (3.19)$$

where p is pressure and a , b and c represent the sum of the convective and diffusive terms

$$a = -\frac{\partial u^2}{\partial x} - \frac{\partial uv}{\partial y} - \frac{\partial uw}{\partial z} + \frac{1}{Re} \left\{ \frac{\partial^2 u}{\partial x^2} + \frac{\partial^2 v}{\partial y^2} + \frac{\partial^2 u}{\partial z^2} \right\} \quad (3.20)$$

$$b = -\frac{\partial v^2}{\partial y} - \frac{\partial uv}{\partial x} - \frac{\partial vw}{\partial z} + \frac{1}{Re} \left\{ \frac{\partial^2 v}{\partial x^2} + \frac{\partial^2 v}{\partial y^2} + \frac{\partial^2 v}{\partial z^2} \right\} \quad (3.21)$$

$$c = -\frac{\partial w^2}{\partial z} - \frac{\partial vw}{\partial y} - \frac{\partial uw}{\partial x} + \frac{1}{Re} \left\{ \frac{\partial^2 w}{\partial x^2} + \frac{\partial^2 w}{\partial z^2} \right\} + \beta(T^*). \quad (3.22)$$

where $Re = 100$, based on a characteristic length scale of $L = 1cm$ and a characteristic velocity of $U = 1cm/s$. The buoyancy term $\beta(T^*)$ in equation (3.22) is a function of the non-dimensional temperature T^* (see (3.8)) and is modelled using the Boussinesq approximation.

When substituting the discretized form of the momentum equation into the continuity equation a Poisson equation for the pressure is obtained. The Poisson equation is iteratively solved using the conjugate gradient method with a diagonal preconditioning. From the obtained pressure field the new velocity field can be calculated by rearranging the discretized equations of (3.17), (3.18) and (3.19),

$$u_{i+\frac{1}{2},j,k}^{(n+1)} = u_{i+\frac{1}{2},j,k}^{(n)} + \Delta t \left\{ -\frac{p_{i+1,j,k}^{(n+1)} - p_{i,j,k}^{(n+1)}}{x_{i+1} - x_i} + a_{i+\frac{1}{2},j,k}^n \right\} \quad (3.23)$$

$$v_{i,j+\frac{1}{2},k}^{(n+1)} = v_{i,j+\frac{1}{2},k}^{(n)} + \Delta t \left\{ -\frac{p_{i,j+1,k}^{(n+1)} - p_{i,j,k}^{(n+1)}}{y_{j+1} - y_j} + b_{i,j+\frac{1}{2},k}^n \right\} \quad (3.24)$$

$$w_{i,j,k+\frac{1}{2}}^{(n+1)} = w_{i,j,k+\frac{1}{2}}^{(n)} + \Delta t \left\{ -\frac{p_{i,j,k+1}^{(n+1)} - p_{i,j,k}^{(n+1)}}{z_{k+1} - z_k} + c_{i,j,k+\frac{1}{2}}^n \right\}. \quad (3.25)$$

The terms $a_{i+\frac{1}{2},k}^{(n)}$, $b_{i,j+\frac{1}{2}}^n$ and $c_{i,k+\frac{1}{2}}^{(n)}$ are the discretized form of the convective and diffusive

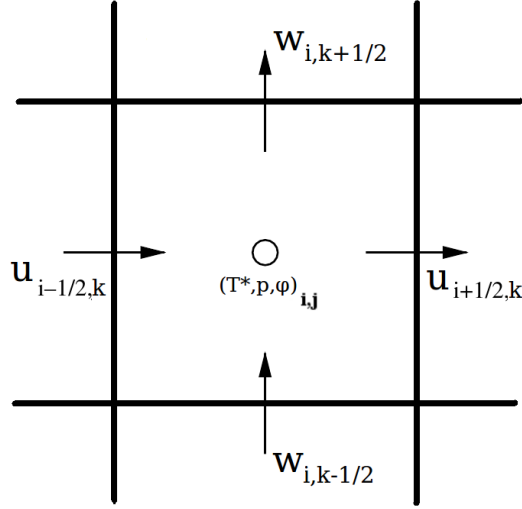


Figure 3.1: Variables on a staggered mesh [96].

terms in (3.20), (3.21) and (3.22) and can be written as,

$$a_{i+\frac{1}{2},j,k}^{(n)} = u_{i+\frac{1}{2},j,k}^{(n)} C_x(u, \bar{v}, \bar{w})_{i+\frac{1}{2},j,k} + u_{i+\frac{1}{2},j,k}^{(n)} \frac{1}{Re} D_x(u, \bar{v}, \bar{w})_{i+\frac{1}{2},j,k}^{(n)} \quad (3.26)$$

$$b_{i,j+\frac{1}{2},k}^{(n)} = v_{i,j+\frac{1}{2},k}^{(n)} C_y(\bar{u}, v, \bar{w})_{i,j+\frac{1}{2},k} + v_{i,j+\frac{1}{2},k}^{(n)} \frac{1}{Re} D_y(\bar{u}, v, \bar{w})_{i,j+\frac{1}{2},k}^{(n)} \quad (3.27)$$

$$c_{i,j,k+\frac{1}{2}}^{(n)} = w_{i,j,k+\frac{1}{2}}^{(n)} C_z(\bar{u}, \bar{v}, w)_{i,j,k+\frac{1}{2}} + w_{i,j,k+\frac{1}{2}}^{(n)} \frac{1}{Re} D_z(\bar{u}, \bar{v}, w)_{i,j,k+\frac{1}{2}}^{(n)} + \beta(T^*)_{i,j,k+\frac{1}{2}} \quad (3.28)$$

where $C_x(u, \bar{v}, \bar{w})$, $C_y(\bar{u}, v, \bar{w})$ and $C_z(\bar{u}, \bar{v}, w)$ represent the discretization of the convective terms, $D_x(u, \bar{v}, \bar{w})$, $D_y(\bar{u}, v, \bar{w})$ and $D_z(\bar{u}, \bar{v}, w)$ the discretization of the diffusive terms and $\beta(T^*)$ the Boussinesq buoyancy term which in discrete form reads,

$$\beta(T^*)_{i,j,k+\frac{1}{2}} = -0.5611516 \frac{T_k^* + T_{k+1}^*}{2}. \quad (3.29)$$

The temperature difference between the top and the initial bulk temperature is only 3 °C. The temperature range in this particular case is between 20 and 23 °C where the relation between density and temperature can be assumed to be linear. The coefficient above arises from the non-dimensionalization of the buoyancy term (see (3.14)).

Fig. 3.1 shows the location of variables on a staggered mesh. Interpolations are required to evaluate the kinetic energy conserving convective terms (3.30) and (3.32). For instance at $(x_{i+\frac{1}{2}}, z_k)$ only the u -velocity component is available at that location, while the w -velocity

is only available at $(x_i, z_{k+\frac{1}{2}})$. Hence an interpolation of w to the position where u is defined gives $\bar{w}_{i+\frac{1}{2},k}$. An equivalent procedure for the z -momentum where u needs to be interpolated where w is defined gives $\bar{u}_{i,k+\frac{1}{2}}$. This yields to the discretization of the convective term in (3.26) by a fourth-order central discretization,

$$\begin{aligned}
C_x(u, \bar{v}, \bar{w})_{i+\frac{1}{2},j,k} = & -\frac{1}{2} \left[\frac{1}{-x_{i+\frac{5}{2}} + 8x_{i+\frac{3}{2}} - 8x_{i-\frac{1}{2}} + x_{i-\frac{3}{2}}} \left\{ -u_{i+\frac{5}{2},j,k}(u_{i+\frac{1}{2},j,k} + u_{i+\frac{5}{2},j,k}) \right. \right. \\
& + 8u_{i+\frac{3}{2},j,k}(u_{i+\frac{1}{2},j,k} + u_{i+\frac{3}{2},j,k}) - 8u_{i-\frac{1}{2},j,k}(u_{i+\frac{1}{2},j,k} + u_{i-\frac{1}{2},j,k}) + u_{i-\frac{3}{2},j,k}(u_{i+\frac{1}{2},j,k} + u_{i-\frac{3}{2},j,k}) \left. \right\} \\
& + \frac{1}{-y_{j+2} + 8y_{j+1} - 8y_{j-1} + y_{j-2}} \left\{ -u_{i+\frac{1}{2},j+2,k}(\bar{v}_{i+\frac{1}{2},j,k} + \bar{v}_{i+\frac{1}{2},j+2,k}) \right. \\
& + 8u_{i+\frac{1}{2},j+1,k}(\bar{v}_{i+\frac{1}{2},j,k} + \bar{v}_{i+\frac{1}{2},j+1,k}) - 8u_{i+\frac{1}{2},j-1,k}(\bar{v}_{i+\frac{1}{2},j,k} + \bar{v}_{i+\frac{1}{2},j-1,k}) \\
& + u_{i+\frac{1}{2},j-2,k}(\bar{v}_{i+\frac{1}{2},j,k} + \bar{v}_{i+\frac{1}{2},j-2,k}) \left. \right\} \\
& + \frac{1}{-z_{k+2} + 8z_{k+1} - 8z_{k-1} + z_{k-2}} \left\{ -u_{i+\frac{1}{2},j,k+2}(\bar{w}_{i+\frac{1}{2},j,k} + \bar{w}_{i+\frac{1}{2},j,k+2}) \right. \\
& + 8u_{i+\frac{1}{2},j,k+1}(\bar{w}_{i+\frac{1}{2},j,k} + \bar{w}_{i+\frac{1}{2},j,k+1}) - 8u_{i+\frac{1}{2},j,k-1}(\bar{w}_{i+\frac{1}{2},j,k} + \bar{w}_{i+\frac{1}{2},j,k-1}) \\
& \left. \left. + u_{i+\frac{1}{2},j,k-2}(\bar{w}_{i+\frac{1}{2},j,k} + \bar{w}_{i+\frac{1}{2},j,k-2}) \right\} \right] \tag{3.30}
\end{aligned}$$

The convective terms in the y -direction are discretized in a similar manner.

$$\begin{aligned}
C_y(\bar{u}, v, \bar{w})_{i,j+\frac{1}{2},k} = & -\frac{1}{2} \left[\frac{1}{-y_{j+\frac{5}{2}} + 8y_{j+\frac{3}{2}} - 8y_{j-\frac{1}{2}} + y_{j-\frac{3}{2}}} \left\{ -v_{i,j+\frac{5}{2},k}(v_{i,j+\frac{1}{2},k} + v_{i,j+\frac{5}{2},k}) \right. \right. \\
& + 8v_{i,j+\frac{3}{2},k}(v_{i,j+\frac{1}{2},k} + v_{i,j+\frac{3}{2},k}) - 8v_{i,j-\frac{1}{2},k}(v_{i,j+\frac{1}{2},k} + v_{i,j-\frac{1}{2},k}) + v_{i,j-\frac{3}{2},k}(v_{i,j+\frac{1}{2},k} + v_{i,j-\frac{3}{2},k}) \left. \right\} \\
& + \frac{1}{-x_{i+2} + 8x_{i+1} - 8x_{i-1} + x_{i-2}} \left\{ -v_{i+2,j+\frac{1}{2},k}(\bar{u}_{i,j+\frac{1}{2},k} + \bar{u}_{i+2,j+\frac{1}{2},k}) \right. \\
& + 8v_{i+1,j+\frac{1}{2},k}(\bar{u}_{i,j+\frac{1}{2},k} + \bar{u}_{i+1,j+\frac{1}{2},k}) - 8v_{i-1,j+\frac{1}{2},k}(\bar{u}_{i,j+\frac{1}{2},k} + \bar{u}_{i-1,j+\frac{1}{2},k}) \\
& + v_{i-2,j+\frac{1}{2},k}(\bar{u}_{i,j+\frac{1}{2},k} + \bar{u}_{i-2,j+\frac{1}{2},k}) \left. \right\} \\
& + \frac{1}{-z_{k+2} + 8z_{k+1} - 8z_{k-1} + z_{k-2}} \left\{ -v_{i,j+\frac{1}{2},k+2}(\bar{w}_{i,j+\frac{1}{2},k} + \bar{w}_{i,j+\frac{1}{2},k+2}) \right. \\
& + 8v_{i,j+\frac{1}{2},k+1}(\bar{w}_{i,j+\frac{1}{2},k} + \bar{w}_{i,j+\frac{1}{2},k+1}) - 8v_{i,j+\frac{1}{2},k-1}(\bar{w}_{i,j+\frac{1}{2},k} + \bar{w}_{i,j+\frac{1}{2},k-1}) \\
& \left. \left. + v_{i,j+\frac{1}{2},k-2}(\bar{w}_{i,j+\frac{1}{2},k} + \bar{w}_{i,j+\frac{1}{2},k-2}) \right\} \right] \tag{3.31}
\end{aligned}$$

The convective terms in the z -direction are discretized in a similar manner.

$$\begin{aligned}
C_z(\bar{u}, \bar{v}, w)_{i,j,k+\frac{1}{2}} = & -\frac{1}{2} \left[\frac{1}{-z_{k+\frac{5}{2}} + 8z_{k+\frac{3}{2}} - 8z_{k-\frac{1}{2}} + z_{k-\frac{3}{2}}} \left\{ -w_{i,j,k+\frac{5}{2}}(w_{i,j,k+\frac{1}{2}} + w_{i,j,k+\frac{5}{2}}) \right. \right. \\
& + 8w_{i,j,k+\frac{3}{2}}(w_{i,j,k+\frac{1}{2}} + w_{i,j,k+\frac{3}{2}}) - 8w_{i,j,k-\frac{1}{2}}(w_{i,j,k+\frac{1}{2}} + w_{i,j,k-\frac{1}{2}}) + w_{i,j,k-\frac{3}{2}}(w_{i,j,k+\frac{1}{2}} + w_{i,j,k-\frac{3}{2}}) \left. \right\} \\
& + \frac{1}{-x_{i+2} + 8x_{i+1} - 8x_{i-1} + x_{i-2}} \left\{ -w_{i+2,j+\frac{1}{2},k}(\bar{u}_{i,j,k+\frac{1}{2}} + \bar{u}_{i+2,j,k+\frac{1}{2}}) \right. \\
& + 8u_{i+1,j,k+\frac{1}{2}}(\bar{u}_{i,j,k+\frac{1}{2}} + \bar{u}_{i+1,j,k+\frac{1}{2}}) - 8w_{i-1,j,k+\frac{1}{2}}(\bar{u}_{i,j,k+\frac{1}{2}} + \bar{u}_{i-1,j,k+\frac{1}{2}}) \\
& + w_{i-2,j,k+\frac{1}{2}}(\bar{u}_{i,j,k+\frac{1}{2}} + \bar{u}_{i-2,j,k+\frac{1}{2}}) \left. \right\} \\
& + \frac{1}{-y_{j+2} + 8y_{j+1} - 8y_{j-1} + y_{j-2}} \left\{ -w_{i+\frac{1}{2},j+2,k}(\bar{v}_{i,j,k+\frac{1}{2}} + \bar{v}_{i,j+2,k+\frac{1}{2}}) \right. \\
& + 8w_{i,j+1,k+\frac{1}{2}}(\bar{v}_{i,j,k+\frac{1}{2}} + \bar{v}_{i,j+1,k+\frac{1}{2}}) - 8w_{i,j-1,k+\frac{1}{2}}(\bar{v}_{i,j,k+\frac{1}{2}} + \bar{v}_{i,j-1,k+\frac{1}{2}}) \\
& \left. \left. + w_{i,j-2,k+\frac{1}{2}}(\bar{v}_{i,j,k+\frac{1}{2}} + \bar{v}_{i,j-2,k+\frac{1}{2}}) \right\} \right] \quad (3.32)
\end{aligned}$$

The diffusive terms $D_x(u, \bar{v}, \bar{w})_{i+\frac{1}{2},j,k}$, $D_y(\bar{u}, v, \bar{w})_{i,j+\frac{1}{2},k}$ and $D_z(\bar{u}, \bar{v}, w)_{i,j,k+\frac{1}{2}}$ are discretized using the fourth-order accurate central discretization scheme for the second derivative which reads

$$\begin{aligned}
D_x(u, \bar{v}, \bar{w})_{i+\frac{1}{2},j,k} = & \frac{-u_{i+\frac{5}{2},j,k} + 16u_{i+\frac{3}{2},j,k} - 30u_{i+\frac{1}{2},j,k} + 16u_{i-\frac{1}{2},j,k} - u_{i-\frac{3}{2},j,k}}{12(\delta x_{i+\frac{1}{2}})^2} \quad (3.33) \\
& + \frac{-\bar{u}_{i,j+\frac{5}{2},k} + 16\bar{u}_{i,j+\frac{3}{2},k} - 30\bar{u}_{i,j+\frac{1}{2},k} + 16\bar{u}_{i,j-\frac{1}{2},k} - \bar{u}_{i,j-\frac{3}{2},k}}{12(\delta y_{j+\frac{1}{2}})^2} \\
& + \frac{-\bar{u}_{i,j,k+\frac{5}{2}} + 16\bar{u}_{i,j,k+\frac{3}{2}} - 30\bar{u}_{i,j,k+\frac{1}{2}} + 16\bar{u}_{i,j,k-\frac{1}{2}} - \bar{u}_{i,j,k-\frac{3}{2}}}{12(\delta z_{k+\frac{1}{2}})^2}
\end{aligned}$$

and

$$\begin{aligned}
D_y(\bar{u}, v, \bar{w})_{i,j+\frac{1}{2},k} = & \frac{-\bar{v}_{i+\frac{5}{2},j,k} + 16\bar{v}_{i+\frac{3}{2},j,k} - 30\bar{v}_{i+\frac{1}{2},j,k} + 16\bar{v}_{i-\frac{1}{2},j,k} - \bar{v}_{i-\frac{3}{2},j,k}}{12(\delta x_{i+\frac{1}{2}})^2} \quad (3.34) \\
& + \frac{-v_{i,j+\frac{5}{2},k} + 16v_{i,j+\frac{3}{2},k} - 30v_{i,j+\frac{1}{2},k} + 16v_{i,j-\frac{1}{2},k} - v_{i,j-\frac{3}{2},k}}{12(\delta y_{j+\frac{1}{2}})^2} \\
& + \frac{-\bar{v}_{i,j,k+\frac{5}{2}} + 16\bar{v}_{i,j,k+\frac{3}{2}} - 30\bar{v}_{i,j,k+\frac{1}{2}} + 16\bar{v}_{i,j,k-\frac{1}{2}} - \bar{v}_{i,j,k-\frac{3}{2}}}{12(\delta z_{k+\frac{1}{2}})^2}
\end{aligned}$$

and

$$\begin{aligned}
D_z(\bar{u}, \bar{v}, w)_{i,j,k+\frac{1}{2}} = & \frac{-\bar{w}_{i+\frac{5}{2},j,k} + 16\bar{w}_{i+\frac{3}{2},j,k} - 30\bar{w}_{i+\frac{1}{2},j,k} + 16\bar{w}_{i-\frac{1}{2},j,k} - \bar{w}_{i-\frac{3}{2},j,k}}{12(\delta x_{i+\frac{1}{2}})^2} \\
& + \frac{-\bar{w}_{i,j+\frac{5}{2},k} + 16\bar{w}_{i,j+\frac{3}{2},k} - 30\bar{w}_{i,j+\frac{1}{2},k} + 16\bar{w}_{i,j-\frac{1}{2},k} - \bar{w}_{i,j-\frac{3}{2},k}}{12(\delta y_{j+\frac{1}{2}})^2} \\
& + \frac{-w_{i,j,k+\frac{5}{2}} + 16w_{i,j,k+\frac{3}{2}} - 30w_{i,j,k+\frac{1}{2}} + 16w_{i,j,k-\frac{1}{2}} - w_{i,j,k-\frac{3}{2}}}{12(\delta z_{k+\frac{1}{2}})^2}
\end{aligned} \tag{3.35}$$

where $\delta x_{i+\frac{1}{2}} = x_i - x_{i+1}$, $\delta y_{j+\frac{1}{2}} = y_j - y_{j+1}$ and $\delta z_{k+\frac{1}{2}} = z_k - z_{k+1}$ where the coefficients on non-uniform meshes are determined using Lagrange interpolations.

3.5 Discretization of the convection-diffusion equation of the scalar φ with WENO scheme

The scheme that is employed here is a variant of the WENO5 scheme as described by Liu et al. [61]. The WENO schemes use an approximation of the scalar fluxes at the cell interface by employing interpolation schemes. The reconstruction procedure produces a high order accurate approximation to the solution from the calculated cell averages.

In this section we briefly outline the discretization of the transport equation for the scalar φ . The three-dimensional convection diffusion equation of $\varphi = \varphi(x, y, z, t)$ reads

$$\frac{\partial \varphi}{\partial t} + u \frac{\partial \varphi}{\partial x} + v \frac{\partial \varphi}{\partial y} + w \frac{\partial \varphi}{\partial z} = \Gamma \left(\frac{\partial^2 \varphi}{\partial x^2} + \frac{\partial^2 \varphi}{\partial y^2} + \frac{\partial^2 \varphi}{\partial z^2} \right), \tag{3.36}$$

where x, y and z are the horizontal and vertical directions, respectively and t denotes time. The diffusive term on the right is discretized using a fourth-order accurate central scheme, while the convective term is discretized using a variant of the fifth-order WENO scheme developed by Liu et al. [61]. Below, the implemented scheme is detailed only in one dimension. Generalization to higher dimensions is straightforward.

When ignoring the diffusive term, the one dimensional variant of (3.36) can be rewritten as

$$\frac{\partial \varphi}{\partial t} = -\frac{\partial(u\varphi)}{\partial x}. \quad (3.37)$$

where u is the velocity in the x -direction. As we employ a staggered mesh, for the volume centred around $x = x_i$, the convective fluxes R_i^+ and R_i^- are defined by

$$R_i^+ = \frac{a_0}{a_0 + a_1 + a_2} P_{i-1}(x_{i+\frac{1}{2}}) + \frac{a_1}{a_0 + a_1 + a_2} P_i(x_{i+\frac{1}{2}}) + \frac{a_2}{a_0 + a_1 + a_2} P_{i+1}(x_{i+\frac{1}{2}}) \quad (3.38)$$

and

$$R_i^- = \frac{a_0}{a_0 + a_1 + a_2} P_{i-1}(x_{i-\frac{1}{2}}) + \frac{a_1}{a_0 + a_1 + a_2} P_i(x_{i-\frac{1}{2}}) + \frac{a_2}{a_0 + a_1 + a_2} P_{i+1}(x_{i-\frac{1}{2}}) \quad (3.39)$$

where a_0, a_1, a_2 are weights and P the Lagrange interpolations polynomials defined in (3.42). In the above, the weights for the convex combination of the quadratic Lagrange interpolation polynomials are given by,

$$\begin{aligned} a_0 &= \frac{1}{12(\varepsilon - IS_i)^3} \\ a_1 &= \frac{1}{2(\varepsilon - IS_{i+1})^3} \\ a_2 &= \frac{1}{4(\varepsilon - IS_{i+2})^3} \end{aligned} \quad (3.40)$$

where $\varepsilon = 10^{-9}$ and the smoothness indicator IS_i is defined by

$$IS_i = \frac{1}{2}((\varphi_{i-1} - \varphi_{i-2})^2 + (\varphi_i - \varphi_{i-1})^2) + (\varphi_i - 2\varphi_{i-1} + \varphi_{i-2})^2. \quad (3.41)$$

The modified quadratic Lagrange interpolations $P_i(x)$ in equations (3.38) and (3.39) read

$$\begin{aligned} P_i(x) &= \frac{(x-x_i)(x-x_{i+1})}{(x_{i-1}-x_i)(x_{i-1}-x_{i+1})} \varphi_{i-1} + \frac{(x-x_{i-1})(x-x_{i+1})}{(x_i-x_{i-1})(x_i-x_{i+1})} \varphi_i + \frac{(x-x_{i-1})(x-x_i)}{(x_{i+1}-x_{i-1})(x_{i+1}-x_i)} \varphi_{i+1} \\ &\quad - \frac{(x_i-x_{i-1})\varphi_{i+1} - (x_{i+1}-x_{i-1})\varphi_i + (x_{i+1}-x_i)\varphi_{i-1}}{12(x_{i+1}-x_i)} \end{aligned} \quad (3.42)$$

High-order polynomial interpolations to the midpoints $x_{i+\frac{1}{2}}$ are computed using known grid values of the scalar φ . The scheme uses a 5-points stencil which is divided into three 3-points stencils as shown in Fig. 3.2.

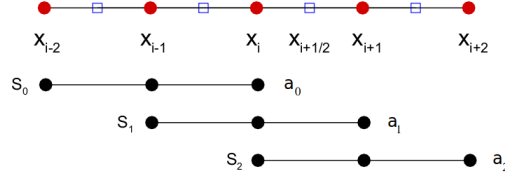


Figure 3.2: Schematic illustration of the weighted 5 point convex combination composed of three 3-points stencils S_0, S_1, S_2 and their respective weights a_0, a_1, a_2 used in the classical WENO5 scheme. [82].

These three-point interpolations of the scalar to the faces of the volume are combined with a smoothing term at the right. Using the above, depending on the signs of $u_{i-\frac{1}{2}}$ and $u_{i+\frac{1}{2}}$, we have four possible ways to calculate the discretization of the convective terms $L_i(\varphi) = \left(-u \frac{\partial \varphi}{\partial x}\right)|_{x_i}$ in x_i :

$$u_{i+\frac{1}{2}} > 0, u_{i-\frac{1}{2}} > 0 : L_i(\varphi) = -\frac{u_{i+\frac{1}{2}} R_i^+ - u_{i-\frac{1}{2}} R_{i-1}^+}{x_{i+\frac{1}{2}} - x_{i-\frac{1}{2}}} \quad (3.43)$$

$$u_{i+\frac{1}{2}} > 0, u_{i-\frac{1}{2}} < 0 : L_i(\varphi) = -\frac{u_{i+\frac{1}{2}} R_i^+ - u_{i-\frac{1}{2}} R_i^-}{x_{i+\frac{1}{2}} - x_{i-\frac{1}{2}}} \quad (3.44)$$

$$u_{i+\frac{1}{2}} < 0, u_{i-\frac{1}{2}} > 0 : L_i(\varphi) = -\frac{u_{i+\frac{1}{2}} R_{i+1}^- - u_{i-\frac{1}{2}} R_{i-1}^+}{x_{i+\frac{1}{2}} - x_{i-\frac{1}{2}}} \quad (3.45)$$

$$u_{i+\frac{1}{2}} < 0, u_{i-\frac{1}{2}} < 0 : L_i(\varphi) = -\frac{u_{i+\frac{1}{2}} R_{i+1}^- - u_{i-\frac{1}{2}} R_i^-}{x_{i+\frac{1}{2}} - x_{i-\frac{1}{2}}} \quad (3.46)$$

The diffusive term on the right hand side of (3.36) is discretized using a fourth-order central finite difference method for the second derivative with,

$$\frac{\partial^2 \varphi}{\partial x^2} \approx \frac{-\varphi_{i+2,k} + 16\varphi_{i+1,k} - 30\varphi_{i,k} + 16\varphi_{i-1,k} - \varphi_{i-2,k}}{12(\delta x_i)^2} \quad (3.47)$$

and

$$\frac{\partial^2 \varphi}{\partial z^2} \approx \frac{-\varphi_{i,k+2} + 16\varphi_{i,k+1} - 30\varphi_{i,k} + 16\varphi_{i,k-1} - \varphi_{i,k-2}}{12(\delta z_k)^2}, \quad (3.48)$$

where $\delta x_i = \frac{1}{2}(x_{i+\frac{1}{2}} - x_{i-\frac{1}{2}})$ and $\delta z_i = \frac{1}{2}(z_{i+\frac{1}{2}} - z_{i-\frac{1}{2}})$, respectively. On a stretched mesh the actual discretisation coefficients are obtained from the above equations using Lagrange interpolations. The time integration of the convection-diffusion equation is implemented using a third order Runge-Kutta method (RK3) developed by Shu and Osher [82] that reads,

$$\begin{aligned} \varphi_i^{(1)} &= \varphi_i^{(n)} + \Delta t L_i(\varphi_i^{(n)}) \\ \varphi_i^{(2)} &= \frac{3}{4}\varphi_i^{(n)} + \frac{1}{4}\varphi_i^{(1)} + \frac{1}{4}\Delta t L_i(\varphi_i^{(1)}) \\ \varphi_i^{(n+1)} &= \frac{1}{3}\varphi_i^{(n)} + \frac{2}{3}\varphi_i^{(2)} + \frac{2}{3}\Delta t L_i(\varphi_i^{(2)}) \end{aligned} \quad (3.49)$$

In the case of using three quadratic interpolations a fifth-order accuracy can be achieved. Note that the weights given to the interpolating polynomials depend on the local smoothness of the solution. Interpolation polynomials defined in regions where the solution is smooth are given higher weights than those in regions near discontinuities (shocks) or steep gradients (like the gas concentration near the interface in this case).

3.6 Dual Mesh Approach

Because the diffusivity of the scalars of interest is up to three orders smaller than that of the momentum, the resolution requirements for the flow field are less stringent as will be shown later by the mesh refinement tests in Section 4.3. To save computing time a dual mesh approach is used as illustrated in Fig. 3.3. The velocity is solved on a coarser base mesh (Fig. 3.1), while the scalar is defined on the finer subgrid (Fig. 3.3b and 3.3c) so that the required computational resources are significantly reduced.

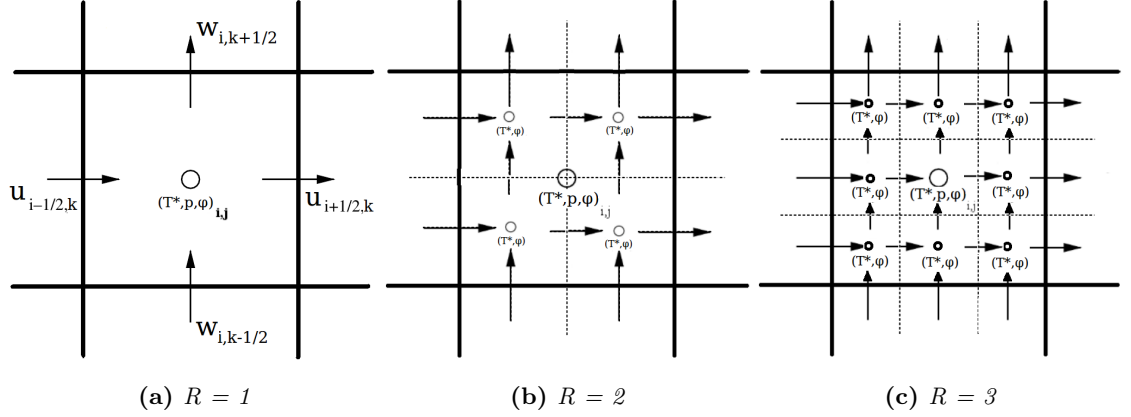


Figure 3.3: Variables on the new dual mesh. The flow field is solved on the outer coarse mesh, whilst the scalar is computed on a refined subgrid. For the transport of the scalar the velocities are interpolated onto the midpoints of the subgrid

To calculate the convective transport of the scalar the velocities are interpolated onto the finer subgrid using a fourth-order interpolation. When employing a subgrid refinement by a factor of $R = 2$ (Fig. 3.3b) an interpolation is required for each subcell as the velocity location and the scalar locations do not coincide with their counter parts on the base mesh. In contrast Fig. 3.3c shows that in the case of a subgrid refinement by a factor $R = 3$ some velocities and the central subcells for the scalars are defined at the same locations.

3.7 Implementation of Boundary Conditions

Dirichlet and Neumann boundary conditions are implemented by extrapolating the values obtained at the latest time step to ghost cells outside of the computational domain. This has the advantage that there is no need to change the numerical stencils near boundaries. Suppose the quantity q is defined on an N -point mesh and we want to implement a Dirichlet (odd) boundary condition $q_N = Q$. By using the known values $q_{\frac{1}{2}}, q_{\frac{3}{2}}, \dots, q_{N-\frac{1}{2}}$, the values $q_{N+i-\frac{1}{2}}$ are determined by using the formula

$$q_{N+i-\frac{1}{2}} = 2Q - q_{N-i+\frac{1}{2}} \text{ for } i = 1, \dots, 3. \quad (3.50)$$

To implement the Neumann (even) boundary condition at $i = 0$, we use the formula

$$q_{-i+\frac{1}{2}} = q_{i-\frac{1}{2}} \text{ for } i = 1, \dots, 3. \quad (3.51)$$

The free-slip condition for the velocity is implemented by using a Neumann boundary condition (3.51) of the velocity component that is parallel to the boundary and a Dirichlet boundary condition (3.50) for the component that is orthogonal to the boundary (using the value zero at the boundary itself).

3.8 Parallelization

The calculations are carried out using parallel computing. For simplicity the parallelization procedure is described here in one dimension only. In the following only the communication in x -direction on a vertical boundary is detailed. The procedure is the same in the other directions. Parallel computing is a powerful method to cut down computation time by letting multiple processors work simultaneously. The basic idea is to divide the computational domain into smaller subdomains which are solved simultaneously on various processors. If the subdomains are of similar size (i.e. have the same number of cells) the computation time for each subdomain is nearly the same which makes the computation very efficient. This method implies a certain level of communication between the processes as the variable's values at the interfaces between the processes need to be known. Values in one process will influence its neighbouring process and vice versa. The 2-dimensional domain is divided into subdomains as shown schematically in Fig. 3.4.

Each subdomain has a cartesian mesh defined as $\Delta x_i, i = 0, \dots, N_x$ and $\Delta z_k, k = 0, \dots, N_z$ and the computation of each domain runs as its own process (i.e. on its own assigned processor). Considering two neighbouring processes A and B , as illustrated in figure 3.4, and *one* scalar variable to be stored on the grid denoted \bar{A} when used in process A and \bar{B} when used in process B . The gridpoints of each domain are illustrated as circles for process A and diamonds for process B . There is a communication required between the two processes A and B as, for instance, the scalar values of \bar{B} will act as a boundary condition for process A and vice versa. The thick lines in the centre of the zoomed view on the right in figure 3.4

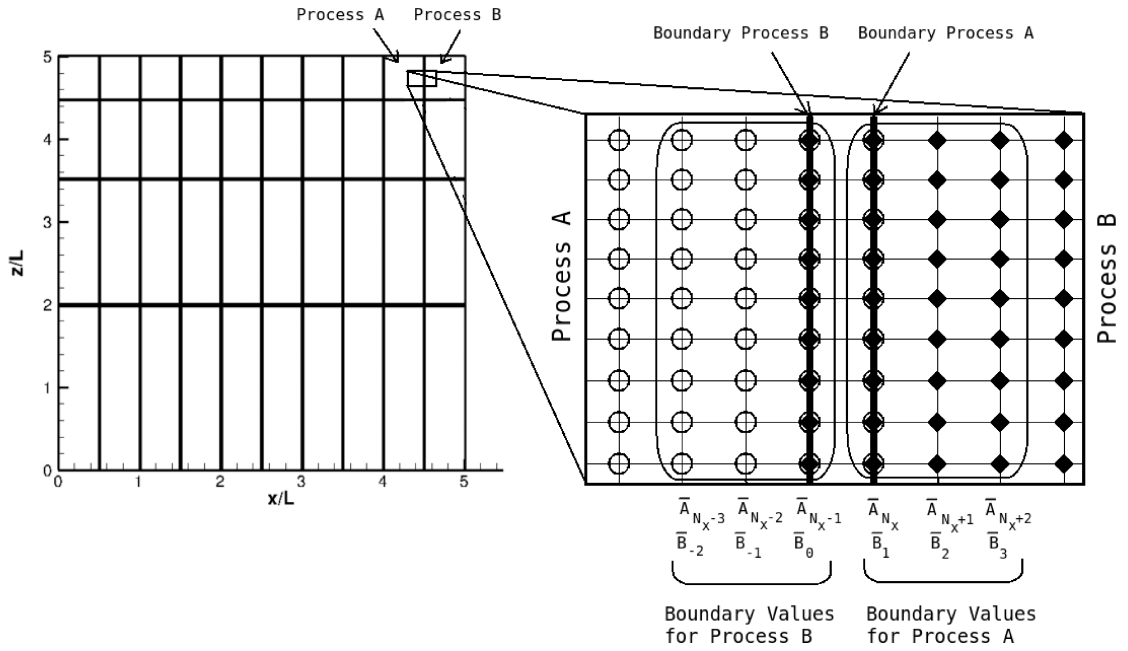


Figure 3.4: *Schematic parallelization procedure*

are the domain boundaries. As can be seen in the illustration the gridpoints are shared and overlap. The interfaces are part of either domain and represent the boundary. However, the numerical method used requires more than one boundary value. For instance, the WENO5 scheme described in Section 3.5 requires 2 additional gridpoints at either side as it uses a 5 point stencil (see Fig. 3.2). Therefore the first two points 'behind' the boundary act as a boundary condition too. Three values \bar{A}_{N_x-3} , \bar{A}_{N_x-2} and \bar{A}_{N_x-1} act as a boundary condition for process *B* and \bar{B}_1 , \bar{B}_2 and \bar{B}_3 act as a boundary condition for process *A*. These values need to be passed from one process to the other. Once these 'ghost points' are known each process can start its iteration without requesting more information from the neighbouring process as all boundary values are known. After each time step n the boundary values for process *A* are updated so that

$$\overline{A}_{N_x}^{n+1} = \overline{B}_1^n \quad (3.52)$$

$$\overline{A}_{N_x+1}^{n+1} = \overline{B}_2^n \quad (3.53)$$

$$\overline{A}_{N_x+3}^{n+1} = \overline{B}_3^n \quad (3.54)$$

and for process B so that

$$\overline{B}_{-2}^{n+1} = \overline{A}_{N_x-3}^n \quad (3.55)$$

$$\overline{B}_{-1}^{n+1} = \overline{A}_{N_x-2}^n \quad (3.56)$$

$$\overline{B}_0^{n+1} = \overline{A}_{N_x-1}^n. \quad (3.57)$$

The near interface points of one domain act as 'ghost boundary points' for the neighbouring domain. The above description outlines the general method of parallelization used here for exchanging grid data between neighbouring processes. Note that in the actual simulations the variables in question are the velocities and scalar quantities as shown in Fig. 3.1. The data exchange between the processes is realized using the well established Message Passing Interface protocol (MPI). Each process can run on its own assigned processor with distributed memory.

Chapter 4

Numerical Experiments

To determine the accuracy of the numerical method described in Chapter 3 a series of numerical experiments has been carried out. Scalar transport problems were tested in one and two-dimensional numerical experiments. The first part covers 1D numerical experiments. The advantage of the 1D experiments is that they are much less costly in terms of computational effort which enabled a detailed grid sensitivity study of the numerical method. Furthermore there often exists an analytical solution for 1D transport problems so an exact error of the numerical method can be calculated. For instance, the propagation of a wave by means of convection is easily predictable when that convection is in only one direction with a given constant velocity. It is simply to be shifted along that direction. As the problem of gas transfer at the air-water interface is a convection-diffusion problem one dimensional scalar transport was tested for problems which were either purely convective or purely diffusive. These experiments enabled the determination of the order of accuracy of the numerical scheme used to solve the diffusive and convective terms respectively. Comparisons with an alternative WENO scheme and the 5th order upwind central method were conducted.

In the second part two-dimensional numerical experiments were carried out. A mesh sensitivity study revealed the order of accuracy for a two-dimensional scalar distribution in an inviscid sheared flow. A mesh sensitivity study for scalar transfer in a buoyancy driven 2D flow could clearly identify a minimum mesh size to accurately resolve the scalar convection-

diffusion of a low diffusive scalar ($Sc = 500$). As these parameters correspond to air-water gas transfer these findings were of great importance for the resolution requirements of the full 3D gas transfer simulations. The alternative WENO scheme and 5th order upwind central method were also tested for this buoyancy driven case.

4.1 1D Numerical Experiments

In the following section the WENO-scheme is applied for different test problems with the purpose to predict the accuracy of the method on uniform and stretched meshes, respectively. As scalar transport is not purely convective problem the fourth-order central discretization of diffusion is also tested on non uniform meshes.

4.1.1 Scalar transport by convection on a uniform grid

By using the modified quadratic Lagrange interpolations for reconstruction (3.42) it is expected to achieve a fifth-order accuracy for the convective scalar transport on uniform meshes. In both of the following cases (uniform and non-uniform meshes), the previously described WENO schemes for spatial discretization and the 3rd-order Runge-Kutta-scheme for time integration of the one-dimensional convection equation is used. Because a prediction of the numerical error in the WENO scheme is desired, the diffusive terms will not be solved. If $\varphi(x_i, t)$ and φ_{exact} are the numerical and the exact solutions, respectively at (x_i, t) , the L_1 discretization error is given by

$$L_1 = \frac{1}{N} \sum_{i=1}^N | \varphi(x_i, t) - \varphi_{exact} |, \quad (4.1)$$

where N describes the number of nodes in the domain, t the time, i the node number.

The scalar distribution is initialized by a sine wave function $\varphi_0(x) = \sin(\pi x)$. The discrete representation of the curve on a 10 point grid is depicted in Figure 4.1. The wave was convected with a constant velocity in x direction with periodic boundary condition at the sides. In the calculations an extremely small CFL-number was used so that the time-step would be small enough to ensure that the third-order temporal behaviour of the Runge-Kutta scheme would not affect the rate of convergence of the WENO schemes.

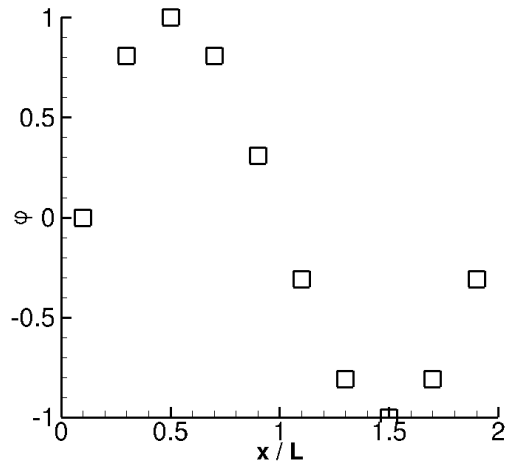


Figure 4.1: *The sine wave used for 1D convection test on a 10-point mesh*

Table 4.1 gives the L_1 error after running the simulation during one time-unit as well as the resulting order of accuracy. The WENO5 implementation of Liu et al. [61] was compared to the alternative WENO5 scheme developed by Shu and Jiang [81] and the upstream central method that is obtained by selecting the smoothness indicators $IS_i = 0$ in either of the WENO schemes (see equation (3.41)). Starting from $N = 10$ nodes the L_1 error is decreasing when increasing the number of nodes to 20, 40, ..., 640. As previously found by Shu and Jiang [81], the implementation of Liu et al. [61] shows a smaller error than the scheme of Shu and Jiang [81] on the coarse 10-point mesh while on finer meshes the Shu and Jiang [81] implementation is superior.

Furthermore, the scheme of Shu and Jiang [81] as well as the upstream central scheme show a fifth-order behaviour, while the original scheme of Liu et al. [61] would need an even finer mesh to exhibit this behaviour. With the mesh sizes shown in the table, a significant increase of ε (even up to a value of $\varepsilon = 1$) would be required to achieve higher order. The choice of the small $\varepsilon = 10^{-6}$ was necessary for the present application in order to resolve very steep gradients. To test whether the Liu et al. [61] scheme has the potential to exhibit a fifth-order behaviour, an additional test had been carried out in which ε was increased to $\varepsilon = 1$ (Table 4.2). As can be seen in Table 4.2 for $\varepsilon = 1$, indeed a fifth order behaviour for

WENO-Liu et al. [61]			WENO-Shu and Jiang [81]			Upstream Central		
N	L_1 -error	order	N	L_1 -error	order	N	L_1 -error	order
10	1.17 E-02	-	10	2.11 E-02	-	10	3.11 E-03	-
20	2.47 E-03	2.24	20	1.10 E-03	4.27	20	1.01 E-04	4.95
40	3.30 E-04	2.90	40	3.26 E-05	5.07	40	3.18 E-06	4.99
80	2.53 E-05	3.70	80	9.98 E-07	5.03	80	9.99 E-08	4.99
160	1.57 E-06	4.01	160	3.12 E-08	5.00	160	3.15 E-09	4.99
320	6.13 E-08	4.68	320	9.76 E-10	5.00	320	1.03 E-10	4.94
640	1.04 E-09	5.89	640	3.13 E-11	4.96	640	4.26 E-12	4.59

Table 4.1: Absolute error and order of convergence on uniform meshes with $\varepsilon = 10^{-6}$.

the original scheme was observed for $N \geq 80$ grid points. The slight decrease in order of convergence for $N = 640$ points is possibly caused by machine-accuracy limitations affecting the calculations.

In practical calculations the mesh will be relatively coarse so that the original WENO implementation of Liu et al. [61], which has a good accuracy on coarse meshes, would be a good choice. Though the fifth-order upstream central method is shown to be even more accurate on coarse meshes, it is not the method of choice as the absence of a mechanism to deal with steep gradients could result in the appearance of wiggles as will be briefly discussed in Section 4.3.1.

4.1.2 Scalar transport by convection on non-uniform meshes

Using the modified Lagrange interpolations (see eqn. (3.42)) the WENO-scheme has been applied on non-uniform meshes where the node distribution is given by:

$$x(i) = \left[1 - \frac{\tanh(x_\phi)}{\tanh(x_1)}\right] x(0) + \left[\frac{\tanh(x_\phi)}{\tanh(x_1)}\right] x(n_x) \quad (4.2)$$

WENO-Liu et al. [61]		
N	L_1 -error	order
10	3.46E-03	-
20	1.76E-04	4.30E+00
40	2.83E-06	5.96E+00
80	9.44E-08	4.91E+00
160	3.11E-09	4.92E+00
320	1.02E-10	4.93E+00
640	4.26E-12	4.59E+00

Table 4.2: Absolute error and order of convergence on uniform meshes with $\varepsilon = 1$.

for $i = 1, \dots, n_x - 1$, with

$$\begin{aligned} x_\phi &= \delta_s/2 \frac{i}{n_x} \\ x_1 &= \delta_s/2. \end{aligned}$$

The procedure for the stretching is controlled by the parameter δ_s . The N -point mesh distribution is so that $x(0) = 0$ and $x(n_x) = 1$ where $n_x = N/2$. The resulting mesh is subsequently mirrored about $x = 1$ to obtain the grid points between $x(n_x) = 1$ and $x(N) = 2$.

The results of the tests using $\delta_s = 1.0$ and 3.0 , respectively, are presented in Table 4.3. The absolute errors, as expected, are smaller for the mesh with reduced stretching. Compared to uniform meshes it can be seen that the order of accuracy decreases to approximately 2.

4.1.3 Scalar transport: pure diffusion

In this section the fourth-order accurate central discretization (3.47) for the solution of scalar diffusion is applied. In the one-dimensional case, concentration gradients in the y - and z -directions are assumed to be zero, so that the one-dimensional diffusion equation for a scalar

$\delta_s = 1.0$			$\delta_s = 3.0$		
N	L ₁ -error	L ₁ -order	N	L ₁ -error	L ₁ -order
10	1.20E-02	-	10	3.58E-02	-
20	2.41E-03	2.32E+00	20	6.28E-03	2.51E+00
40	3.91E-04	2.63E+00	40	1.60E-03	1.98E+00
80	6.27E-05	2.64E+00	80	3.77E-04	2.08E+00
160	1.41E-05	2.15E+00	160	9.26E-05	2.03E+00
320	3.45E-06	2.03E+00	320	2.31E-05	2.00E+00
640	8.62E-07	2.00E+00	640	5.77E-06	2.00E+00

Table 4.3: Absolute error and order of convergence on non-uniform meshes with $\varepsilon = 10^{-6}$.

$\varphi(x, t)$ reads

$$\frac{\partial \varphi}{\partial t} = D \frac{\partial^2 \varphi}{\partial x^2}. \quad (4.3)$$

For the test a one-dimensional domain was chosen with $0 \leq x \leq 5L$. A mesh with N grid points was defined with a refinement near the surface where the concentration boundary layer will form (see Section 4.1.2). At $x = 0$ the boundary condition $\varphi(0, t) = 1$ was imposed. The analytical solution for this boundary value problem is given by

$$\varphi(x, t) = 1 - \operatorname{erf} \left(\frac{x}{\sqrt{4Dt}} \right). \quad (4.4)$$

The initial condition for the test was given by the analytical solution as defined in (4.4) at $t=10$ seconds. In the case of diffusive gas transfer into a liquid $D = \frac{1}{ReSc}$ and for the transfer of oxygen into water we have a Schmidt number of $Sc = 500$ and a Reynolds number of $Re = 100$, which is based on a characteristic length scale of $L = 1$ cm and a characteristic velocity of $u = 1$ cm/s. The latter gives us a characteristic time scale of $\theta = L/U = 1$ second.

The absolute errors and order of accuracy for the pure diffusion scalar transport on non-uniform meshes were tested for $N = 10$ to 640 grid points. The results after 1 time-unit are shown in Table 4.4. The absolute errors in the numerical results are very small, illustrating

$\delta_s = 3.0$			$\delta_s = 4.5$		
N	L ₁ -error	L ₁ -order	N	L ₁ -error	L ₁ -order
10	1.47E-04	-	10	1.27E-03	-
20	2.22E-04	-5.95E-01	20	3.26E-04	1.96E+00
40	2.45E-04	-1.41E-01	40	2.53E-05	3.69E+00
80	2.11E-05	3.54E+00	80	1.50E-06	4.07E+00
160	1.73E-06	3.61E+00	160	1.00E-07	3.91E+00
320	1.12E-07	3.95E+00	320	6.72E-09	3.90E+00
640	7.19E-09	3.96E+00	640	4.37E-10	3.94E+00

Table 4.4: Absolute error and order of convergence on non-uniform meshes for pure diffusion case.

very good agreement with the analytical solution. A fourth order accuracy is achieved even with increased stretching.

All 1D numerical tests described above (Sections 4.1.1 to 4.1.3) illustrate the advantageous behaviour of the chosen combination of a WENO-scheme with a fourth-order discretization of the diffusive terms which resulted in a low numerical diffusion and small absolute errors for both modes of transport, pure convection and pure diffusion, respectively.

4.2 Two dimensional sheared scalar distribution

To further test the robustness of the numerical scheme, mesh sensitivity tests in 2D for two application cases were performed, namely for sheared scalar distribution and low-diffusivity scalar transport in buoyancy driven flow. The first problem deals with a smooth scalar distribution without scalar diffusion being sheared by a zero viscosity flow as shown in Figure 4.2. After 1 time-unit the flow is reversed with the aim to obtain the initial distribution of the scalar back so that the distribution at $t = 0$ should be the same as at $t = 2$.

The simulation was run on a $5L \times 5L$ domain using periodic boundary conditions in the horizontal direction and free-slip boundary conditions for the velocity combined with zero-flux

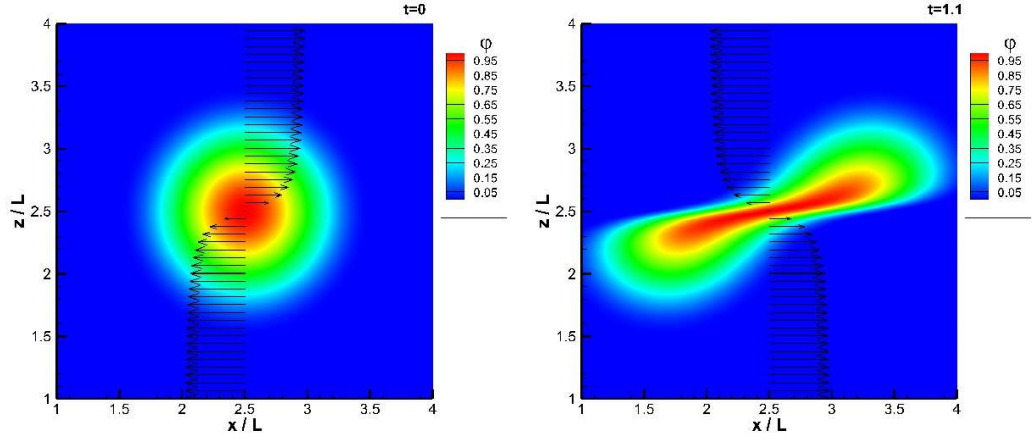


Figure 4.2: A detail of the sheared scalar distribution. a) at $t=0$ second and b) at $t=1.1$ seconds.

boundary conditions (3.51) for the scalar along the upper and lower boundaries. At $t = 0$, the scalar field was initialised by

$$\varphi_{i,k} = 0.5 \left(1 + \cos(\pi \sqrt{(x_i - 2.5)^2 + (z_k - 2.5)^2}) \right), \quad (4.5)$$

while the flow field was initialised using

$$u_{i+\frac{1}{2},k} = 2 \frac{\text{atan}(10(z_k - 2.5))}{\pi}. \quad (4.6)$$

At $t = 1$ second the flow field was reversed, so that

$$u_{i+\frac{1}{2},k} = -2 \frac{\text{atan}(10(z_k - 2.5))}{\pi}. \quad (4.7)$$

After $t = 2$ seconds of simulation the error is determined by comparing the initial to the calculated scalar distribution. As can be seen in Table 4.5, a grid refinement study was carried out by performing simulations on a sequence of uniform meshes with 80×80 up to 640×640 points. With increasing number of grid points the order of accuracy was found to increase significantly from about 2 to 4.

$n_x \times n_z$	L_1 -error	L_1 -order
40×40	1.34E-03	-
80×80	3.51E-04	1.93E+00
160×160	7.30E-05	2.26E+00
320×320	9.33E-06	2.97E+00
640×640	5.92E-07	3.98E+00

Table 4.5: Absolute error and order of convergence resulting from the 2D sheared scalar distribution test on uniform meshes using the WENO scheme of Liu et al. [61] with $\varepsilon = 10^{-6}$.

4.3 Two-dimensional low-diffusivity scalar transport in buoyancy driven flow

The second 2D application case considers the problem of low-diffusivity (high Schmidt number) mass transfer in buoyant-convectively driven flow. An example in nature is the oxygen absorption through the air-water interface in lakes at night time when the lakes' surface is cooled by the overlying cold air leading to an unstable stratification which in turn causes mixing at the water side.

The description of the 2D numerical setup for the problem is as follows. A square domain was chosen with an edge length of $5L$ as illustrated in Fig. 4.3 The base grid size was $n_x = 400$ and $n_z = 256$ in the x - and z -directions, respectively. The mesh was stretched in the z -direction with $\delta_s = 3$ to obtain a finer resolution near the top where a steep concentration gradient occurs. The general stretching procedure has been given in (4.2). For all variables, periodic boundary conditions were employed in the horizontal direction. For the velocity field free-slip boundary conditions were used at the top and bottom of the computational domain. At the beginning of each simulation all velocity components were set to zero. The full set of 2D equations for the velocity given in (3.15) to (3.22) is solved. It should be noted that to account for the effects of buoyancy in this application case the buoyancy term $\beta(T^*)$ is included into equation (3.22). The term $\beta(T^*)$ is modelled using the Boussinesq approximation and is a function of the non-dimensional temperature T^* as defined in (3.8),

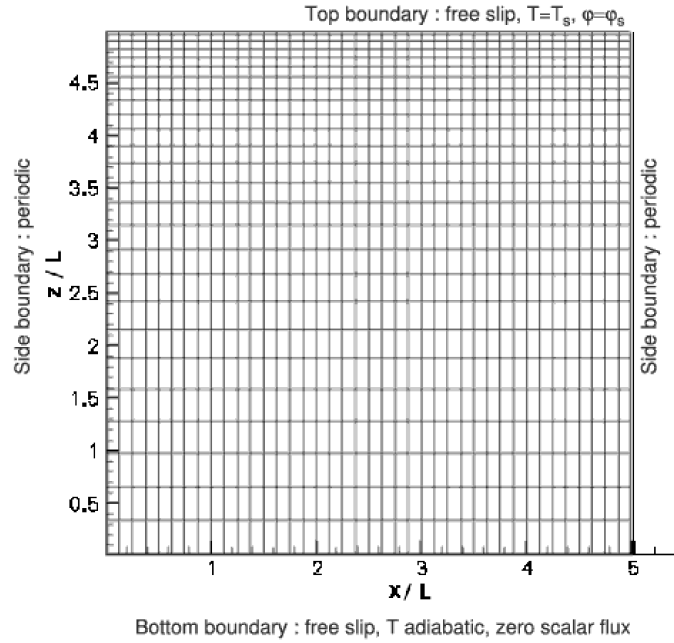


Figure 4.3: Schematic representation of the computational domain. The scatter shows every 10^{th} grid line of the major grid used for the velocity field. The mesh for the scalar was further refined by factors of $R = 2, 3$ and 5 .

where the temperature at the top of the domain was set to a fixed value of $T = T_s = 20^\circ\text{C}$, see (3.50), while in the rest of the computational domain the initial bulk temperature $T_{B,0}$ was 23°C . The relation between density and temperature within this range can be assumed to be linear. To avoid heat losses, at the bottom of the computational domain an adiabatic boundary condition (3.51) was employed for T . The temperature T is a scalar and hence treated the same as the other scalars φ , see (3.36).

At the top of the computational domain the scalar φ was kept at a value of $\varphi = \varphi_s$ (3.50) while at the bottom a zero-flux boundary condition (3.51) was employed. The scalar was non-dimensionalized using (3.7).

The convective instability was triggered by adding random disturbances to the temperature field after letting it evolve for $t = 11$ seconds in order to avoid the triggering of the instability to depend on the mesh size or numerical round off error. The same disturbance

field was used in all simulations. The random numbers that were added to T^* were uniformly distributed between 0 and T_{ran} . To test the influence of the level of the random disturbances on the development of the instability, a test was performed in which a random disturbance field was rescaled so that $T_{ran} = 0.010$, $T_{ran} = 0.020$ and $T_{ran} = 0.040$ before it was added to the non-dimensional temperature. In all three simulations exactly the same buoyant convective disturbance field was found to develop. As can be seen in Table 4.6, the different

T_{ran}	time at which the falling plume reaches $z=4.0$ cm
0.010	23.75 s
0.020	22.30 s
0.040	20.85 s

Table 4.6: *The time difference found between the development of disturbances.*

levels of disturbances were found to affect the time it takes for the plumes to develop. Based on the time difference of 1.45 seconds between subsequent simulations (in which the level of random disturbances is doubled) the exponential growth factor λ for the buoyant-convective instability was estimated to be $\lambda = 0.478$.

To facilitate the comparison between various simulations involving buoyant convection, in the simulations discussed below the same random temperature field consisting of uniformly distributed random numbers between $T = 0$ and $T_{ran} = 0.020$ was added to the non-dimensional temperature field.

4.3.1 Comparison of scalar convection methods in 2D

As mentioned briefly in Section 4.1.2, although the fifth-order upstream central method (C5) shows better accuracy on coarse meshes, it is not the method of choice for the current application due to the absence of a mechanism to deal with steep gradients which could result in the appearance of wiggles. To demonstrate this a number of initial 2D simulations on the 400×256 base mesh using the C5 and the WENO5 schemes were performed. Figure 4.4 shows the profiles extracted at a cross section at $z = 4.5$ cm and $t = 45$ seconds obtained for the C5

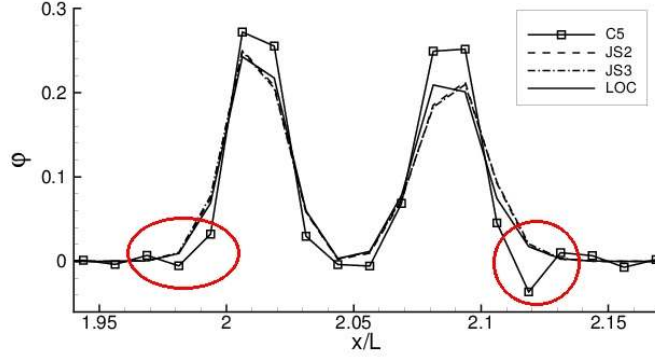


Figure 4.4: Comparison of WENO5 schemes (*JS2*, *JS3*, *LOC*) and the fifth-order central scheme (*C5*), showing profiles of the scalar distribution φ at $z = 4.5\text{cm}$ and $t = 45$ seconds using a Schmidt number of $Sc = 500$.

scheme and different variants of the WENO5 scheme. The cross-section intersects with the falling plumes that develop due to the convective instability which induces sharp gradients in the scalar distribution (see also Figure 4.6a). The plot reveals that wiggles appear close to steep gradients when using the C5 method, which are identified by circles. The original calculation of the weights a_0 , a_1 and a_2 as presented in equation (3.40) is compared to an alternative developed by Shu and Jiang [81], in which the weights for R_i^+ are given by

$$a_0 = \frac{1}{10(\varepsilon + IS_0)^r}, \quad a_1 = \frac{6}{10(\varepsilon + IS_1)^r}, \quad a_2 = \frac{3}{10(\varepsilon + IS_2)^r}, \quad (4.8)$$

while for R_i^- the weights are given by

$$a_0 = \frac{3}{10(\varepsilon + IS_0)^r}, \quad a_1 = \frac{6}{10(\varepsilon + IS_1)^r}, \quad a_2 = \frac{1}{10(\varepsilon + IS_2)^r}, \quad (4.9)$$

with the smoothness indicators IS_i in Shu and Jiang [81] (compare to equation (3.41)) defined by

$$\begin{aligned} IS_0 &= \frac{13}{12}(\varphi_{i-2} - 2\varphi_{i-1} + \varphi_i)^2 + \frac{1}{4}(\varphi_{i-2} - 4\varphi_{i-1} + 3\varphi_i)^2 \\ IS_1 &= \frac{13}{12}(\varphi_{i-1} - 2\varphi_i + \varphi_{i+1})^2 + \frac{1}{4}(\varphi_{i-1} - \varphi_{i+1})^2 \\ IS_2 &= \frac{13}{12}(\varphi_i - 2\varphi_{i+1} + \varphi_{i+2})^2 + \frac{1}{4}(3\varphi_i - 4\varphi_{i+1} + \varphi_{i+2})^2. \end{aligned} \quad (4.10)$$

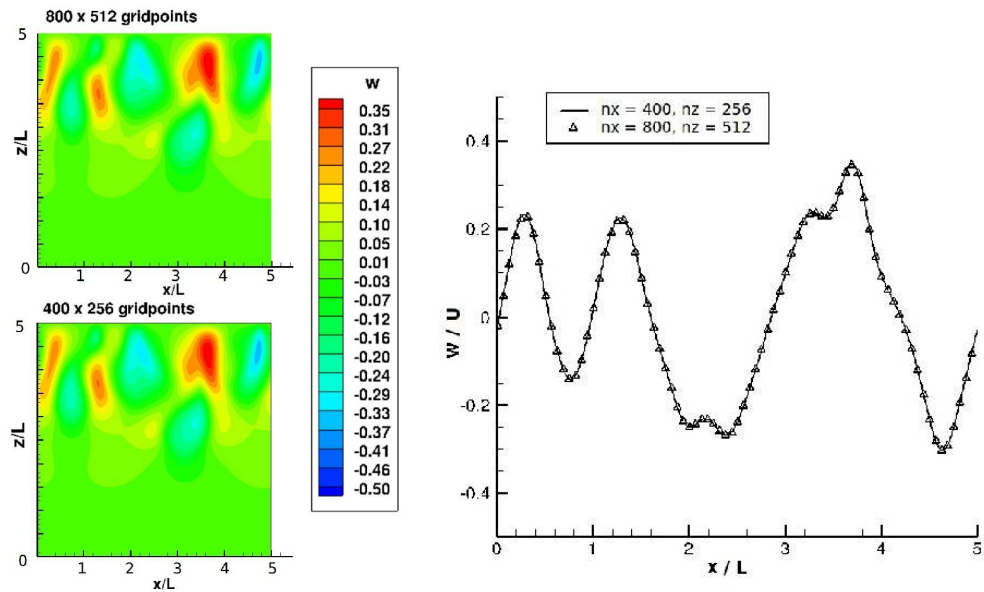
It was found that the wiggles completely disappear when using the WENO5 schemes JS2 and JS3 of Shu and Jiang [81] with powers $r = 2$ and 3 , respectively - see (4.8,4.9) - as well as

the original implementation of Liu et al. [61] (LOC). It can be seen that the results obtained using the WENO5 schemes are very similar.

In the following sections, the mesh sensitivity for resolving the 2D flow and concentration fields were tested in several subgrid mesh refinement studies.

4.3.2 Mesh sensitivity test : Flow-field

To verify that the flow-field was fully resolved on the chosen 400×256 base mesh, the grid was refined in all directions by factors of 1.5 and 2, respectively. Fig. 4.5 shows the contour



(a) vertical velocity w field on a grid (b) vertical velocity w along a line at $z = 4L$ after $t = 400 \times 256$ and 800×512 after $t = 45$ seconds
45 seconds

Figure 4.5: A grid refinement showed that the velocity field is fully resolved on a 400×256 grid.

plots and the velocity profiles obtained from the simulations with the base grid and the mesh refined by a factor 2 ($R = 2$) (with 800×512 points) after $t = 45$ seconds. The contour plots of the flow-field using the refined mesh did not show any visible changes in the flow structures (Fig. 4.5b). This is further confirmed by the vertical velocity profiles along a horizontal line at $z = 4L$. The profiles are virtually identical verifying that the velocity field

is fully resolved on the 400×256 grid which was subsequently used in all further cases.

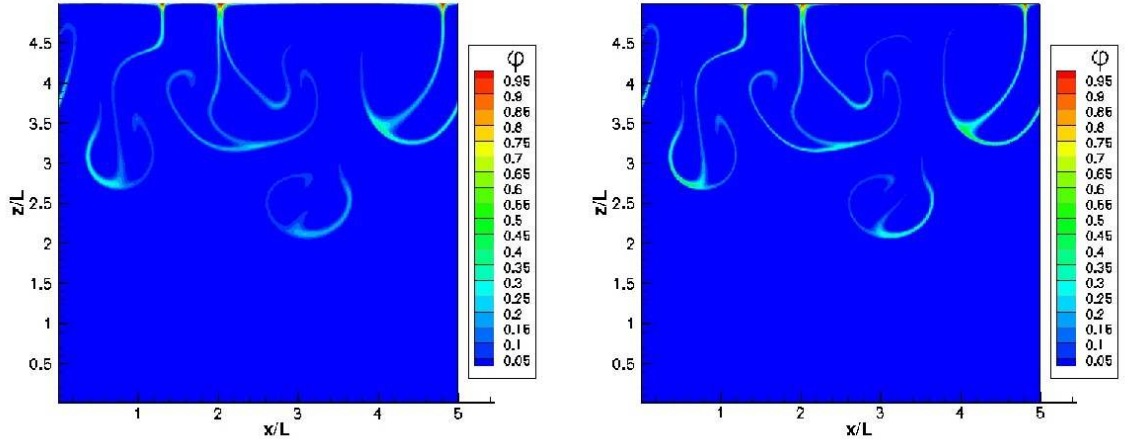
4.3.3 Mesh sensitivity test: gas concentration field

As described above, a dual-mesh approach has been used in which the scalar was resolved on a finer mesh than the one used for the velocity. Various levels of refinement were employed as illustrated in Fig 3.3. In this section, the mesh sensitivity for the scalar transport using this dual mesh approach is evaluated. Fig. 4.6 shows a comparison of the non-dimensional gas concentration contour plots that visualise the development of the scalar transport at $t = 45$ seconds using the base mesh (400×256) for both velocity and scalar and the dual mesh approach with refinement factor 3 applied to the scalar. The Schmidt number is $Sc = 500$ which is equivalent to the diffusion of oxygen in water.

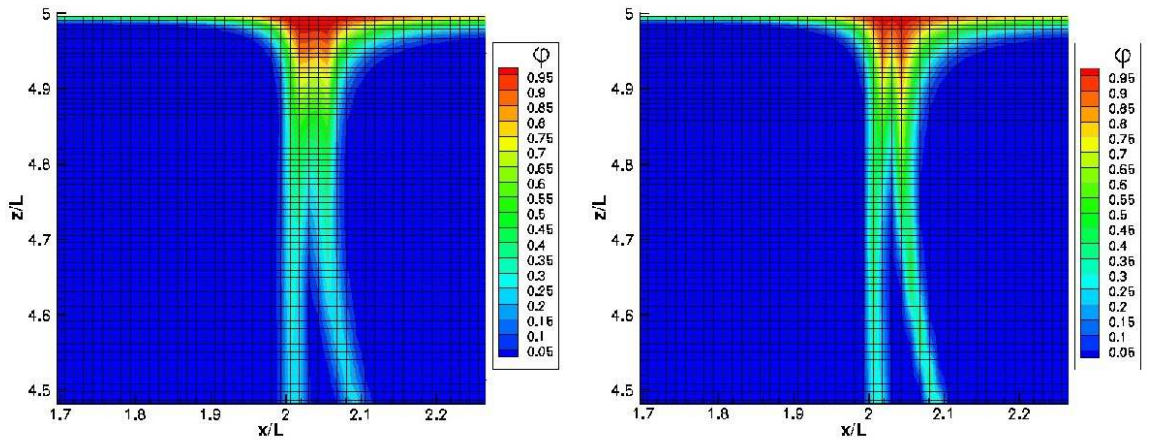
In general, both concentration fields in Figs. 4.6a and 4.6b reveal the same structures of downwards plumes. However, a zoomed view of the top region near the water surface reveals a more detailed representation of the gas concentration field when the dual mesh approach is used (Fig. 4.6c and 4.6d). Please note that the gas concentration in all figures is interpolated to the base grid and not shown on the refined mesh used for the scalar transport.

Figs. 4.7 and 4.8 show line plots of the scalar field at various locations within the domain. The locations are across or along the typical mushroom pattern that develops as a result of the convective instability and shows the presence of sharp gradients in the scalar field. Solving the scalar on the finer subgrid shows a significant improvement in resolution. The $R = 2$ refinement shows a big improvement in deeper regions where the scalar distribution is maintained better than in the base mesh which is relatively coarse. In the far field ($z < 4$) the scalar concentration profiles for the refined cases $R = 2$, $R = 3$ and $R = 5$ converge to nearly identical values (Fig. 4.7a).

The improved resolution becomes even more relevant when the spatially integrated total scalar concentration in the domain over time is considered. Fig. 4.9a shows the total concentration over time for $Sc = 500$. Up to a time of $t = 30$ seconds the gas transfer is dominated by diffusion. Subsequently, the instability induces a convective flow that significantly enhances the mass transfer. The typical mushroom patterns start penetrating the



(a) Domain after $t = 45$ seconds on standard mesh (b) Domain after $t = 45$ seconds with refined submesh
 $R = 3$



(c) Zoomed view after $t = 45$ seconds on standard mesh (d) Zoomed view after $t = 45$ seconds with refined submesh $R = 3$

Figure 4.6: Comparison of the gas concentration field after $t = 45$ seconds on standard mesh $n_x = 400$ and $n_z = 256$ and with a dual subgrid in place three times as fine (see Fig. 3.3c). The gas concentration field is resolved in sharper detail with less smearing.

deeper regions of the domain. It is here where the refined submesh shows a much improved resolution with a continuous increase in the concentration levels whilst the standard mesh shows a drop in concentration levels. The drop occurs when the scalar reaches the region

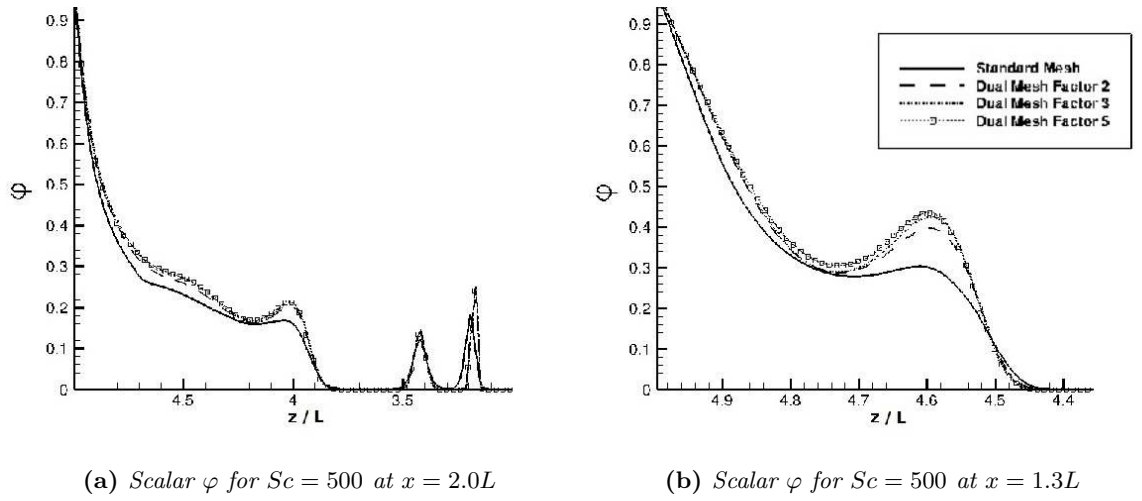
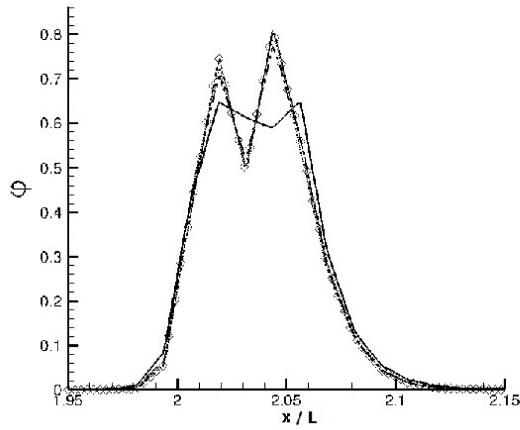
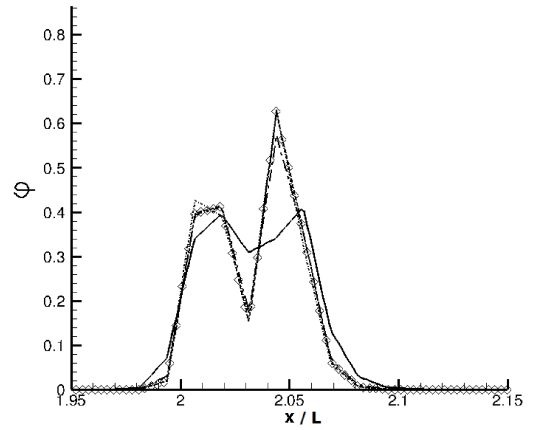


Figure 4.7: Comparison of scalar field after $t = 45$ seconds on different levels of subgrid mesh refinement. The two locations are vertical lines at $x = 2.0L$ and $x = 1.3L$ along the downwards plumes as seen on Fig. 4.6a.

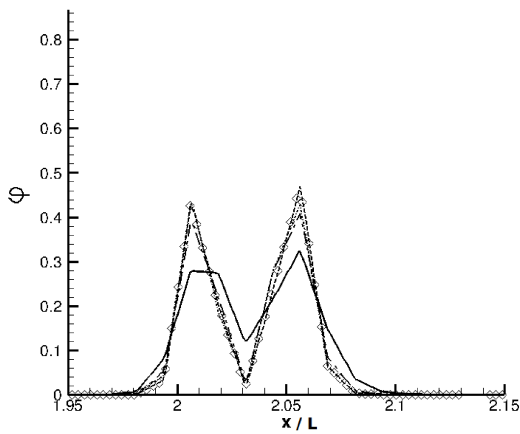
where $z < 2.5L$ (and the mesh becomes significantly coarser) after around $t = 55$ seconds (Fig. 4.9a). This points out an insufficient resolution of the scalar transport in this region. This effect was not present in the refined cases (Fig. 4.9a). The same is found for the transport of the non-dimensionalized temperature T^* (Fig. 4.9b). The grid refinement study for the temperature transport shows a similar trend as seen for the concentration field in Fig. 4.9b. On the coarse mesh fluctuations become evident after $t = 50$ seconds whereas the refined cases do not exhibit such temperature fluctuations. Again the results are identical for all refined cases ($R = 2$, $R = 3$ and $R = 5$).



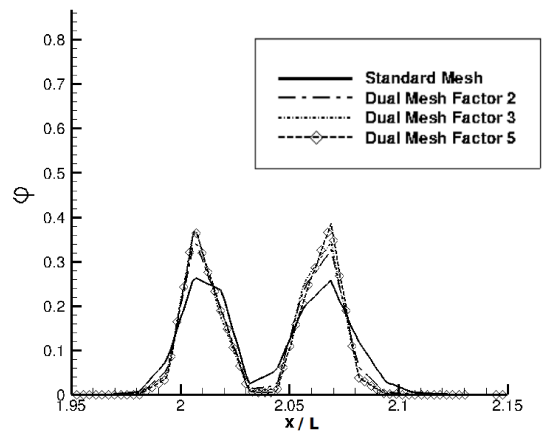
(a) Scalar φ for $Sc = 500$ at $z = 4.9L$



(b) Scalar φ for $Sc = 500$ at $z = 4.8L$

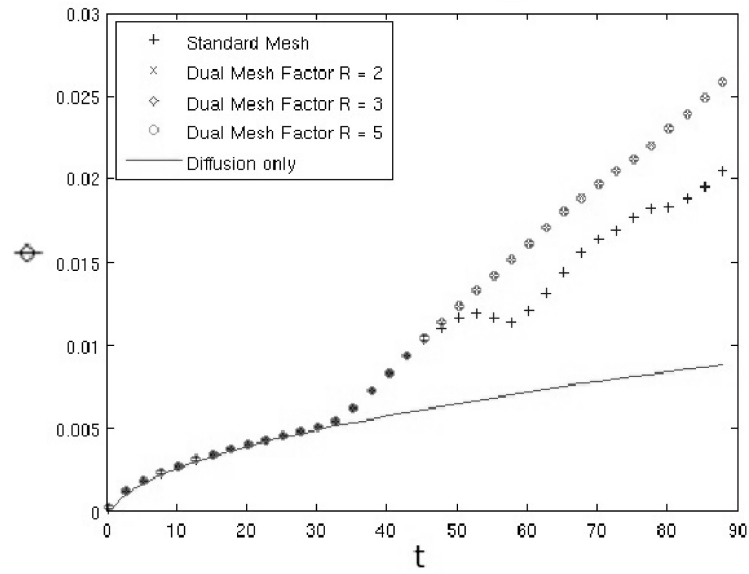


(c) Scalar φ for $Sc = 500$ at $z = 4.7L$

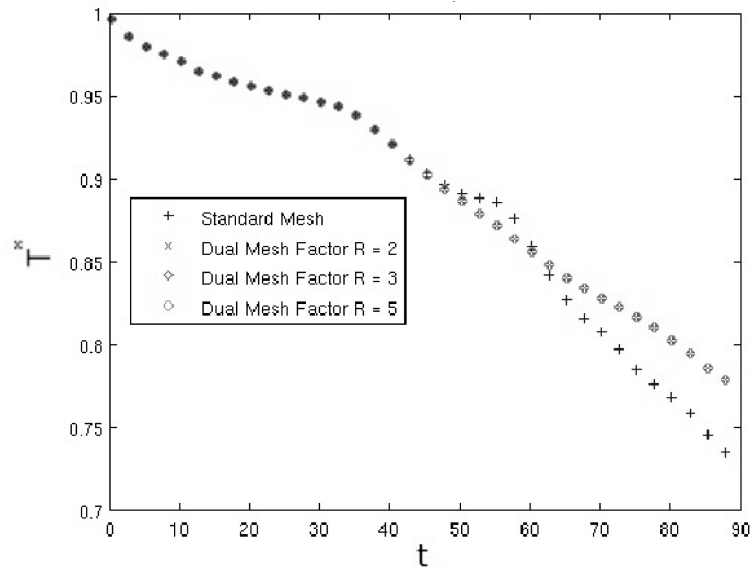


(d) Scalar φ for $Sc = 500$ at $z = 4.6L$

Figure 4.8: Comparison of scalar field after $t = 45$ seconds on different levels of subgrid mesh refinement. The location is a horizontal line at various depths z across the downwards plumes as seen on Fig. 4.6d and 4.6c.



(a) Scalar φ for $Sc = 500$ over time



(b) Non-dimensional total temperature T^* over time

Figure 4.9: Comparison of the total non-dimensional scalar concentration and temperature T^* over time for different levels of subgrid refinement

Chapter 5

Simulations in a 3D domain

THE aim of this study is to gain more understanding of the physical mechanisms that control the absorption of oxygen into water in a convective flow environment. For that purpose it is necessary to resolve the convective and diffusive transport of the dissolved oxygen in a three dimensional domain. The oxygen concentration takes the role of the passive scalar φ in the WENO scheme as described in Section 3.5 which is used to discretize the convection-diffusion equation. The Schmidt number for the absorption of oxygen into water is $Sc \approx 500$ which means the diffusion is very low and steep concentration gradients will occur. The findings of the numerical experiments in Chapter 4 showed that the numerical scheme as described in Chapter 3 is very capable of resolving both convection and diffusion of such high Schmidt number transport problems with negligible errors. The minimum mesh size found in the 2D tests was implemented and a mesh sensitivity study was also carried out for the for the 3D simulations presented in this chapter. The instantaneous gas concentration fields and flow visualisation are presented and an analysis of the statistical data is also carried out together with a qualitative comparison to experiments from the literature.

5.1 Boundary and Initial Conditions

The computational domain is defined as a rectangular box of size $x = y = z = 5L$ as illustrated in figure 5.1. The base mesh size ($R = 1$) is $400 \times 400 \times 256$ gridpoints. The mesh is uniform in the x - and y - directions. An anisotropic stretching is applied in the z - direction with $\delta_s = 3$ as described in (4.2). The figure shows every 10^{th} grid line in the x - and y - directions and every 8^{th} grid line in the z - direction. The thick lines depict the parallel decomposition into 400 subdomains as described in Section 3.8. This is essentially a three dimensional extension of the 2D mesh used in figure 4.3. The boundary conditions in the horizontal directions are periodical whilst a free slip velocity boundary condition is applied on the upper and lower boundary. The temperature at the interface at the top of the domain is set to a fixed value of $T = T_s = 20^\circ\text{C}$, see (3.50), while in the rest of the computational domain the initial bulk temperature is $T_{B,0} = 23^\circ\text{C}$.

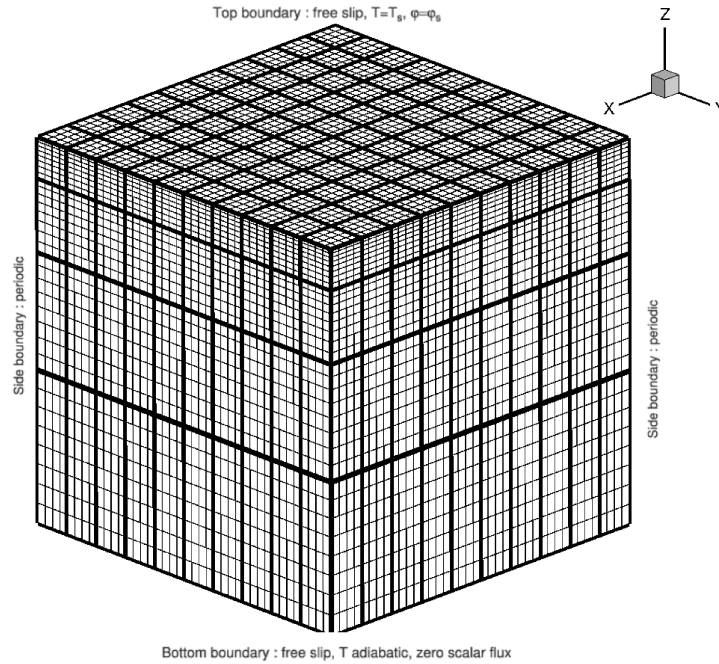


Figure 5.1: *Schematic of the 3D domain*

At the top of the computational domain the scalar ϕ was kept at a value of $\phi = \phi_s$

(3.50) while at the bottom a zero-flux boundary condition (3.51) was employed. In a similar manner as in the 2D simulations in Section 4.3 the convective instability is triggered by adding random disturbances to the temperature field after letting it evolve for $t = 11$ seconds with a $T_{ran} = 0.010$. The same random disturbance field is used in all 3D simulations.

5.2 Results and Discussion

The simulations are carried out by parallel computing where the domain is decomposed into 400 subdomains. In all simulations the Reynolds number used is $Re = 100$ and the Prandtl number is $Pr = 6$. Three simulations are carried out with different levels of dual grid refinement where the gas concentration field is solved on a finer mesh. For the simulations with dual mesh refinement of $R = 1$ (base grid $400 \times 400 \times 256$ points) and $R = 2$ (twice as many gridpoints in each direction), four passive scalars φ_n are solved simultaneously with the four Schmidt numbers $Sc = 20, 50, 200$ and 500 . In the third simulation with a dual grid refinement of $R = 3$ only one passive scalar is solved for $Sc = 500$ in order to save computational resources. The results here are using $Sc = 500$ which is the equivalent Schmidt number for the absorption of oxygen into water. All field variables were exported in a 3D format at every second simulation time and the simulations were run for 60 second physical time.

5.2.1 Qualitative Mesh Sensitivity of 3D Gas Concentration Field

In Chapter 4.3 it could be shown that a mesh refinement of $R = 2$ is sufficient to fully resolve the transport of the scalar field with negligible errors. A further refinement to $R = 3$ and $R = 5$ did not show a higher resolution. The same effect was seen in the 3D simulations. The velocity field is solved on the same base grid for all 3D simulations, as it was demonstrated in section 4.3.2 that the velocity field is fully resolved on the base grid. Figure 5.2 shows a comparison of instantaneous contour plots of the gas concentration between the base grid and refinement $R = 3$. The plots are obtained from a centre plane at $y = 2.5cm$. Red and blue areas correspond to high and low concentration levels, respectively. At the interface

saturation is reached. Figures 5.2a and 5.2b show the onset of the flow and penetration of high concentration plumes after 40 seconds simulation time. The plots in the centre and bottom row show the concentration field at 50 and 60 seconds respectively. The gas concentration field shows a sharper resolution with the refined subgrid, especially for larger time scales. As in the 2D simulations there was no significant improvement between refinement levels $R = 2$ and $R = 3$.

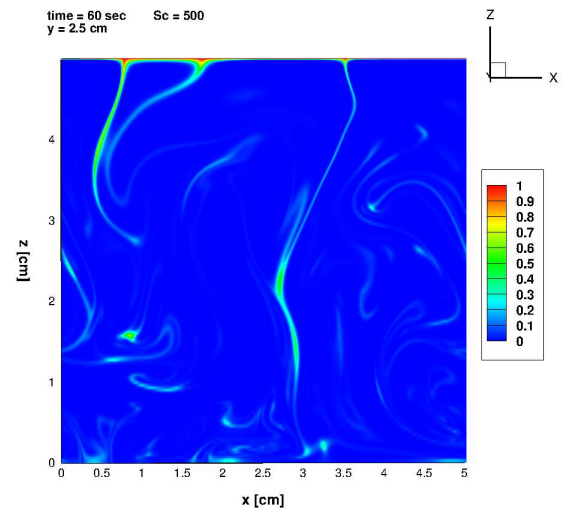
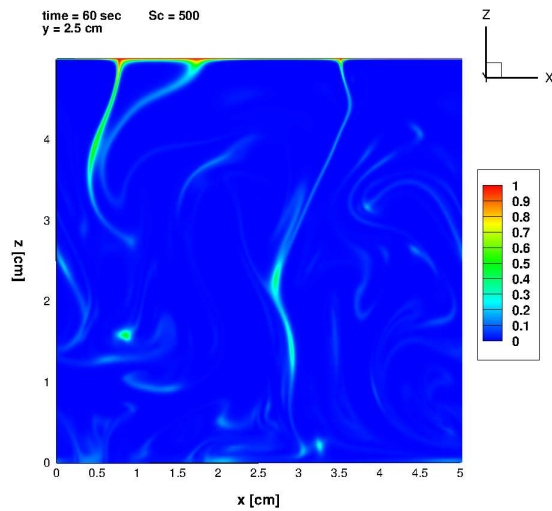
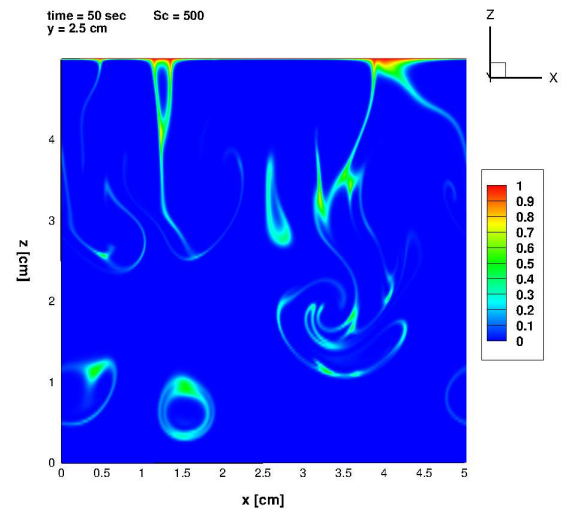
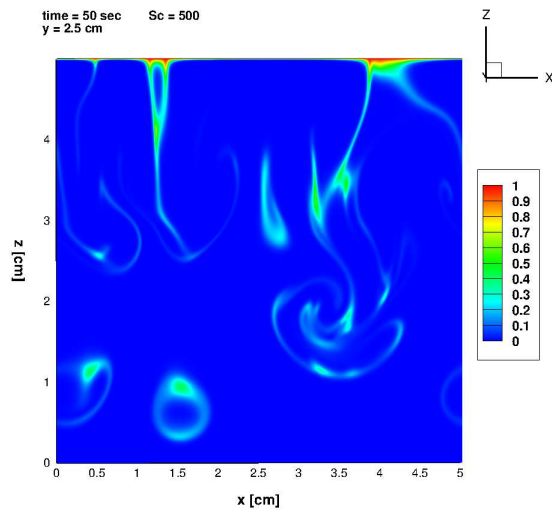
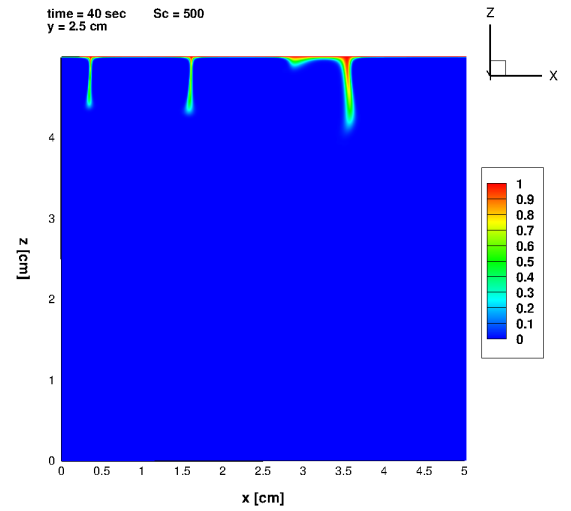
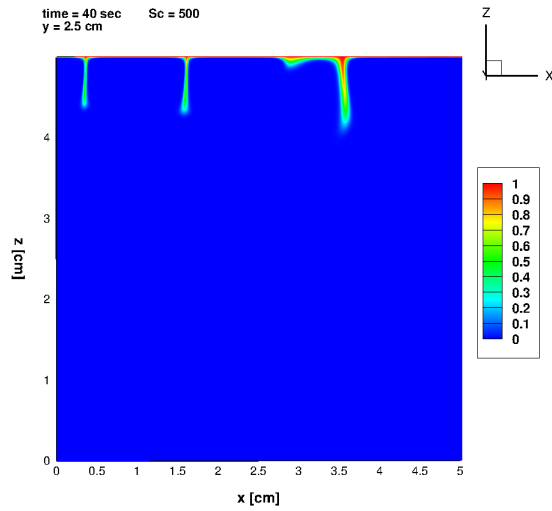
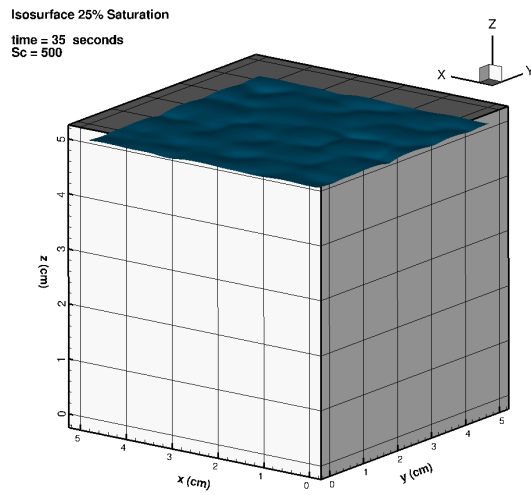


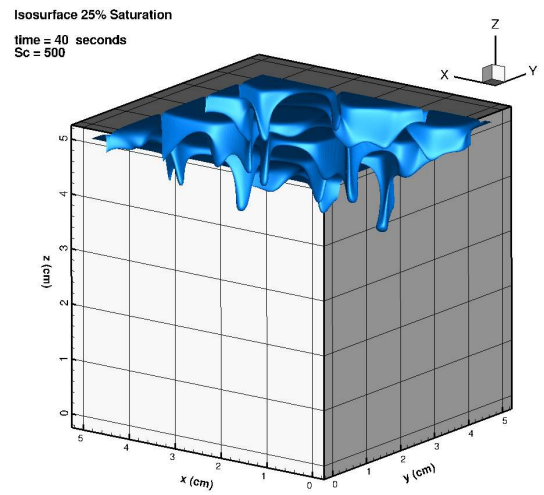
Figure 5.2: Contour plots of gas concentration

5.2.2 3D isosurfaces

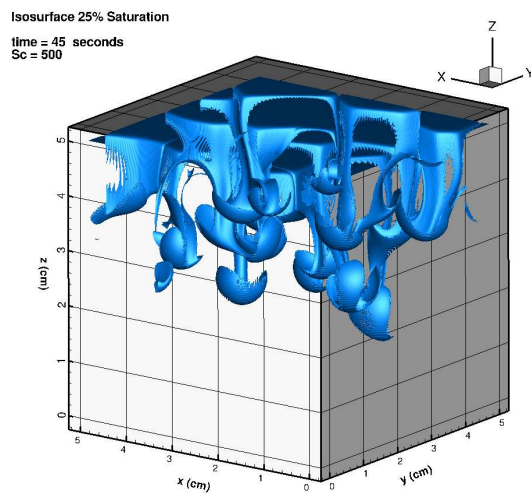
Figure 5.3 and 5.4 show two sequences of 6 isosurfaces of a gas saturation of 25% as viewed from below and above the interface from $t = 35s$ to $t = 60s$ in intervals of 5 seconds for the $R = 3$ and $Sc = 500$ case. The sequence shows that just after the onset of the instability (Figure 5.3a and 5.4a) that cold water of high oxygen concentration is collected in narrow regions that then start plunging down forming sheets of high oxygen concentration water penetrating the unsaturated bulk. Figure 5.5 illustrates the link between the structure of the high gas concentration areas and the temperature field. The plots on the left show the gas concentration isosurfaces whereas the plots on the right show the isosurfaces of the non-dimensional temperature at the early stage of the instability. The downwards moving sheets initially form a reticulated pattern with 'cells' of similar size. This is in good agreement with experimental observations by Spangenberg and Rowland [85] and is discussed further in section 5.3. As time progresses the smaller cells merge and fewer larger cells remain. In Figure 5.3 it is also revealed that as time progresses the penetration changes from an initial sheet-like structure to fine tubes. At $t = 40s$ the penetration is only present in thin straight sheets. At $t = 45s$ a mushroom like structure develops similar to what was seen in the 2D simulations. The outwards bulging regions subsequently become separated and curl upwards whilst thin tubes progress and penetrate deeper. These thin tubes become dominant and the initial sheet-like penetration develops into fine tubes of high gas concentration. The detached high concentration areas swirl around but do not disperse very much. Areas of high concentration remain in close proximity to areas with almost zero concentration. This is a result of the low diffusivity of the gas at $Sc = 500$. On the contrary, as can be seen in Figure 5.5, the temperature field is much more diffusive and such fine structures are lost. The thermoclines are much thicker and wider compared to the isosurfaces of concentration field. (see also Section 5.2.3)



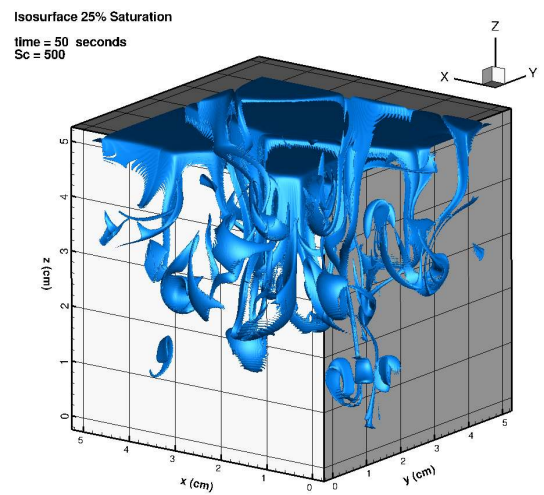
(a) $time = 35s$



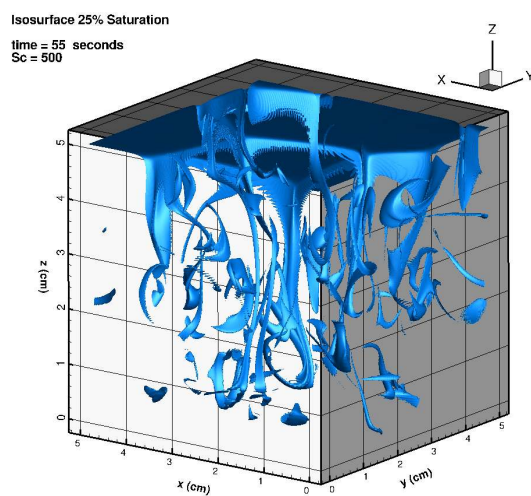
(b) $time = 40s$



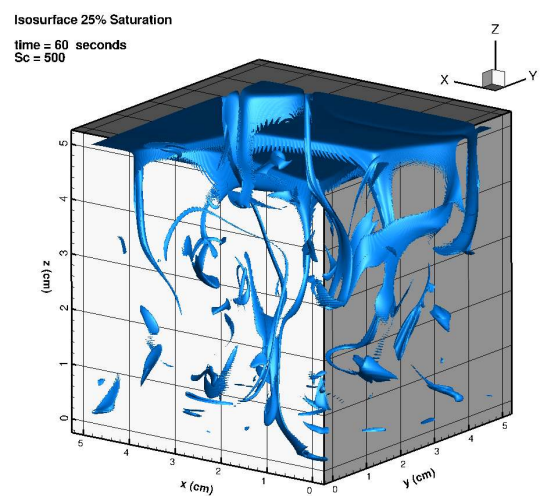
(c) $time = 45s$



(d) $time = 50s$

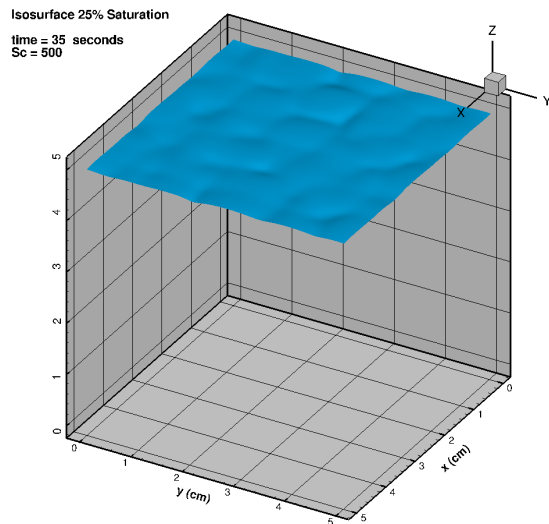


(e) $time = 55s$

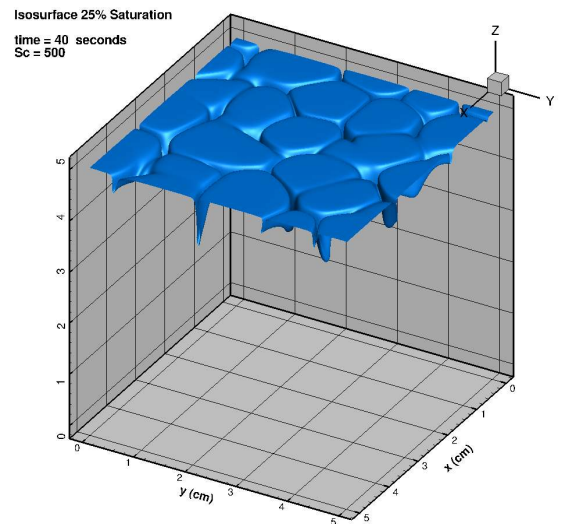


(f) $time = 60s$

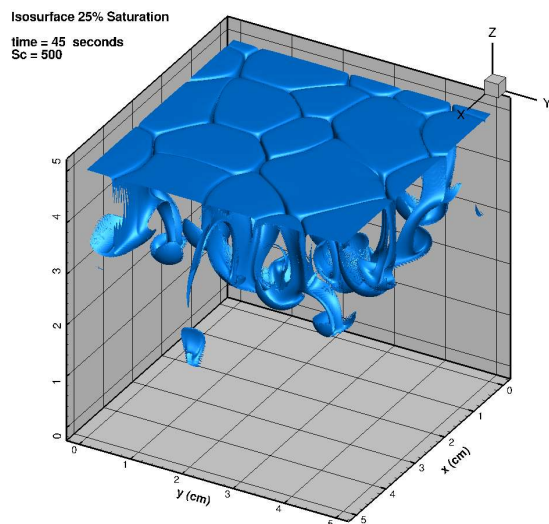
Figure 5.3: Sequence of isosurfaces of 25% gas concentration viewed from below



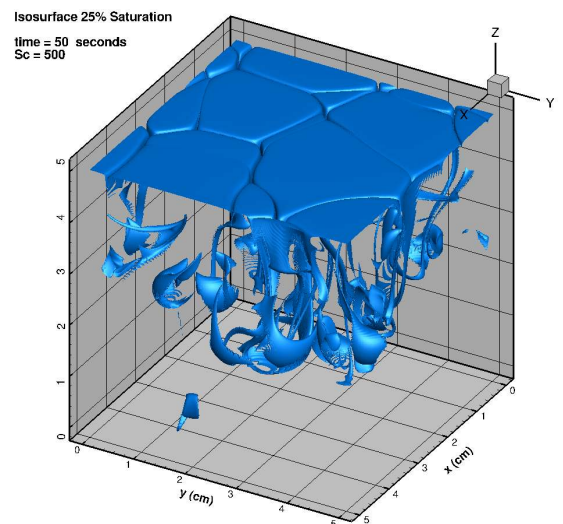
(a) $time = 35s$



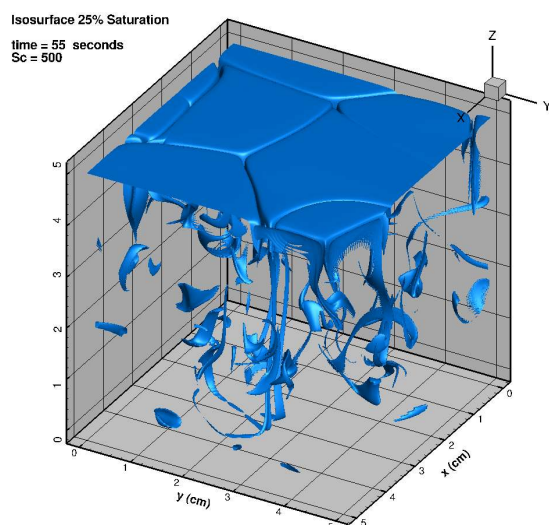
(b) $time = 40s$



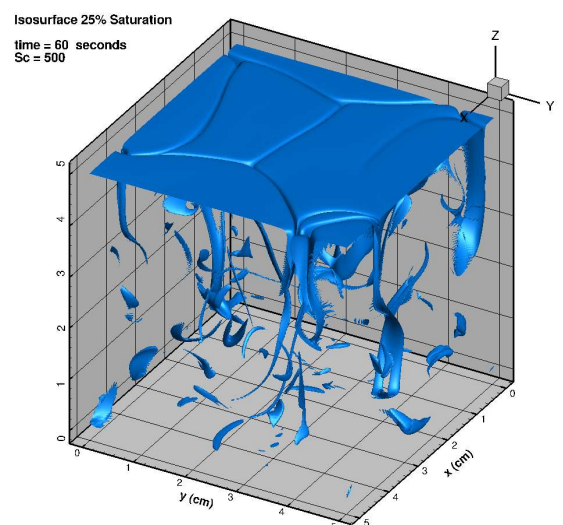
(c) $time = 45s$



(d) $time = 50s$



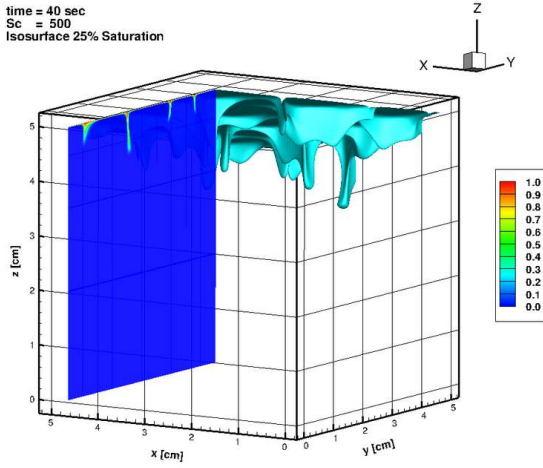
(e) $time = 55s$



(f) $time = 60s$

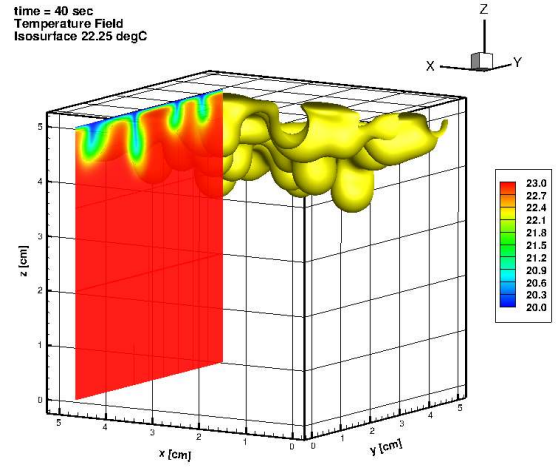
Figure 5.4: Sequence of isosurfaces of 25% gas concentration viewed from above

time = 40 sec
Sc = 500
Isosurface 25% Saturation



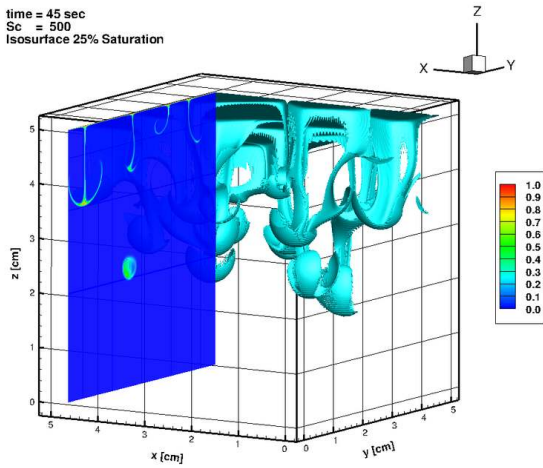
(a) time = 40s

time = 40 sec
Temperature Field
Isosurface 22.25 degC



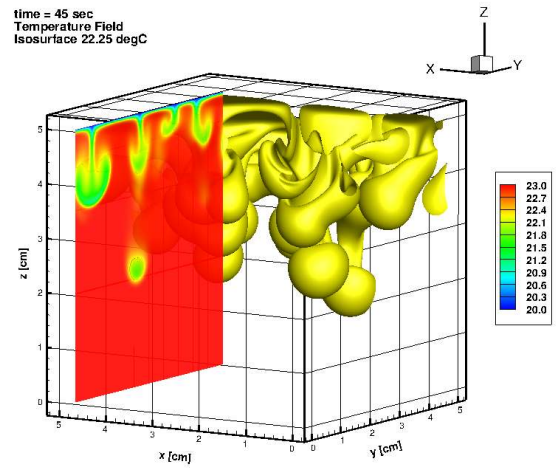
(b) time = 40s

time = 45 sec
Sc = 500
Isosurface 25% Saturation



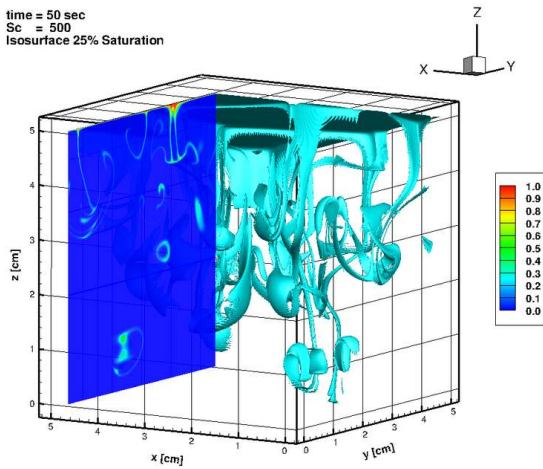
(c) time = 45s

time = 45 sec
Temperature Field
Isosurface 22.25 degC



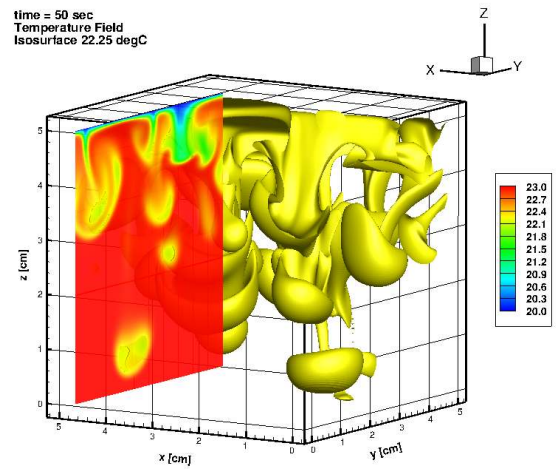
(d) time = 45s

time = 50 sec
Sc = 500
Isosurface 25% Saturation



(e) time = 50s

time = 50 sec
Temperature Field
Isosurface 22.25 degC



(f) time = 50s

Figure 5.5: Comparison of isosurfaces of 25% gas concentration (left) and temperature (right)

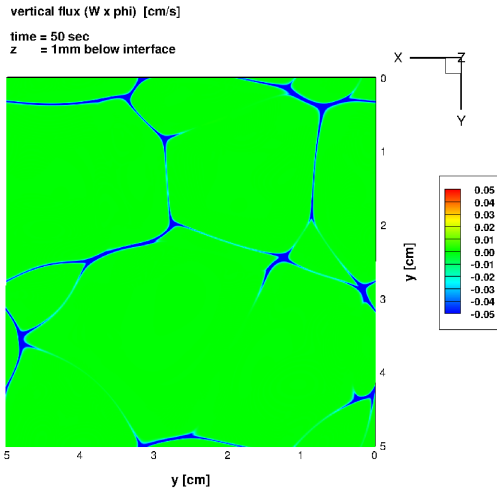
5.2.3 Temperature and Convective Vertical Gas Flux Relation

As stated in the previous section (5.2.2) the temperature reveals some information about the gas concentration, especially near to the interface. This section investigates the relation between the temperature and the *instantaneous vertical convective gas flux* ξ , which is defined as

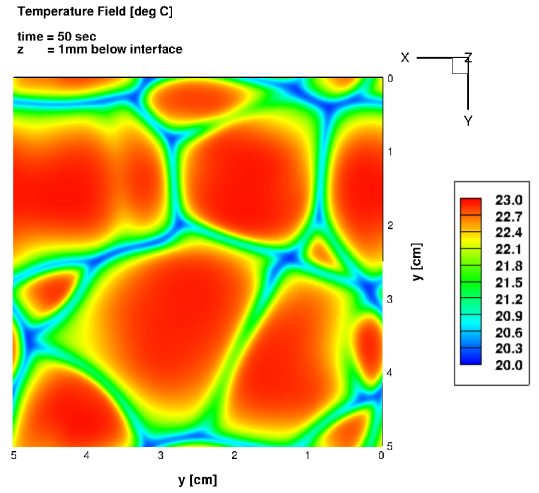
$$\xi = w\varphi^* \quad (5.1)$$

where w is the vertical velocity component and φ^* is the non-dimensional gas concentration. The temperature causes density differences that drive the flow. Initially cold water sinks down in sheet like patterns dragging high gas concentration fluid with it. This plunging motion causes also curl upwards and around 10 seconds after the instability began a mushroom like structure can be observed in the 25% gas concentration isosurfaces (see Figure 5.3). High gas concentration fluid curls outwards and upwards and some areas become detached from the downwards moving fluid. The upwards momentum can overcome the effects of buoyancy and there is also fluid moving upwards that is colder than the surrounding fluid. As the downward moving fluid displaces warmer fluid in the bulk an equal amount of warmer fluid will be moving upward. Figure 5.6 shows a comparison of the vertical flux ξ and the fluid temperature for horizontal sections through the domain 1mm, 10mm and 30mm below the interface at 50 seconds simulation time. Near the interface there is a good correlation between temperature and vertical flux however this correlation is almost lost when moving further below the interface. The temperature has such high diffusivity that some detached high gas concentration lumps might have almost the same temperature as the surrounding fluid. As the concentration isosurfaces revealed, the high concentration fluid stays in thin confined areas that swirl around. The temperature in these areas will increase over time much faster than the gas concentration diffuses. In the top left and bottom of Figure 5.6c there are red areas of upwards swirling high concentration fluid. In the equivalent temperature plot (Figure 5.6d) these areas are relatively warm and not marked by cold fluid. The temperature has diffused and the fluid has already warmed up. Cold fluid marks areas of downwards flux better but is already very blurry 10mm below the interface. The temperature is even further

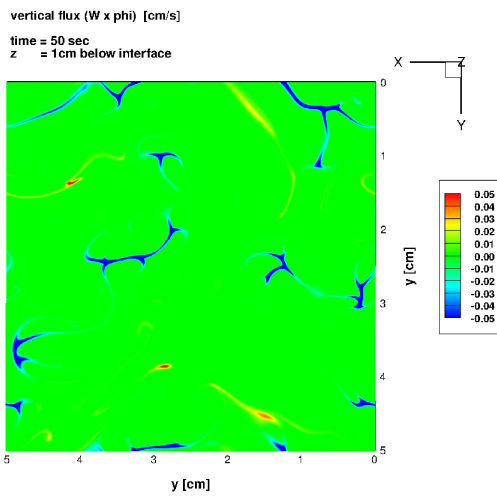
diffused 30mm below the interface (Figure 5.6e). This observation corroborates the practice of using the temperature at the interface as an indicator of the mass flux (e.g.[36]).



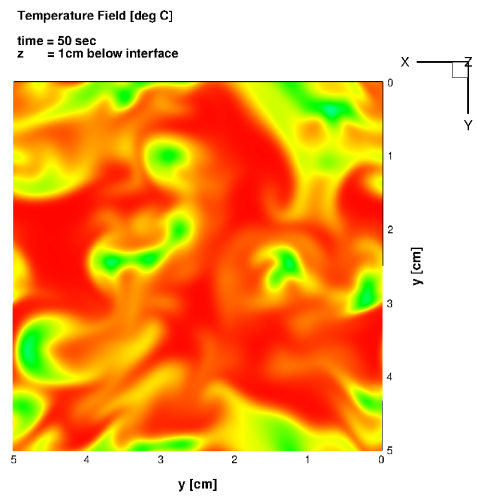
(a) vertical flux 1 mm below interface



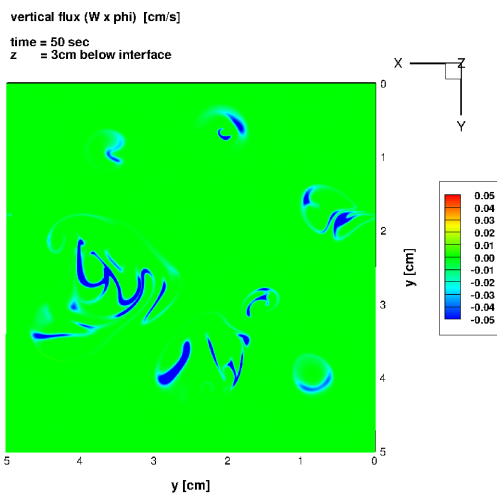
(b) temperature 1 mm below interface



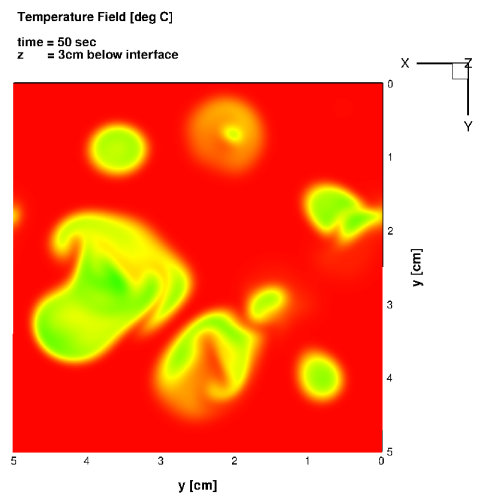
(c) vertical flux 10 mm below interface



(d) temperature 10 mm below interface



(e) vertical flux 30 mm below interface



(f) temperature 30 mm below interface

Figure 5.6: Comparison of vertical flux and temperature at horizontal planes after 50 seconds

5.2.4 Transfer Velocity K_L

As stated in Section 2.2.1 the mass transfer is a combination of molecular diffusion and turbulent transport as described by (2.2) which states that the mass flux is the sum of diffusive flux and advective flux. When horizontally averaging all variables the mass flux in the vertical direction is hence composed of

$$J = -\left(D\frac{\partial\bar{\varphi}}{\partial z} - \bar{\varphi w}\right) \quad (5.2)$$

where D is the mass diffusion coefficient and the overbar denotes horizontal averaging. The first term on the right describes the molecular diffusion. The diffusive flux is proportional to the vertical concentration gradient. The second term is the advective proportion of the mass flux. It describes the mass transport in vertical direction due to the fluid motion. Both terms can be precisely evaluated from the numerical simulations. The concentration φ and the vertical velocity w are known in the domain. When horizontally averaged the vertical mass flux \bar{J} can be determined.

At the interface there is no vertical velocity component w hence the advective component vanishes and the mass flux is entirely driven by diffusion. The total mass flux J into the system becomes $J = -D\frac{\partial\bar{\varphi}}{\partial z}$ and can hence be evaluated as the concentration gradient at the interface is known in the simulations. This enables the calculation of the transfer velocity K_L

$$K_L = \frac{J}{\Delta\varphi} = \frac{J}{\varphi_i - \varphi_b}. \quad (5.3)$$

The term J can be determined from (5.2) and $\varphi_i = 1$ is the interface concentration and φ_b is the average bulk concentration. Figure 5.7 shows the transfer velocity K_L over time from the $R = 2$ simulations.

In that simulation four scalar concentrations with the Schmidt numbers $Sc = 20, 50, 200$ and 500 were resolved simultaneously. It can be clearly seen that there is a sharp increase in K_L at around 40 seconds time when the convection sets in. Before that point in time there is only diffusive mass transfer because the fluid is stationary. The dashed lines show

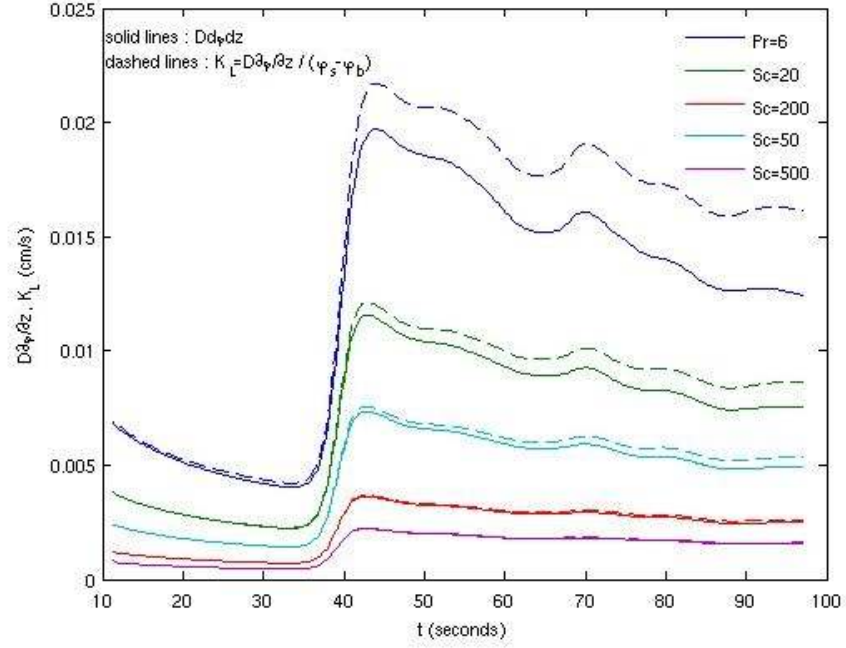


Figure 5.7: K_L over time

the transfer velocity K_L as defined in (5.3). For comparison the solid lines show the transfer velocity when the bulk concentration is assumed to be $\varphi_b = 0$ for the entire process. For high Schmidt numbers this assumption is acceptable as the entire bulk concentration remains very low throughout the process. If the water body is relatively large for high Schmidt numbers K_L can be estimated from the concentration gradient at the interface alone.

In theory K_L for various Schmidt numbers scales with $\alpha_{Sc}^{-0.5}$ where α_{Sc} is the ratio of the Schmidt numbers which are compared. Figure 5.8 shows K_L at $t = 90s$ from figure 5.7 on double logarithmic axes. The triangles are the 'true' K_L where the change in bulk concentration φ_b is considered, the squares mark values where $\varphi_b = 0$. Similar to the plot in figure 5.7 it becomes evident that for high Schmidt numbers the bulk concentration φ_b has nearly negligible impact on the transfer velocity K_L . The denominator in (5.3) stays very close to unity so that $K_L \approx -D \frac{\partial \varphi}{\partial z}$ at the interface. The dotted line in figure 5.8 represents the scaling with $\alpha_{Sc}^{-0.5}$ and the dashed line is the average power for the triangles. The average scaling exponent was determined as -0.522. Figure 5.9 shows the horizontally

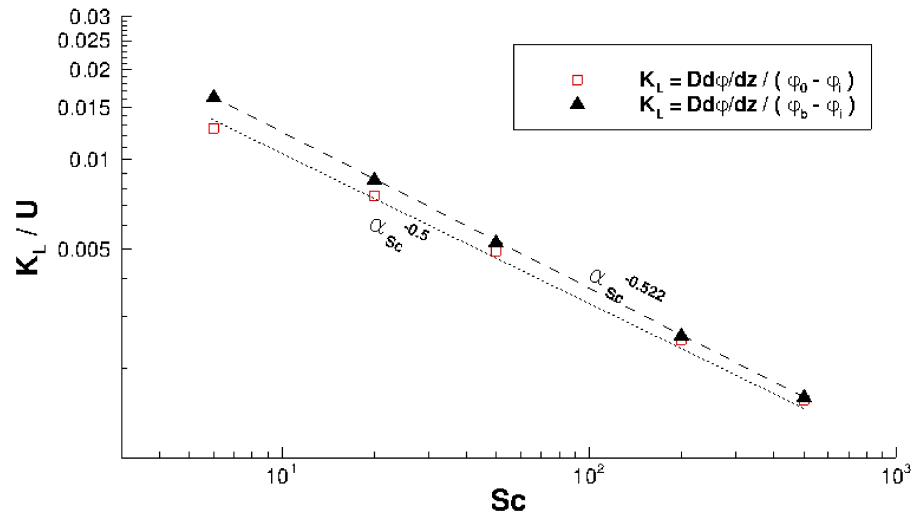


Figure 5.8: Schmidt number scaling for K_L at $t = 90s$

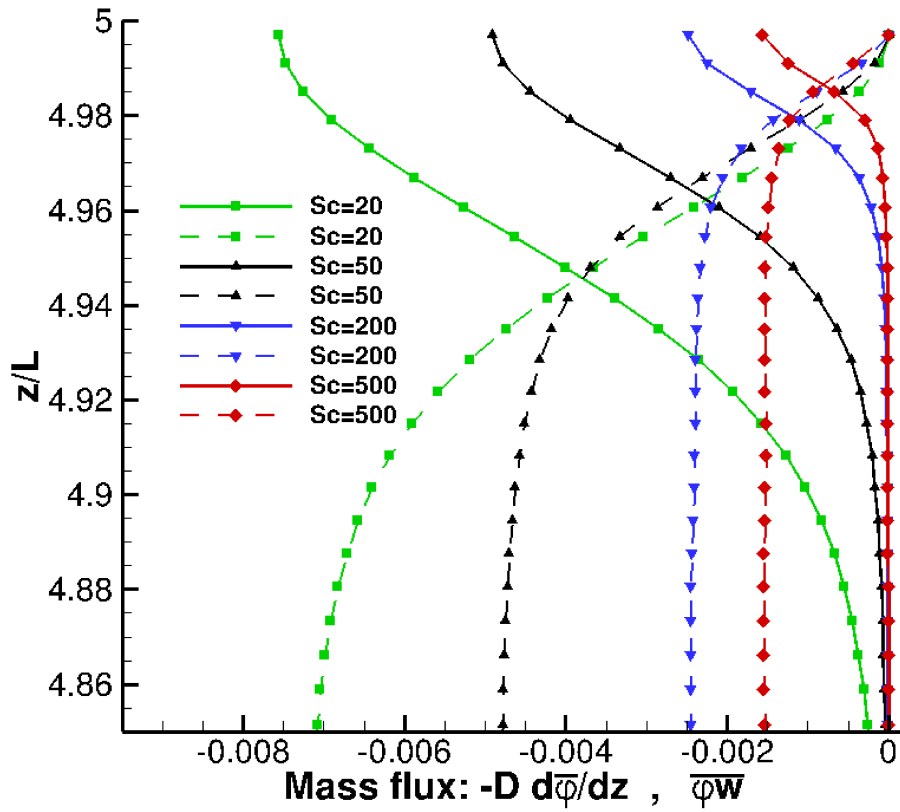


Figure 5.9: Vertical Convective and Diffusive Mass Fluxes at $t = 90s$ below the interface

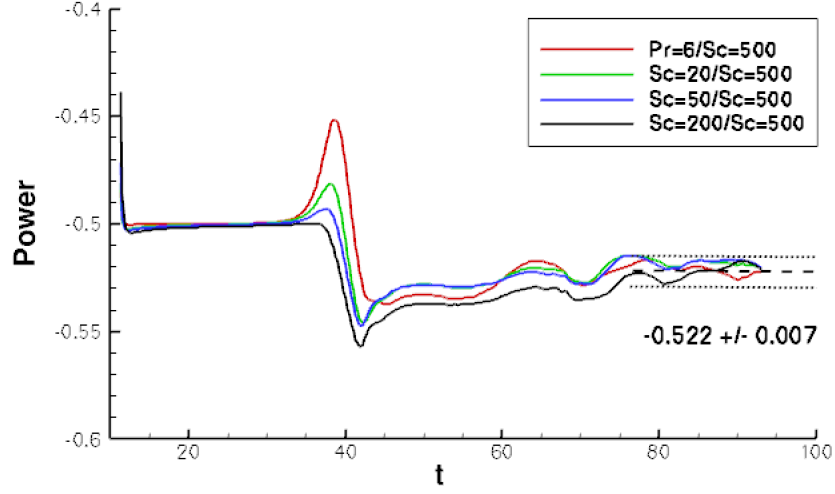


Figure 5.10: Power scaling for K_L over time

averaged convective and diffusive vertical mass fluxes near the interface. The diffusive mass flux is determined from the term $-D\frac{\partial\varphi}{\partial z}$ and the convective mass flux from the term $\overline{\varphi w}$ in (5.2). The solid lines in figure 5.9 represent the diffusive flux and the dotted lines represent the convective flux. It can clearly be seen that the convective flux near the interface ($z = 5$) is zero. At the interface there is only diffusive flux. Further away from the interface the diffusive flux in vertical direction diminishes and the process is dominated by the convective fluxes (dotted lines). This plot is taken at $t = 90s$ and hence corresponds with figure 5.8. The diffusive fluxes at $z = 5$ hence correspond to the squares in figure 5.8.

Figure 5.10 shows the power p of α_{Sc}^p over time for four Schmidt number ratios with $Sc = 500$ as reference. It can be clearly seen that K_L scales almost precisely with $\alpha_{Sc}^{-0.5}$ for the initial phase when there is only diffusion and no fluid motion. The power reduces after the fluid motion sets in. After $t \approx 60s$ recirculation sets in and there are higher variations in the process which narrow down after $t \approx 75s$. The process is then in a quasi-steady state and relatively stable. The variations are very similar except for $\alpha_{Sc} = \frac{Pr=6}{Sc=500}$. This is probably likely due to the strong temperature diffusion. There is nearly two orders of magnitude difference between $Pr = 6$ and $Sc = 500$ and the heat flux is likely to be more influenced by hydrodynamic effects, i.e. the temperature field is distributed more differently than the

oxygen field. The mid range Schmidt numbers $Sc = 20$ and $Sc = 50$ show very similar power scaling. The average power for $t = 90s$ is also plotted and shows that the band covers the scaling power for the 15 seconds well.

5.2.5 Renewal rates and transfer Velocity (K_L)

In section 2.3 conceptual models are reviewed where the transfer velocity K_L is as a function of the diffusion coefficient D and the renewal rate r . This renewal rate can be regarded as the average frequency with which a 'surface renewal event' happens. That is when unsaturated 'fresh' liquid penetrates the concentration boundary layer and replaces saturated fluid. The renewal rate r is therefore also an indication for the strength of the turbulence. Most conceptual models were developed with the idea that the motion of the liquid is generated by shear in the bulk region, however the flow driving mechanism can be various. In nature the flow is driven by a combination of convection and shear. The question is which mechanism is dominant. As the transfer velocity K_L and the diffusion coefficient D are known the renewal rate r can be determined using a conceptual model to evaluate the likelihood of surface renewal events.

The concept of the renewal rate was introduced by Dankwerts [21] and his Surface Renewal model where the relation between K_L and r was found to be

$$K_L \approx \sqrt{Dr} \quad (5.4)$$

where, $D = \frac{1}{ReSc}$. Figure 5.11 shows r over time as derived from (5.4). The renewal rates are obviously a function of K_L and one can clearly see the relation when comparing the plot to figure 5.7.

For instance, Herlina [38] has found renewal rates of between $r = 0.022\frac{1}{s}$ and $r = 0.35\frac{1}{s}$ in her experiments in a grid stirred tank which are similar to what was found in this study. This shows that the gas transfer by buoyant convection is a very efficient method. Even with a lower Reynolds number similar surface renewal is achieved than when using grid stirring. The direct removal of saturated liquid from the surface by the thermoclines causes exchange of saturated and non-saturated fluid near the interface, which is commonly known

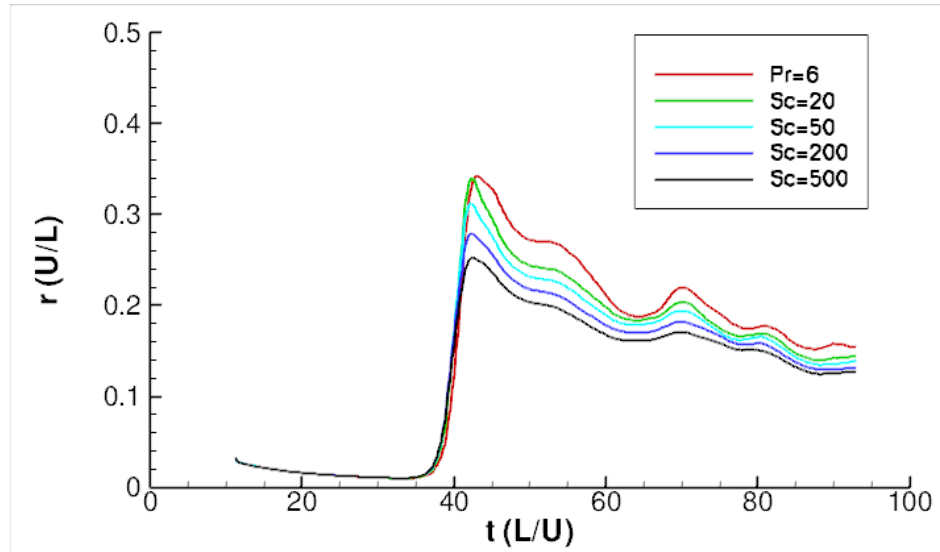


Figure 5.11: Surface renewal rates r over time

as a surface renewal event.

5.2.6 Total Gas Concentration

If there were no motion in the fluid there would only be gas transfer by means of diffusion. A boundary layer would form with the interface being fully saturated. The vertical concentration profile can be determined analytically by

$$\varphi^*(z, t) = 1 - \operatorname{erf}\left(\frac{z}{\sqrt{4Dt}}\right). \quad (5.5)$$

where the diffusion coefficient $D = \frac{1}{ReSc}$. The curve for the *diffusion only* in figure 5.12 is the volume integral of the analytical profile over time. This line represents the theoretical development of the total non-dimensional gas concentration over time if there is only diffusion and no fluid motion. Overlaid are the results from the numerical simulations from 30 seconds simulation time onwards. Initially there is only diffusion acting. The upwards kink at around 40 seconds marks the onset of the flow and the total concentration increases at higher rate.

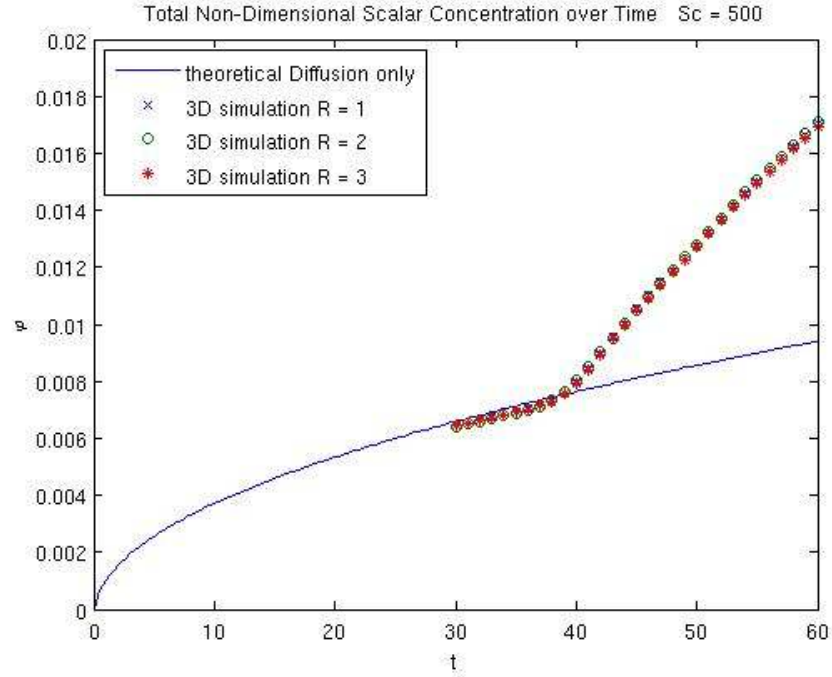


Figure 5.12: *Volume integral of φ over time*

5.2.7 Heat Transfer

As the water surface is cooled there is also heat extracted from the fluid. In reality there is also mass transferred by means of evaporation. With the bulk fluid initially at 23°C and the interface at 20°C the effects of mass loss due to evaporation are very small and can safely be neglected. Fourier's law describes the principle definition of the heat flux per unit area as,

$$\vec{q} = -k\nabla T \quad (5.6)$$

where k is the material's thermal conductivity and ∇T the temperature gradient. The total heat flux \dot{q} over the surface S is the surface integral of ∇T multiplied with $-k$, and reads

$$\dot{q} = \frac{\partial Q}{\partial t} = -k \int_S \nabla T dA. \quad (5.7)$$

Over the discretized horizontal interface surface the total heat flux in (5.7) can be written

as the sum of all local heat fluxes across the cell faces over the interface, such as,

$$\dot{q} = \sum_{i=1}^n -kA_n \frac{\Delta T}{\Delta z} \quad (5.8)$$

where A_n is the face area of each cell face at the interface and the term $\frac{\Delta T}{\Delta z}$ is the local temperature gradient at the interface cell face which is determined by a first order forward difference scheme. Fourier's law describes the heat flux perpendicular to an area by means of conduction, without energy being transported by advection through that area. It is important to note that this is valid for the case of the heat transfer into a liquid as there is no vertical velocity component at the interface.

There is a relation between transfer velocity K_L and the thermal heat flux. The stronger the thermal convection, the higher is the mass and thermal flux due to more mixing and surface renewal. Figure 5.13 shows the relation of thermal flux \dot{q} and transfer velocity K_L during the $R = 2$ simulation. The output rate is in intervals of $t = 0.25s$. The thermal flux at the surface ranges between $\approx 130 \frac{W}{m^2}$ and $\approx 195 \frac{W}{m^2}$. It can be seen that there is a strong correlation between K_L and the heat flux as the points do not scatter much and fall nearly on a line. Figure 5.14 shows the same correlation but all K_L rescaled to $Sc = 500$ with the power law $K_L (\frac{Sc}{500})^{0.522}$ as determined earlier in figure 5.8. It confirms that the transfer velocities scale very well over the entire duration of the process.

5.2.8 Convective cell pattern merging

After the onset of the convective flow a typical convective 'cell pattern' can be observed (see figure 5.4). The cold liquid sinks down in thin sheets. At the early stage the pattern shows the well known typical polygon structure of free surface convection. Even though the initial pattern is relatively homogeneous and the cells have very similar size this pattern is not stable and the downwards moving sheets move around. The cells change in size and shape and some cells even disappear completely and merge with larger growing adjacent cells. In this section the flow field near the interface is analysed qualitatively. In figure 5.15 a sequence of the velocity magnitude contour plots at the interface is shown. Figures 5.16

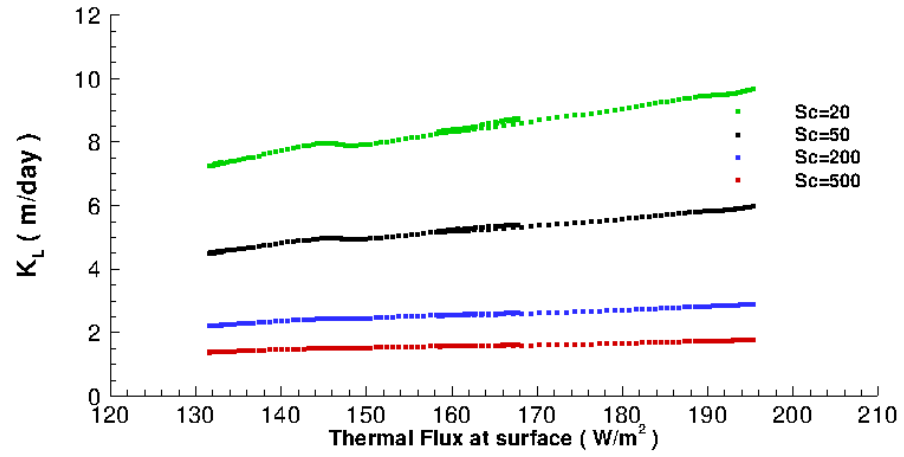


Figure 5.13: K_L versus Thermal Heat flux \dot{q}

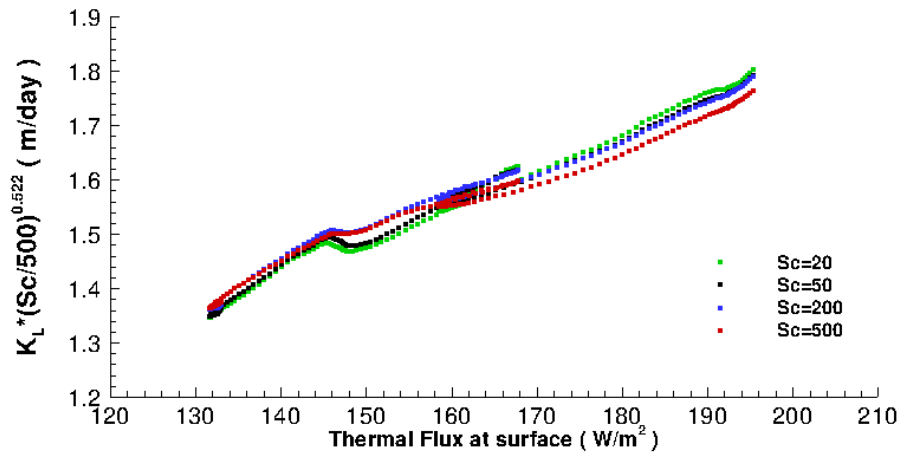


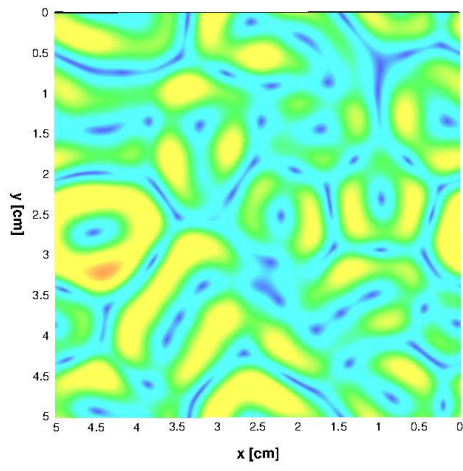
Figure 5.14: K_L versus Thermal Heat flux \dot{q}

and 5.17 show the velocity vectors at the interface and the temperature field 1mm below the interface, respectively. At the initial stage a fairly regular pattern of convective cells form where thin sheets of cold fluid start penetrating the deeper areas. This causes warm unsaturated fluid from the bulk to rise in the centre of the cells which is known as surface renewal. The warm bulk fluid then diverges outwards when approaching the interface. This is illustrated by the vector plots (fig. 5.16). The cell patterns however do shift and cells merge. The temperature near the interface reveals a trend that downwards falling sheets that are warmer at the initial stage have more tendency to disappear. The positions A , B and C in figure 5.17a mark an area of downwards sinking sheets of fluid that is relatively warm compared with other clearly colder sheets. The area at A for instance consists of 3 convective cells at $t = 40s$. Subsequently they merge and become one large convective cell. A similar mechanism can be seen at location B and C .

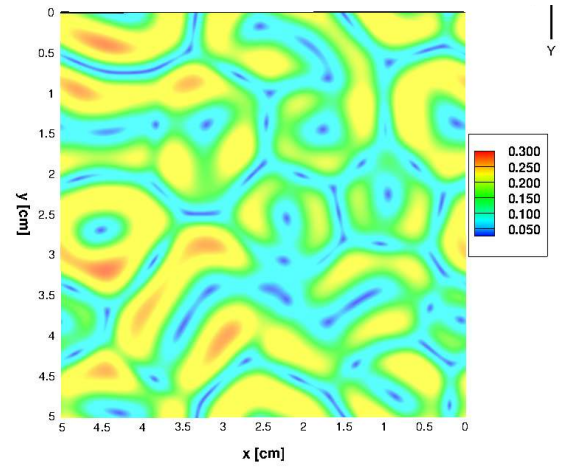
Another factor that determines the 'strength' of a convective cell is its size relative to its neighbours. At location D and E in figure 5.17a a cell is identified that is clearly defined by very cold downwards falling sheets. The surrounding cells are of similar size but not so clearly defined and exhibit warmer cell boundaries and do merge with their neighbouring cells as seen at locations A , B and C . In this process cells D and E becomes surrounded by larger cells, which draw warm liquid up from the bottom in their centres. The cell D subsequently reduces in size and diminishes completely. When looking at the time sequence of the velocity plots and vectors (fig. 5.15 and 5.16) at the location of cell D one can see that the velocity becomes low in that area. Cell D is not 'fed' with liquid from below. The liquid in the centre is drawn away by the down falling sheets of the neighbouring cells that 'eat' up the cell.

These two principal trends revealed from these observations can be summarized as:

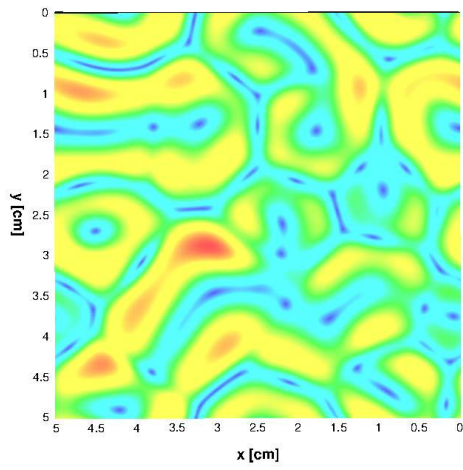
- Cells sharing warmer cell boundaries are more likely to merge
- Small cells surrounded by larger cells are more likely to diminish.



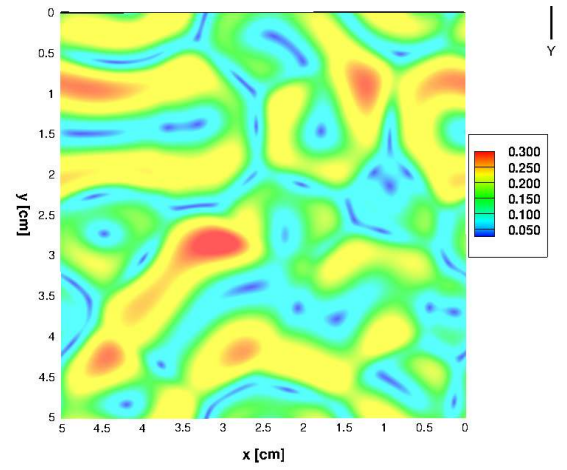
(a) $time = 40s$



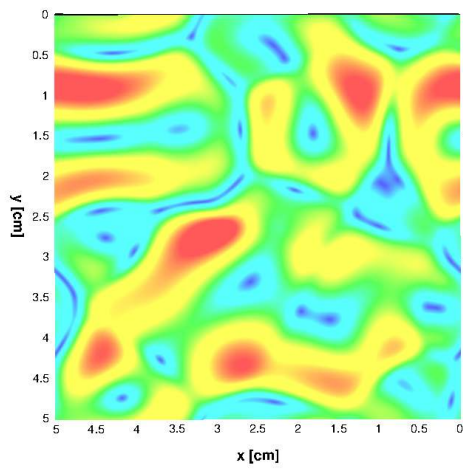
(b) $time = 44s$



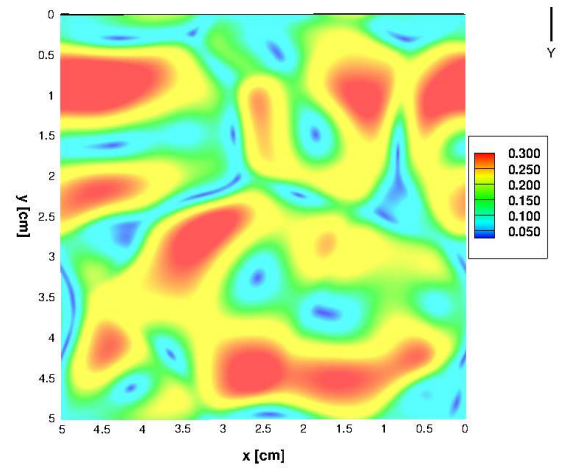
(c) $time = 48s$



(d) $time = 52s$

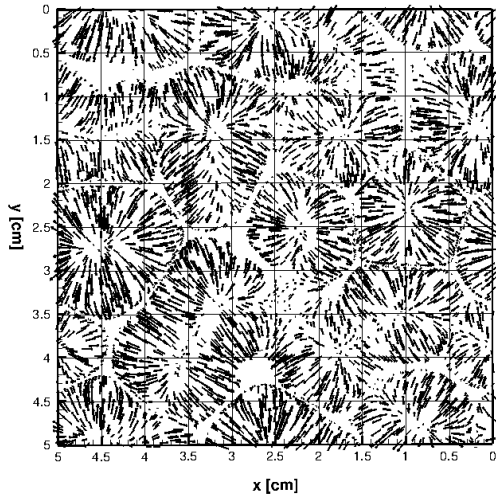


(e) $time = 56s$

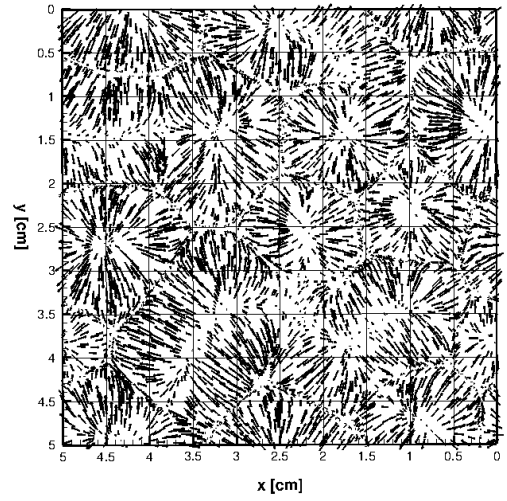


(f) $time = 60s$

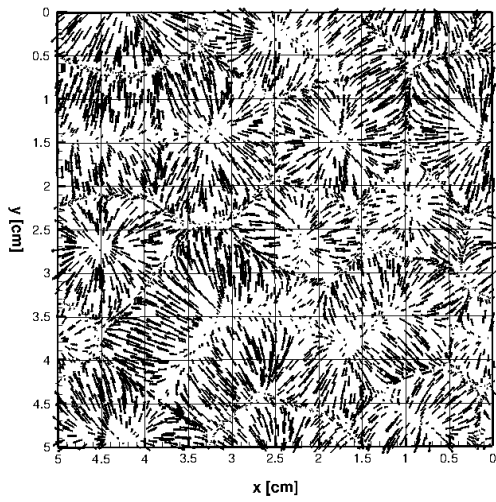
Figure 5.15: *velocity magnitude at interface in 4 second intervals in cm/s*



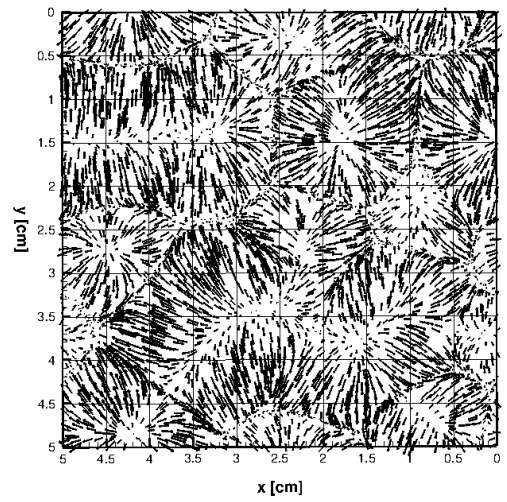
(a) *time = 40s*



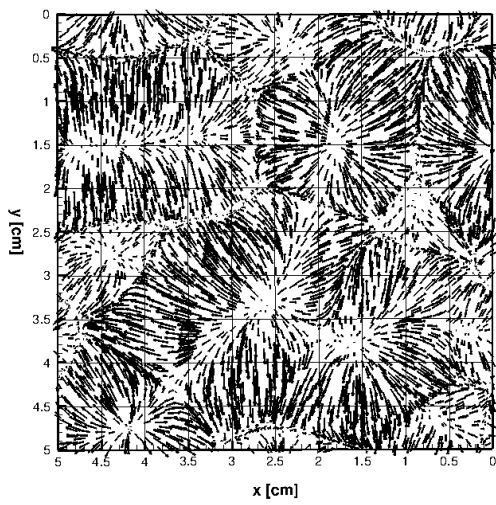
(b) *time = 44s*



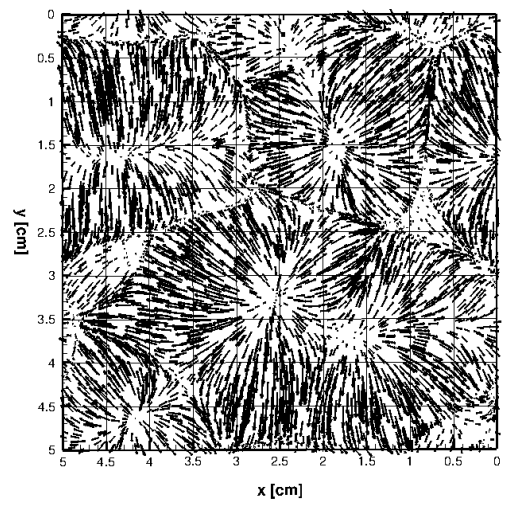
(c) *time = 48s*



(d) *time = 52s*

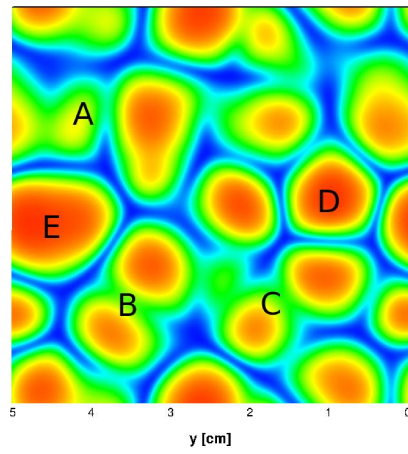


(e) *time = 56s*

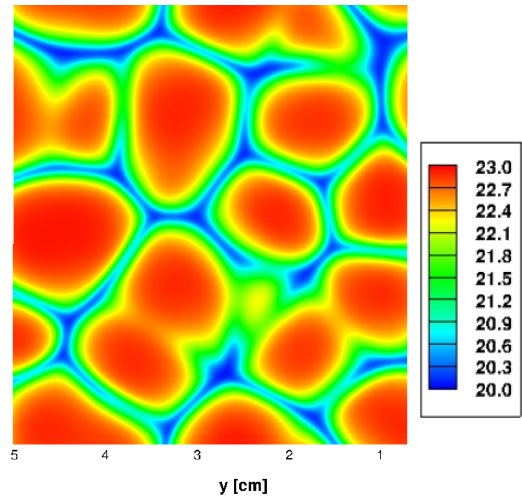


(f) *time = 60s*

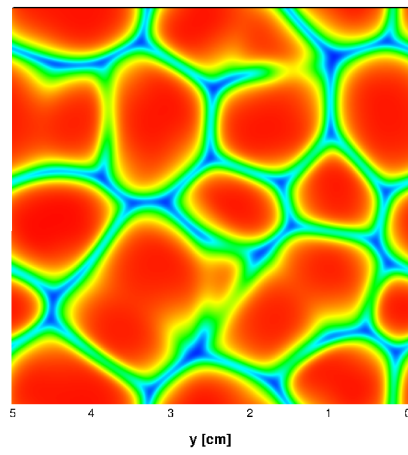
Figure 5.16: *velocity vectors at interface in 4 second intervals*



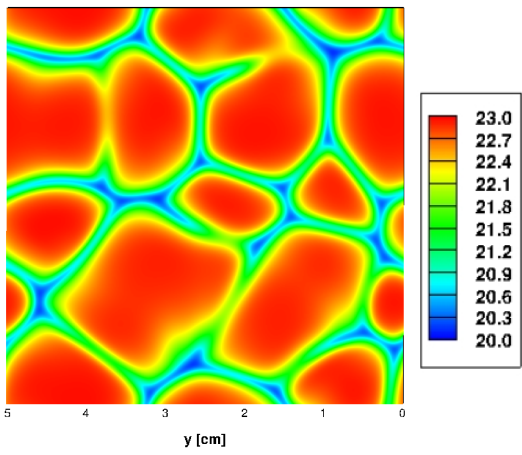
(a) *time = 40s*



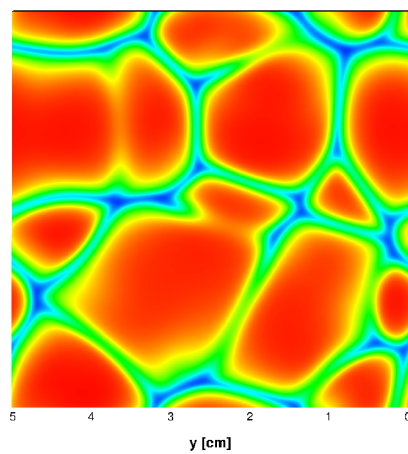
(b) *time = 42s*



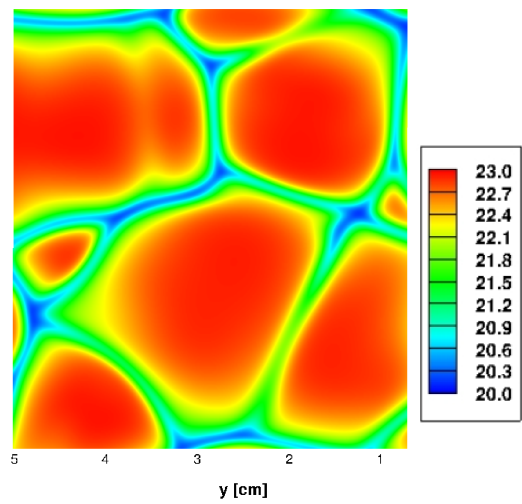
(d) *time = 44s*



(e) *time = 46s*



(g) *time = 48s*



(h) *time = 50s*

Figure 5.17: *temperature plot 1 mm below interface*

5.2.9 Vorticity

The vorticity ω is a measurement of the tendency of the flow field to rotate about an axis.

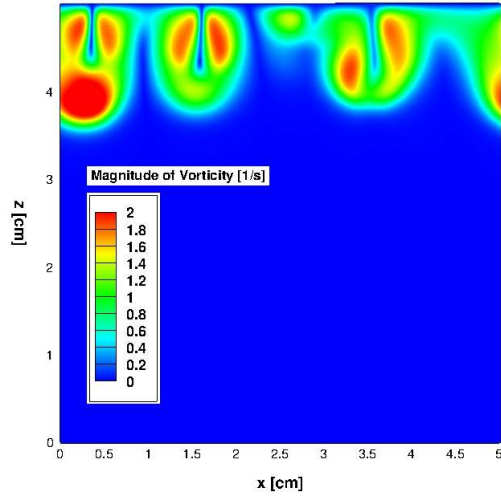
It is a vector defined as,

$$\begin{bmatrix} \omega_x \\ \omega_y \\ \omega_z \end{bmatrix} = \begin{bmatrix} \frac{\partial w}{\partial y} - \frac{\partial v}{\partial z} \\ \frac{\partial u}{\partial z} - \frac{\partial w}{\partial x} \\ \frac{\partial v}{\partial x} - \frac{\partial u}{\partial y} \end{bmatrix} \quad (5.9)$$

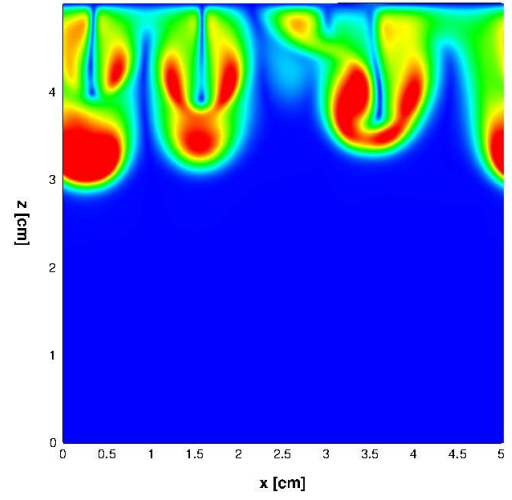
with the magnitude $\|\omega\|$,

$$\|\omega\| = \sqrt{\omega_x^2 + \omega_y^2 + \omega_z^2}. \quad (5.10)$$

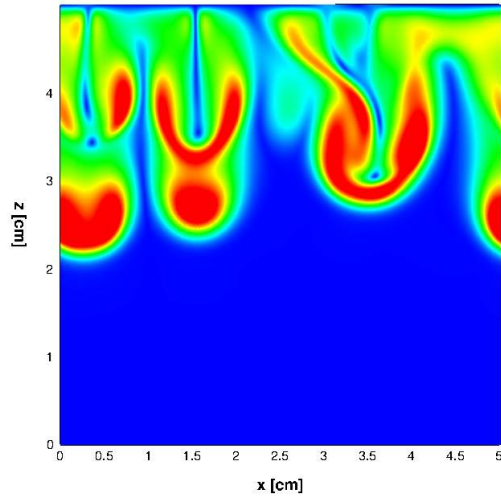
In this section the vorticity magnitude is analysed. Figure 5.18 shows a sequence of the vorticity magnitude in the central vertical cross section as the flow develops between $t = 40s$ and $t = 60s$. It is evident that the vorticity magnitude increases in the overall domain, however, it remains very low near the interface. The flow near the interface is smooth and mainly parallel to it with little intrusions from eddies below. This is even more evident when looking at the sequence in figure 5.19. This sequence shows the vorticity magnitude plotted on isosurfaces of 25% gas concentration. As the sheets of high concentration plunge down and start penetrating deeper areas they are entering areas of higher vorticity. Near the interface on the other hand the vorticity over large areas stays very low.



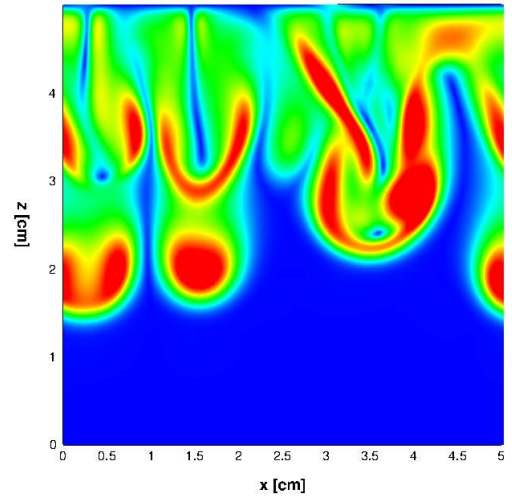
(a) $time = 40s$



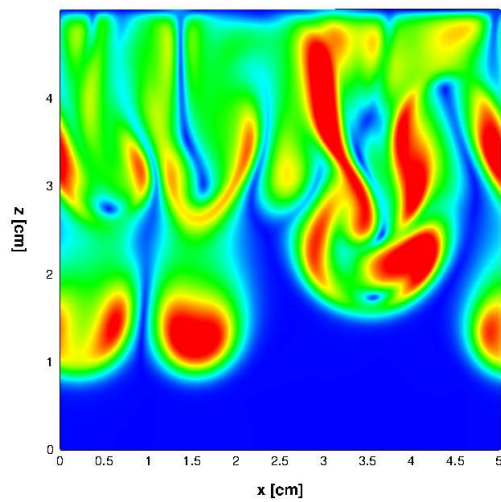
(b) $time = 44s$



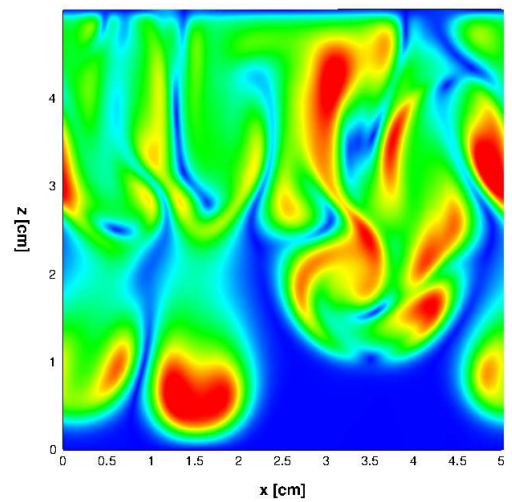
(c) $time = 48s$



(d) $time = 52s$

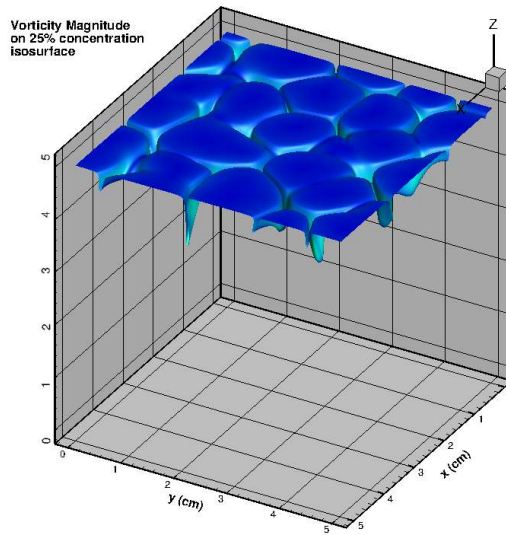


(e) $time = 56s$

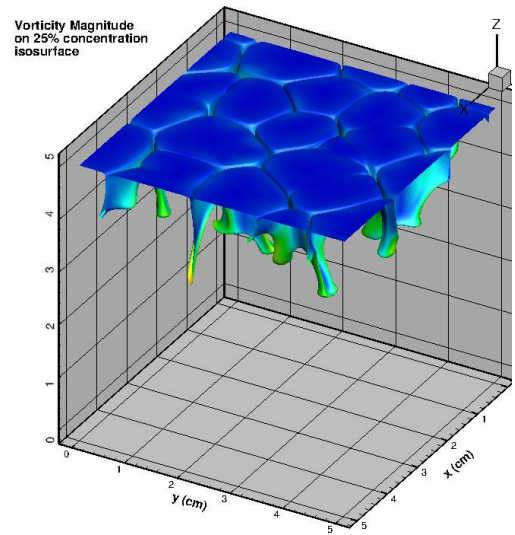


(f) $time = 60s$

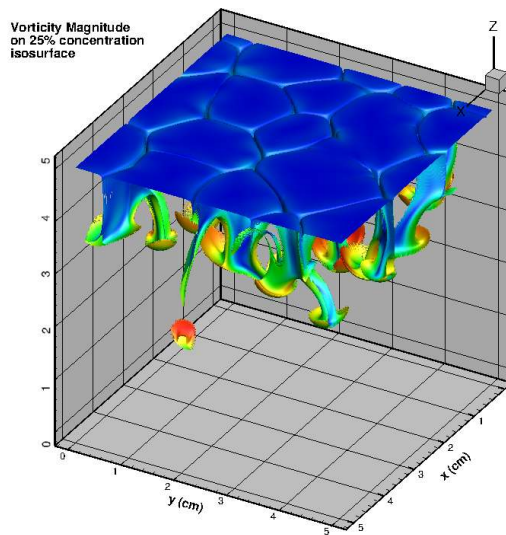
Figure 5.18: vorticity magnitude at $y = 2.5cm$ in 4 second intervals



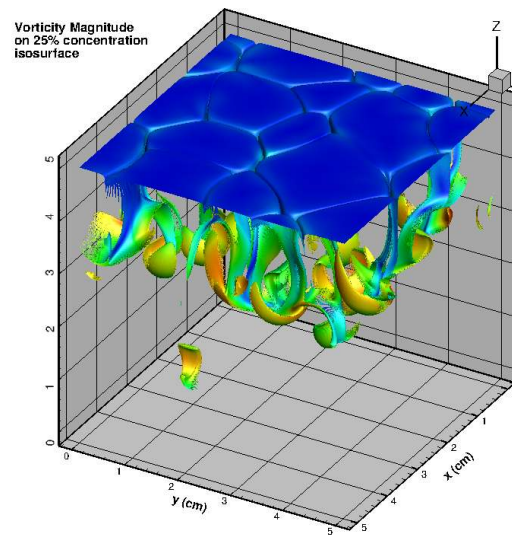
(a) $time = 40s$



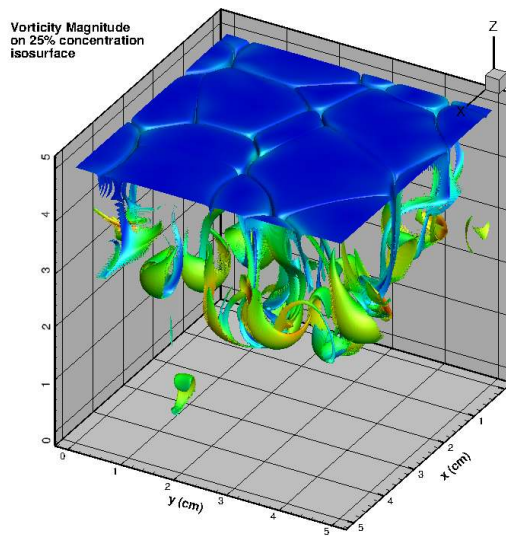
(b) $time = 42s$



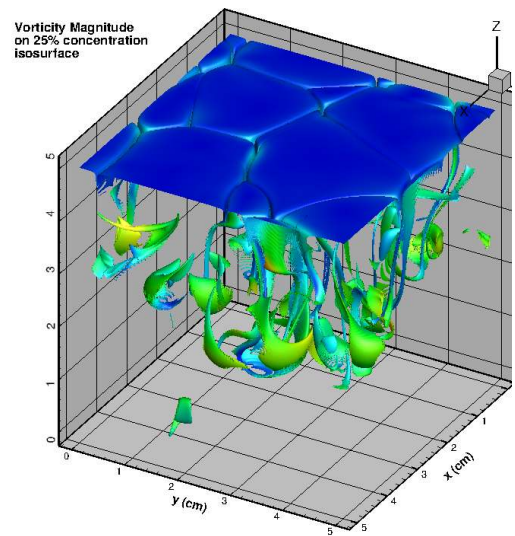
(c) $time = 44s$



(d) $time = 46s$



(e) $time = 48s$



(f) $time = 50s$

Figure 5.19: vorticity magnitude on 25% isosurface in 4 second intervals

Figure 5.20 shows the average vorticity magnitude over time for the total domain as well as in various plane sections nearing the interface. Expectedly, the overall average vorticity magnitude is increasing as the flow sets on and then settles after around 50 seconds at a constant value of 0.7 1/s. The plot also shows the average vorticity magnitude in plane sections near the interface and those reveal that the magnitude is way below the total average closer to the interface. The closer to the interface the lower is the average vorticity. Another observation that can be made is that the average vorticity in the plane sections near the interface increases sharply when the flow sets in at around $t = 35s$ but then decreases again at $t \approx 42s$ and then stabilizes. It remains at low levels therefore quantitatively proving that there is little intrusion from eddies into the concentration boundary layer. The turbulence lower down from the interface does not impinge on the concentration boundary layer. The confined sheets of high gas concentration are ripped apart and swirled around in eddies in the lower parts of the domain but very near interface there is not much intrusion from eddies into the concentration boundary layer.

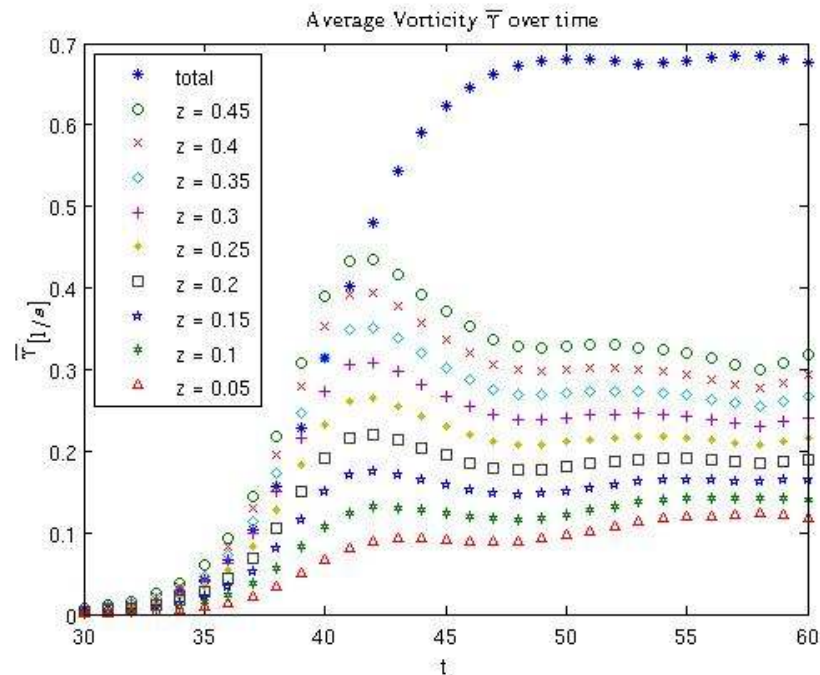


Figure 5.20: average vorticity magnitude over time; total and in plane sections near the interface

5.2.10 Mean and fluctuating concentration

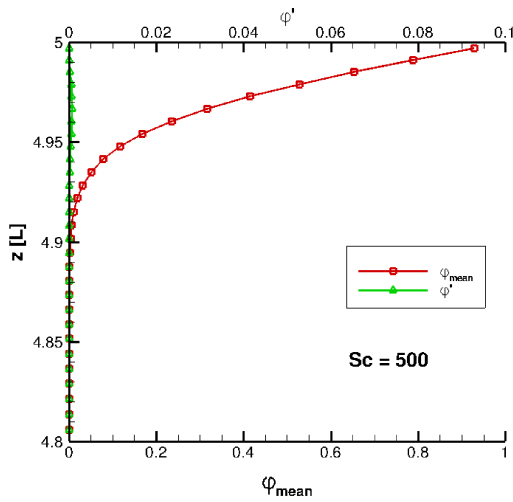
The normalized concentration φ is spatially averaged in horizontal layers of cells. As the grid is hexagonal and horizontally uniform there are individual layers of 399×399 cells (see figure 5.1) on the base grid on which the variables are output (see also figure 3.3). The spatially horizontal mean concentration is calculated as,

$$\bar{\varphi} = \frac{\sum_{i=1}^n \varphi}{n} \quad (5.11)$$

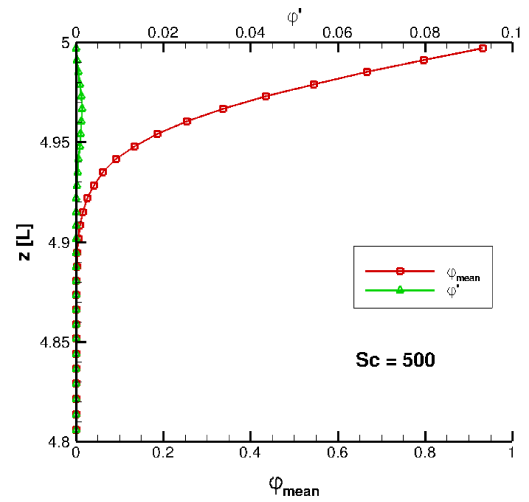
where n is the number of cells per horizontal layer. The concentration fluctuation φ' is the standard deviation of the spatially horizontal mean concentration $\bar{\varphi}$.

$$\varphi' = \sqrt{\frac{1}{n} \sum_{i=1}^n (\varphi - \bar{\varphi})^2} \quad (5.12)$$

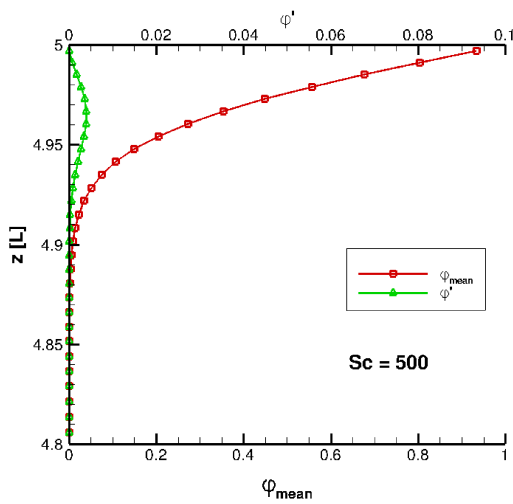
Figure 5.21 shows a sequence of the vertical mean and fluctuation concentration profiles in intervals of $\delta t = 2.5s$ in the proximity of the interface. In figure 5.21a in the sequence the fluid can be considered motionless. The mean concentration profile has developed by diffusion only and, in fact could be predicted analytically (see eq. (4.4)). The concentration fluctuation in the horizontally averaged direction is zero as the diffusion process is technically one dimensional when the fluid is stationary. In the subsequent time steps it can be observed that the fluctuations rise as the convective flow develops. Whereas they are zero at the interface by the boundary condition (the entire interface is saturated) they increase with depth and in the bulk region decrease again. In hand with this comes a thinning of the mean concentration profile. Please note that only data on the base grid is plotted whilst data in the simulation was calculated on the $R = 2$ refined grid.



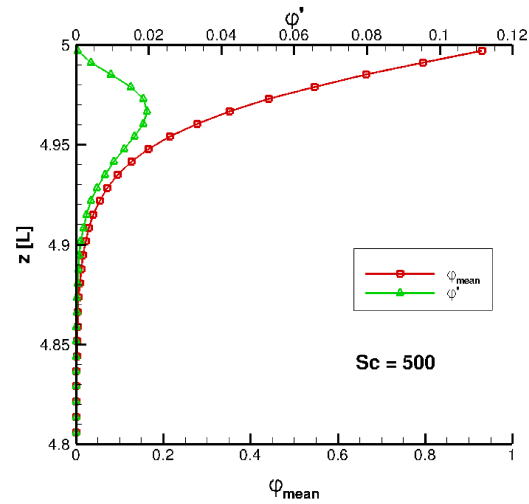
(a) time = 27.5 s



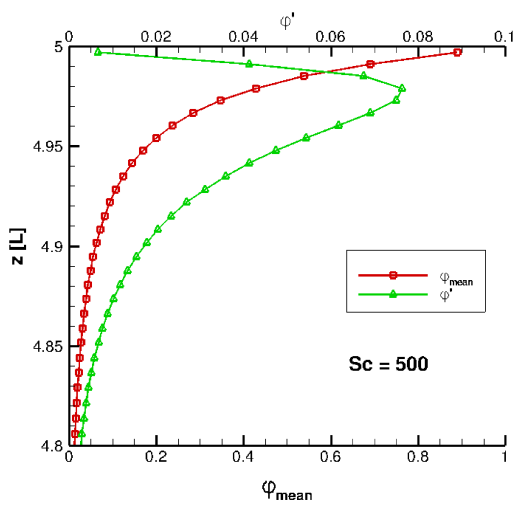
(b) time = 30 s



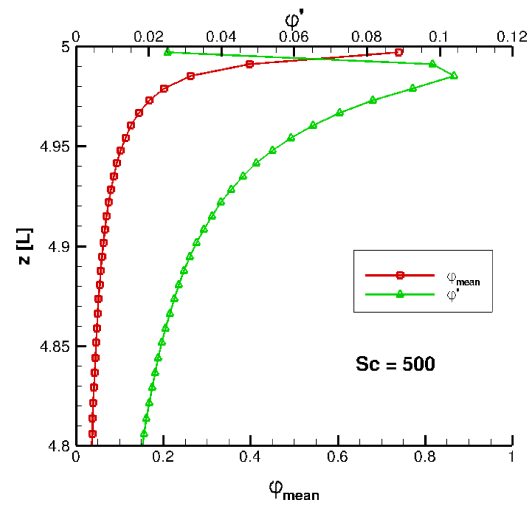
(c) time = 32.5 s



(d) time = 35 s



(e) time = 47.5 s



(f) time = 40 s

Figure 5.21: sequence of vertical mean and fluctuating concentration profiles

5.2.11 Boundary Layer Thickness

The thickness of the concentration boundary layer at the interface for soluble gases is in the order of hundreds of μm at maximum. This makes the experimental measurement of the concentration boundary layer very difficult. Measurements with intrusive methods (Chu and Jirka [19], Brumley and Jirka [12]) have the disadvantage that the thickness can only be measured at one point at the time. The *actual* average thickness is not known as instantaneous measurements of the entire boundary layer are not feasible. The combined PIV-LIF method by Herlina [38] enabled instantaneous measurements of the boundary layer thickness in planar sections. However the global average thickness of the boundary layer across the entire interface remains unknown. All experimental efforts to determine the boundary layer thickness hence rely on the analysis of the vertical mean concentration profile as variations across the interface are not known. The consequence of this is that there are different ways of interpreting the boundary layer thickness when analysing experimental data. For instance, Chu and Jirka [19] proposed an exponential function for the normalized mean concentration profile

$$\varphi^* = e^{-z^*/\delta_e}, \quad (5.13)$$

in their experiments in a grid stirred tank. φ^* is the normalized gas concentration as defined in (3.7). The value δ_e in (5.13) can be interpreted as the measured boundary layer thickness, z^* is the distance measured from the water surface downwards, but again this would be based on the mean concentration profile measured from various point probes. The actual mean value of the boundary layer remains unknown when using a bulk method.

A much more advanced method to determine the boundary layer thickness is to use the vertical profile of the concentration fluctuation φ' . This is possible in numerical simulations as these fluctuations are known. Numerical simulations enable the calculation of the *entire* boundary layer thickness across the interface as the entire concentration field is known over time. This is a great advantage over experiments and does not require the use of time averaged single measurements and mean profiles. The boundary layer thickness can be

defined as the depth where the *maximum* fluctuations occur. This definition is based on the argument that fluctuations are low at both, the interface (fully saturated) and also further away from the mixing zone in the bulk region. In between there is depth where a local maximum of fluctuations is present. The advantage of this method is that the fluid motion and mixing is represented in the fluctuation whereas if only the mean concentration profile is used for the definition of the boundary layer thickness there remains an unknown element of *where* mixing takes place as this can not reliably be estimated when only looking at the mean profiles.

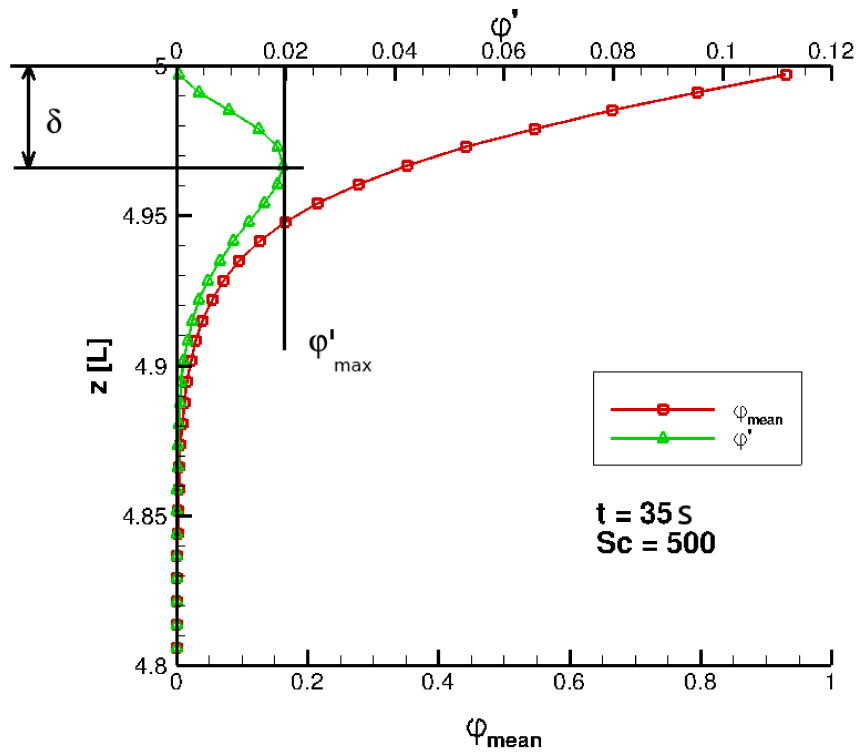


Figure 5.22: *definition of the boundary layer thickness*

Figure 5.22 depicts the definition of the boundary layer as the depth of where the maximum concentration fluctuations occur at the example of the fluctuation and mean profiles at $t = 35s$.

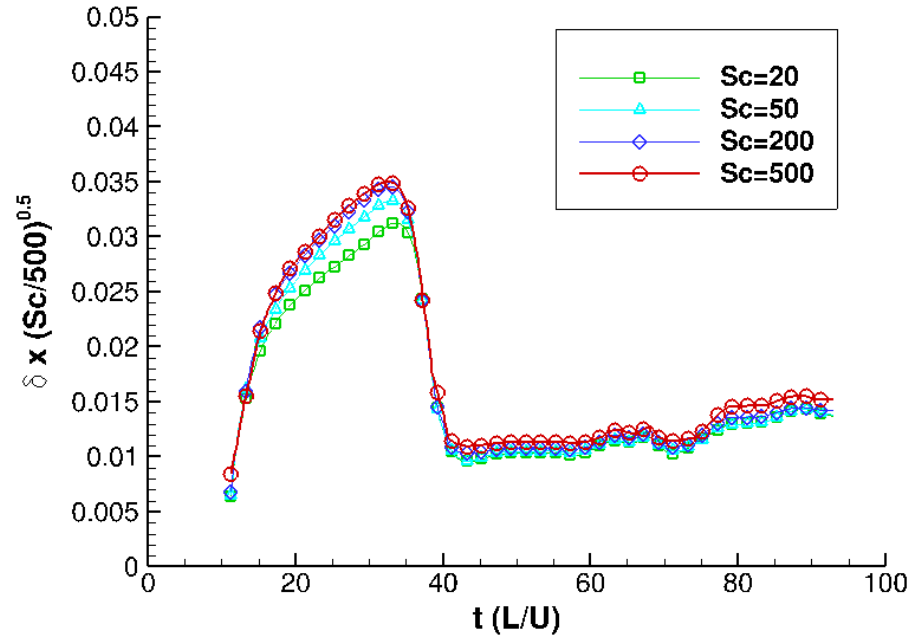


Figure 5.23: *boundary layer thickness over time*

Figure 5.23 shows the evolution of the boundary layer thickness δ over time from the $R = 2$ simulation for the four Schmidt numbers $Sc = 20, 50, 200$ and 500 . The results have been scaled by the $Sc^{-0.5}$ power law which shows good agreement. The slightly higher value for $Sc = 500$ might be caused by interpolation error. Figure 5.24 shows a snap shot of the fluctuation profiles for the four Schmidt numbers at $t = 37.5s$. It can be seen that the maximum for $Sc = 500$ occurs within the first 5 data points. Each maximum was calculated with a first order gradient based linear interpolation. As the gradient change at the maximum for $Sc = 500$ is higher relative to the others the first order interpolation might introduce a slight inaccuracy that can be seen in the time evolution in figure 5.23.

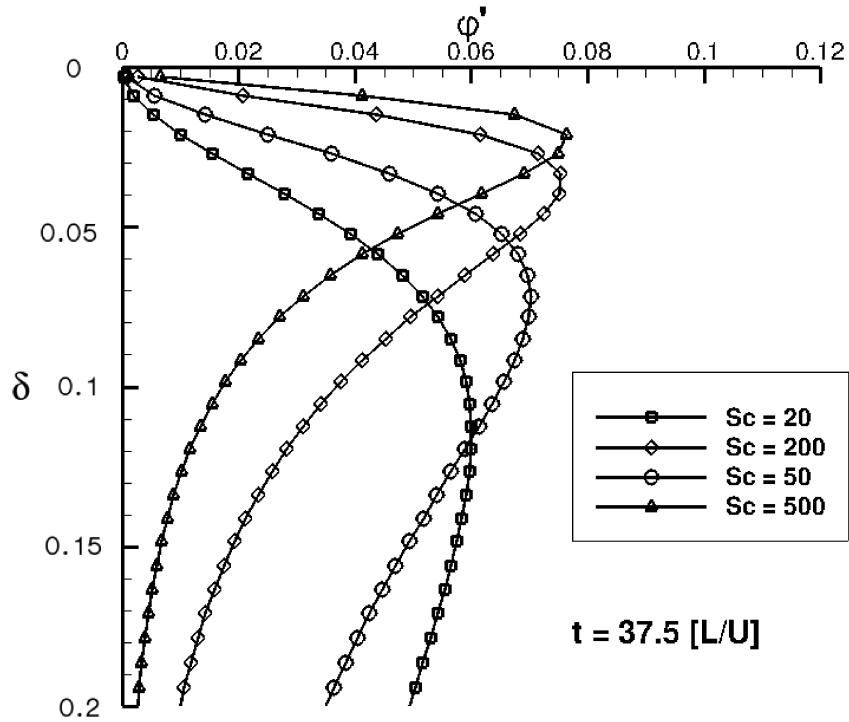


Figure 5.24: *unscaled fluctuations at $t = 37.5s$*

A further method to analyse and visualise the boundary layer is the use of concentration isosurfaces. The isosurfaces give more insight into the topological characteristic of the boundary layer. Here the depth of the the isosurface of 10% saturation was monitored as schematically defined in figure 5.25. The distance between an isosurface of 10% saturation and the interface is defined as δ_{iso} . Only values of $\delta_{iso} < 1mm$ are considered, as there are thin areas where the isosurface is 'pulled down' in thin sheets (see figure 5.3).

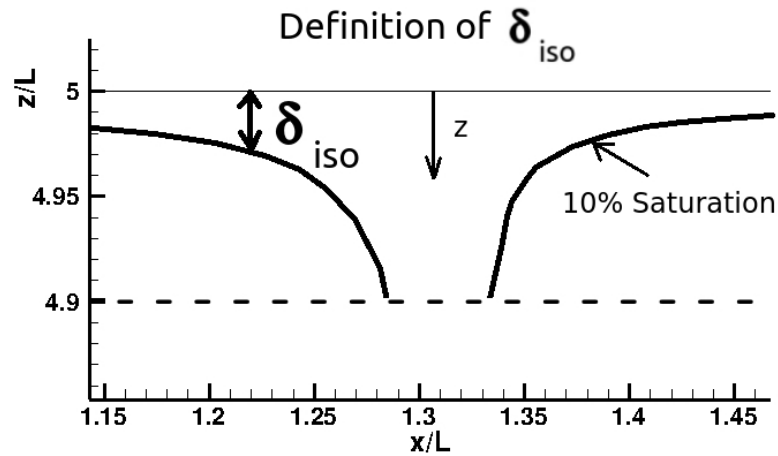
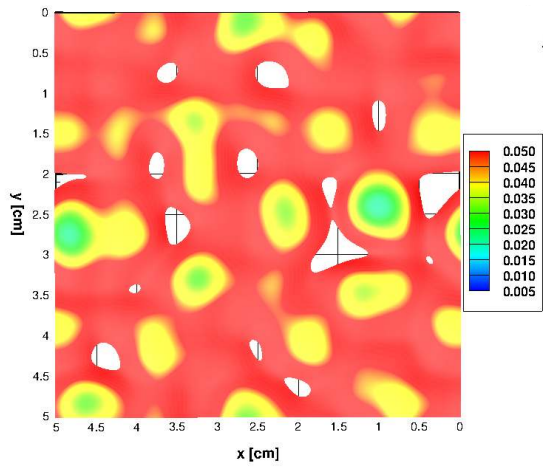
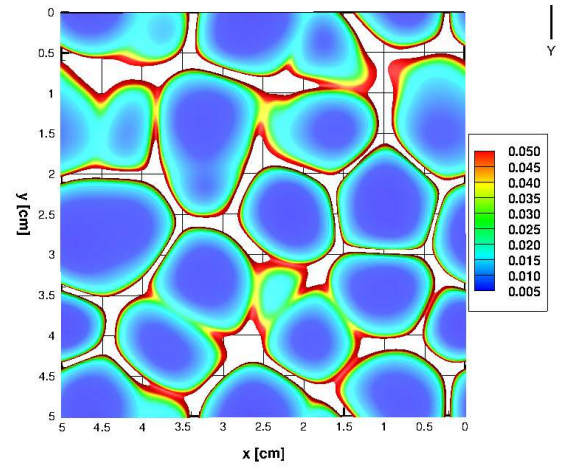


Figure 5.25: Definition of the isosurface thickness δ_{iso}

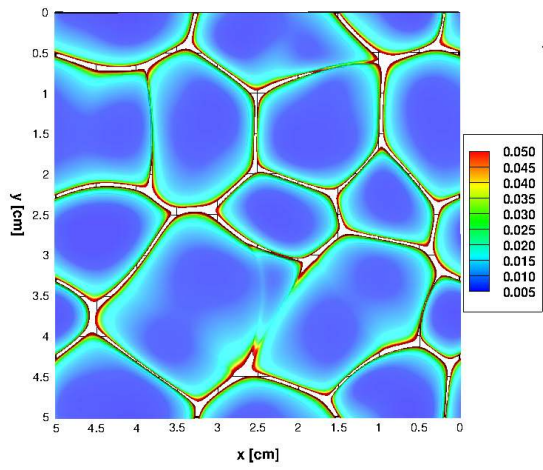
Figure 5.26 shows a sequence of plots where the depth is plotted on the 10% concentration isosurfaces. Only the isosurfaces within 1mm of the interface are shown. From figure 5.26 it is evident that for large proportions of the interface there is a relatively low and uniform depth of the 10% saturation threshold. Initially the isosurface is wavy and some areas are above the clipping range of $\delta_{iso} = 0.1\text{cm}$ (fig. 5.26a). As time progresses the typical convective cell pattern forms and δ_{iso} reduces. This is supported by figure 5.27 which shows the minimum and average depth of the isosurface δ_{iso} over time. The depth becomes smaller when the convective flow sets in. Interestingly it then remains at a nearly constant value. It is also interesting to note that the value of the boundary layer thickness δ as found in figure 5.23 lays between the minimum and average thickness δ_{iso} found in figure 5.26. Looking at the sequence in figure 5.26 it is visible that even though the convective cells increase in size and merge, the mean depth of the isosurface remains nearly constant over large proportions of the area. Only at the edges of the downward plunging sheets there is an increase in depth present.



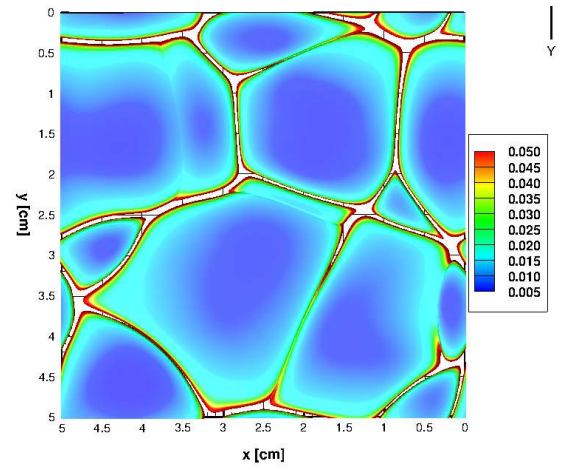
(a) $time = 35s$



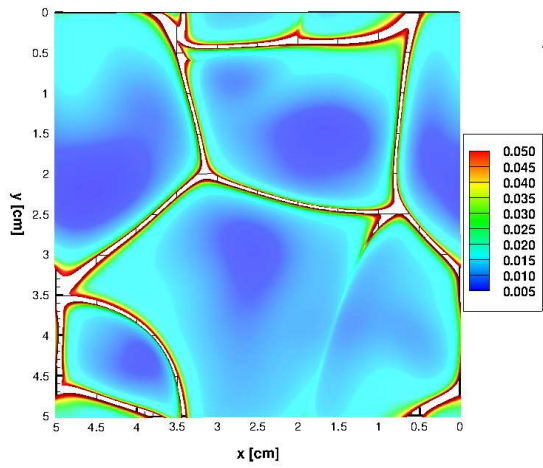
(b) $time = 40s$



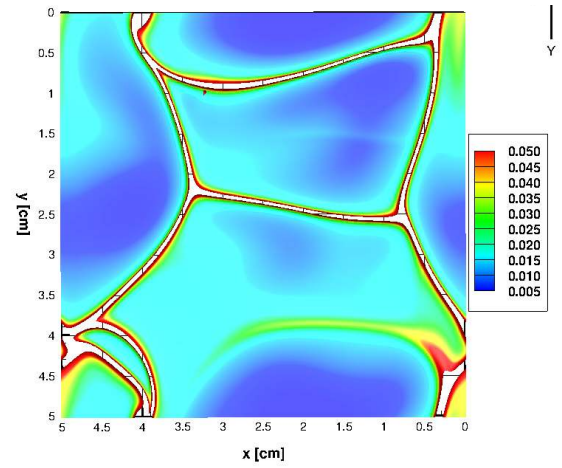
(c) $time = 45s$



(d) $time = 50s$



(e) $time = 55s$



(f) $time = 60s$

Figure 5.26: depth δ_{iso} plotted on the isosurface

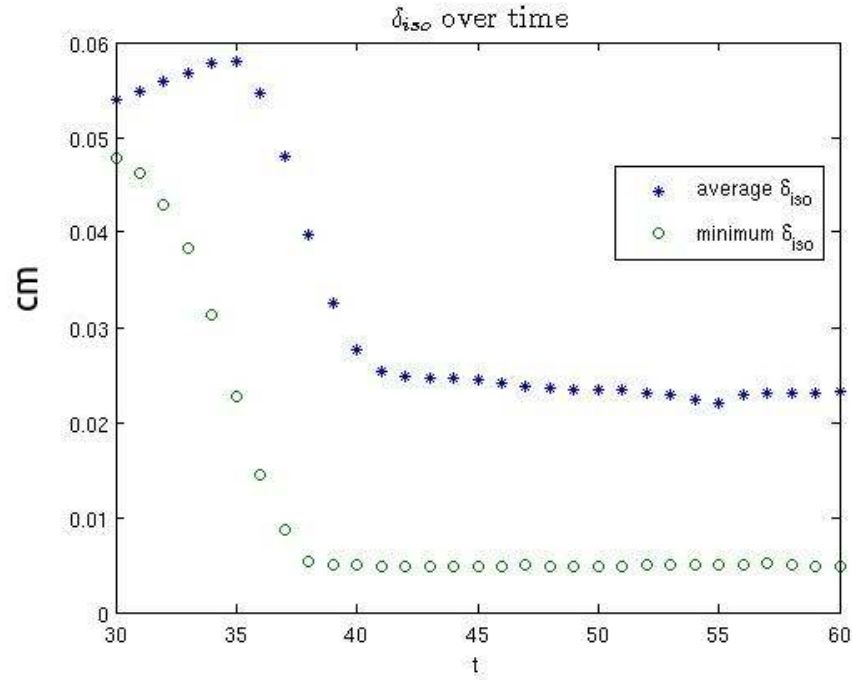


Figure 5.27: Minimum and average δ_{iso} over time for $Sc = 500$

5.3 Comparison to Experiments

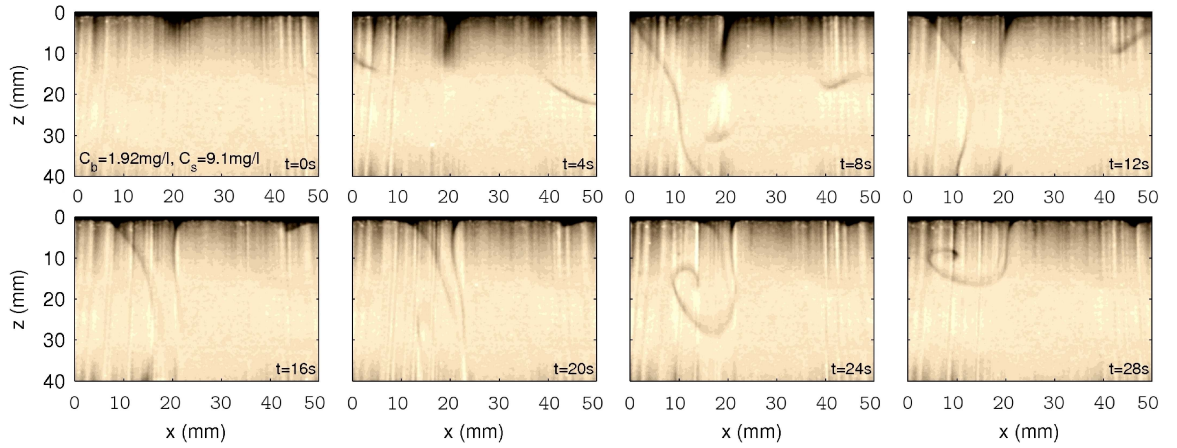
The gas transfer process across an air-water interface is characterised by three physical quantities; namely the concentration, the temperature and the velocity. The temperature differences are driving the flow field so the velocity field is a result of the temperature field and subsequently the velocity field influences the convective proportion of the mass transfer. To observe the mechanisms experimentally in detail it is necessary to resolve the concentration field in time and space simultaneously with the velocity field. The concentration boundary layer near the interface has a thickness of only a fraction of a millimeter, hence non-intrusive measurement techniques are essential to not influence the flow field and thus the experimental results.

5.3.1 Concentration Field

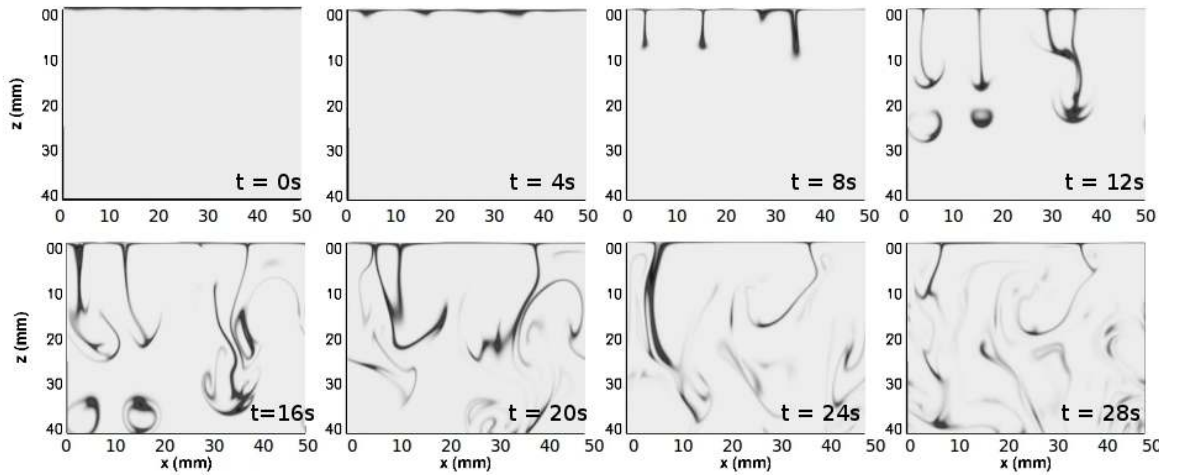
The gas concentration field can be experimentally visualised with the Laser Induced Fluorescence (LIF) technique, first developed by Vaughan and Weber [91]. The LIF technique enables visualisation of planar oxygen concentration fields. The LIF technique uses so called oxygen quenching, which takes advantage of the fact that the fluorescent intensity which is proportional to the fluorescent lifetime of a dye is quenched or reduced by the presence of oxygen molecules in a solution. Pyrene butyric acid (PBA) has been identified as the best dye for this method [91]. Wolff and Hanratty [97] showed that the fluorescence lifetime of PBA reduces from 160 ns in the absence of oxygen to 65 ns in air-saturated solution. This changes the intensity of the fluorescence depending on the oxygen levels in the solution. Higher oxygen levels lead to lower fluorescence, hence the oxygen concentration can be made visible by the intensity of the emitted fluorescence.

In this section the numerical results are compared to the laboratory measurements conducted by Jirka et al. [46] at KIT. In the experiments instantaneous 2D oxygen concentration fields were visualized using the LIF technique in an area of approximately 60×80 mm in buoyant-convective flow. The experiments were performed in a $50 \times 50 \times 65$ cm³ tank and the water depth was about 42 cm. The surface temperature was 3 °C lower than the bulk temperature of the water which is the equivalent temperature boundary condition that was applied in the numerical simulations. Figure 5.28 shows a comparison of the concentration field in a vertical planar section. Note that the DNS results show the top section of the domain that has the same dimension as the LIF-maps. The actual experimental domain was much larger so the sides and bottom in these plots can be considered as open boundaries. For reasons of better comparison the timescale was set to $t = 0$ seconds from the moment when the flow field started moving which was after a simulation time of 33 seconds. Both the spatial distance between high concentration plumes and the size of the eddies were found to be similar in the experiment and the simulation. Because of the low diffusivity of oxygen in water and the rather low turbulence intensity the plumes of high oxygen concentration retain their fine structures. This means that the steep concentration gradients do not smear out because of turbulent diffusion. As a result a good qualitative agreement between the

numerical simulations and the experimental data is obtained.



(a) *Experimental Results*



(b) *Numerical Results*

Figure 5.28: Comparison of flow structures. High oxygen concentration plumes of LIF measurements conducted by Jirka et al. [46] (Fig. 5.28a) and DNS results (Fig. 5.28b). The dark and light colour scaling indicate regions with high and low scalar concentration, respectively. In both cases the surface temperature was 3°C colder than the bulk temperature.

Figure 5.29 shows a comparison of the boundary layer thickness just at the moment when a falling plume begins to develop. The normalized concentration levels obtained from

the numerical simulation (left) and experiments (right) show a very similar pattern and are in good qualitative agreement. The boundary layer appears to be slightly thicker in the experiments. This may be caused by the non-instant cooling of the air in the experiments, hence resulting in a longer period of pure diffusive gas transfer in which the boundary layer can grow for longer before the fluid starts moving. In fact, in some of the experiments Jirka et al. [46] observed that the boundary layer could even grow up to 10mm in thickness before cold plumes started falling down.

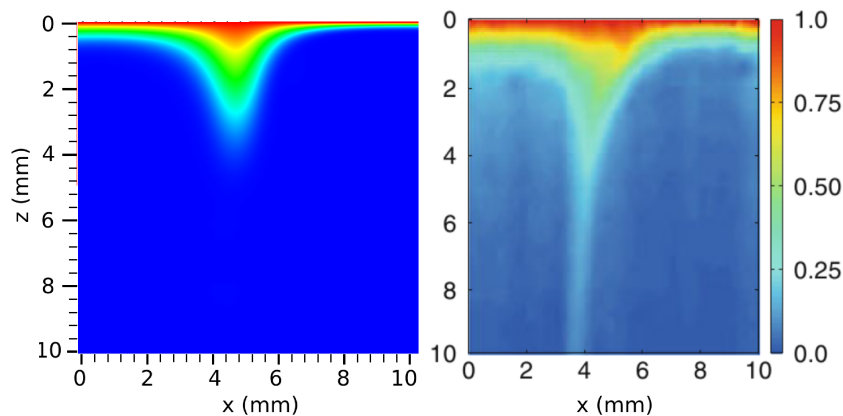


Figure 5.29: *comparison of gas concentration boundary layer just at the beginning of the convection. Numerical results (left), Experimental results conducted by Jirka et al. [46] (right).*

In the experimental result in figure 5.29 the contour of the boundary is not as sharp as in the simulation but this seems to be down to noise and resolution. However, the general distribution of the oxygen concentration and the formation and curvature of the falling plume is in very good qualitative agreement.

5.3.2 Temperature Field

A well-known method to visualize flows of varying density is Schlieren photography first developed by Toepler [90]. The method makes use of the fact that changes in density in a transparent fluid change the refractive index.

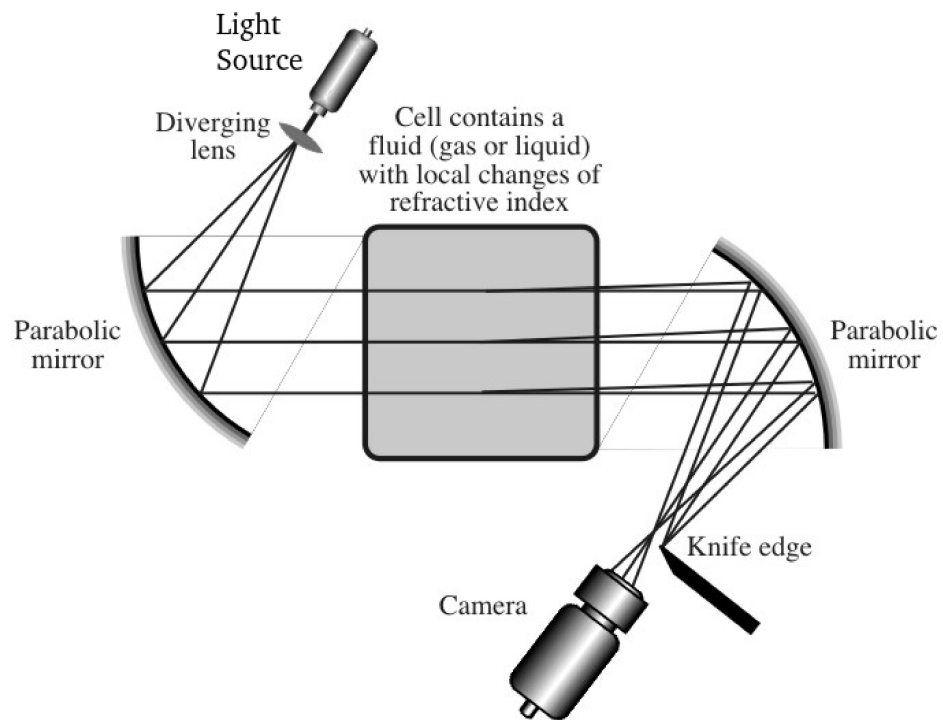


Figure 5.30: *Principle of Schlieren Photography*

The basic principle of Schlieren Photography is depicted in Figure 5.30. Collimated light, whose rays are parallel, is shining through an area with a density gradient. The key element of the system is a knife edge that is located at the focal point of the system to block half the light. The change of the refractive index in the area where a density gradient is present will cause a deflection of the rays. They will focus imperfectly which means their focal point will be moved and blocked by the knife edge. Figure 5.30 shows the path of both the straight and deflected light paths. The result of this blocking of deflected rays is a difference in light intensity corresponding to the negative or positive density gradient in the direction normal to the knife edge.

The Schlieren technique was used by Spangenberg and Rowland [85] to visualize the temperature field in convective flow in an open water tank. Spangenberg and Rowland [85] could show that cold fluid is plunging downwards in thin vertical sheets. The top views

of their experiments showed that the plunging regions appear sometimes straight, curved or branched or terminated with no fixed patterns. They found that the patterns formed do have the net like tessellation found by Thomson [89] particularly when the temperature difference between the water and the ambient air was between one and three degrees.

In the experiments carried out by Spangenberg and Rowland [85] the tank was covered and left undisturbed to eliminate all convection. The cover was removed and the water and air temperatures recorded by thermopiles and schlieren images were monitored for indications of density gradients resulting from the surface cooling.

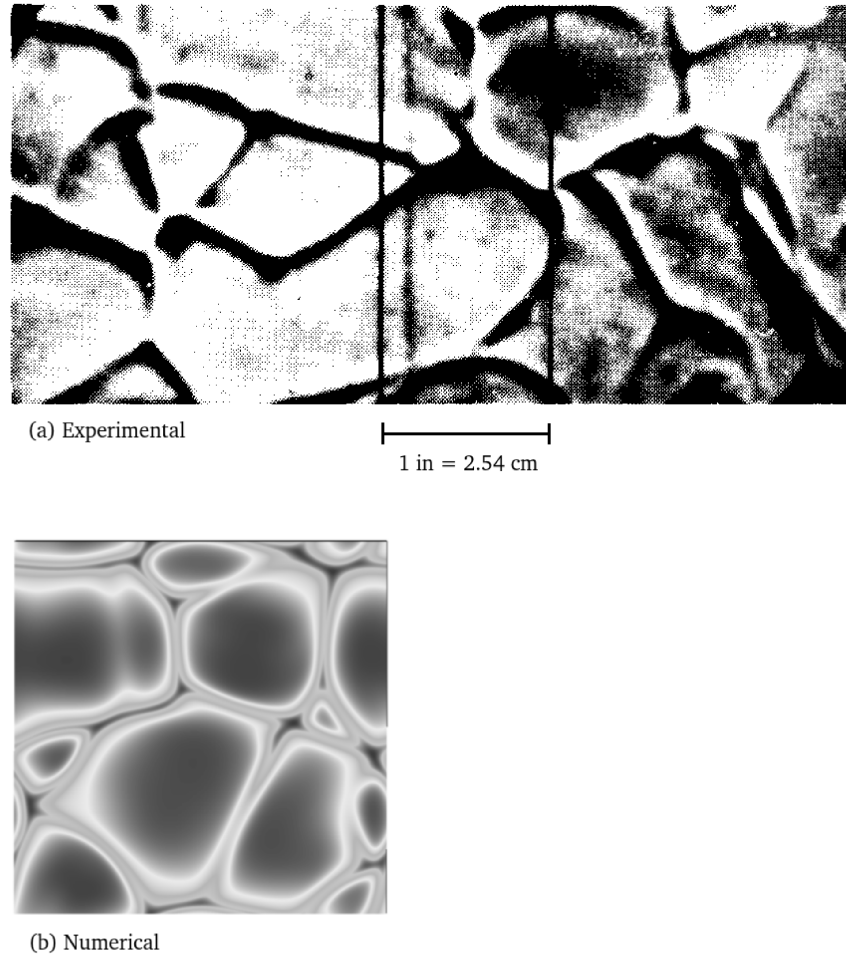


Figure 5.31: Comparison of (a) experimental Schlieren photographs and (b) numerical results of temperature field.

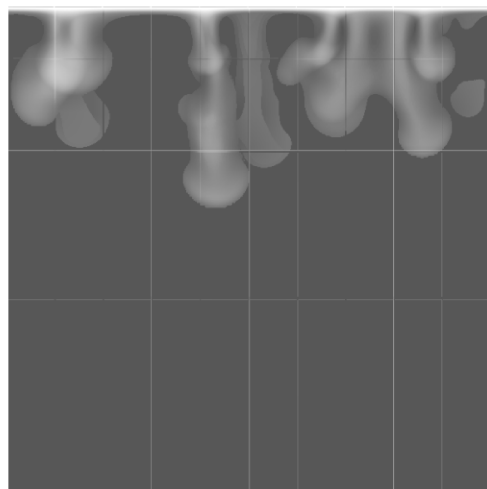
Figure 5.31 shows a comparison between the experiments [85] and the numerical results. The numerical results show a greyscale image of the temperature field 1 mm below the interface after 50 seconds simulation time. The experimental results are obtained from a motion picture film showing the schlieren photograph of the top view. The temperature difference was in the same range as in the numerical simulations. The images are scaled to the same size. The markers in the experiments were 1 inch apart. It can be seen that the pattern of cold sheets is qualitatively in very good agreement. The pattern shows the 'net

like' structure that was described by Thomson [89].



(a) Experimental

1 in = 2.54 cm



(b) Numerical

Figure 5.32: Comparison of (a) experimental Schlieren photographs and (b) numerical results of temperature field.

Figure 5.32 shows a comparison of experimental Schlieren photographs and numerical results of temperature field. The schlieren photograph shows columns together with sheets immediately after the convection began. In the experiments the typical mushroom structure could be also found. Spangenberg and Rowland [85] also observed that a few seconds after the formation the columns spread into sheets to form branched patterns or cells. The

water temperature in the experiments was 24.6 °C and the air temperature 20.9 °C so the temperature difference was very similar to that used in the numerical simulation.

The numerical results show a translucent grey scale contour plot of the temperature through the domain as seen from the side. Both images are scaled to the same size. The observations made in the simulations are in very good agreement with the observations made by Spangenberg and Rowland [85].

Chapter 6

Conclusions and Recommendations

6.1 Conclusions

The aim of this study is to simulate the low-diffusive gas transfer across the air-water interface using Direct Numerical Simulation in order to gain a better understanding of the detailed mechanisms that control that process. This study focuses in particular on the buoyant-convective driven flow. When considering the diffusion of soluble gases such as O_2 or CO_2 into water the Schmidt number for the mass transfer of such gases is ≈ 500 which will result in a very low diffusivity. It is known that the concentration boundary layer which forms near the interface is only of the order of ten to hundreds μm thick. The low diffusivity and the very thin boundary layer mean that there are steep concentration gradients present. Near the interface the fluid is almost fully saturated whereas only less than 1 mm below in the bulk region the gas concentration levels are nearly zero. As the fluid is subsequently set in motion by natural convection mixing will take place. Saturated fluid from the interface is transported away to deeper regions but because of the low diffusivity high concentration fluid can still be in very close proximity to fluid of low concentration with a steep gradient between them over a short distance. The main challenge is to apply a numerical method that can reliably resolve the diffusion-convection equation when a very low diffusivity is present.

It is therefore important to resolve the convective and diffusive transport of the gas concentration field with a suitable numerical method. To achieve this a modified version

of the WENO5 scheme of Shu and Jiang [81] is deployed to discretize the scalar convection (the scalar being the gas concentration). The use of the WENO scheme to solve a low-diffusive scalar transport problem has the advantage of being able to capture steep gradients within only a few gridpoints without losing accuracy because of numerical errors such as oscillations or smearing. WENO schemes are in fact capable to even resolve the convection of discontinuities without exhibiting oscillations.

To evaluate the accuracy of the numerical method a series of tests have been performed. Scalar transport by convection was tested in 1D experiments on uniform and non-uniform grids. In those test the diffusive terms were not included in the transport equation in order to predict the accuracy of the WENO scheme. A full period of a sine wave was convected through the one-dimensional domain with periodic boundary conditions on uniform and non-uniform grids with the number of gridpoints ranging from 10 to 640 points. The WENO5 implementation of Liu et al. [61] was compared to the alternative WENO5 scheme developed by Shu and Jiang [81]. The tests showed that the implementation of Shu and Jiang [81] show a smaller error on coarse meshes. Tests were also performed with a 2D sheared scalar distribution which showed that the order of accuracy increased from 2 to 4 when using finer grids. Numerical tests were also performed to determine the order of accuracy for the discrete solution of pure scalar diffusion in one dimension. These test revealed that the fourth-order central scheme indeed achieved a fourth-order accuracy even on stretched meshes.

The two WENO5 schemes and the fifth-order upstream central method were also tested for their performance when solving scalar convection with steep gradients in and unstable flow. 2D simulations of a buoyant-convective flow with low diffusive scalar at the top boundary were performed. It could be clearly demonstrated that the WENO5 schemes do not exhibit any oscillations near strong gradient changes as they appear in the physical case of low diffusive gas transfer in a liquid. The WENO5 scheme of Liu et al. [61] was therefore chosen as the numerical method deployed to carry out the investigation in buoyancy driven gas transfer at a realistic Schmidt number.

Further 2D tests focused on the mesh sensitivity. It could be demonstrated that the velocity field is fully resolved when using a 400×256 grid. A dual mesh method has been

introduced where the velocity field is solved on the base grid of 400×256 grid points, whereas the transported scalars have been resolved on a variety of finer meshes. The grid for the scalars was refined by factor $R = 2$, $R = 3$ and $R = 5$, respectively, and the velocities were interpolated from the base grid to the refined mesh. It could be shown that there is a significant gain to resolve the scalar on the finer dual grid. There was a big gain in resolution of resolving the scalars on a grid with $R = 2$. There was only a small gain in resolution for $R > 3$ and the scalar field could be considered as fully resolved for a dual grid with $R = 3$.

The findings from the test in 1D and 2D enabled a proper setup of the 3D simulations aimed to resolve the 'real' physical process. The domain was extended to three dimensions but the same mesh was used in the vertical direction as in the previous 2D simulations with a $400 \times 400 \times 256$ points base grid. A qualitative comparison of the gas concentration field over time using several scalar grid refinements was carried out. The 2D results were confirmed: there was no improvement of resolution observed for refinements above $R = 2$. The results using the refined scalar grid with $R = 3$ can therefore be regarded as a fully resolved where numerical errors are negligible.

This enabled detailed observations of the gas concentration field in full transient 3D simulations. All field variables were exported every second and the entire process was simulated for 93 seconds of physical time. It was observed that the plunging of cold saturated fluid begins after around 35 seconds. Isosurfaces of the gas concentration showed that cold saturated water is collected along lines and plunges down in sheets and columns. The thin sheets of high gas concentration and the columnar mushroom structure was also observed by Jirka et al. [46] in experiments. The observed net like pattern of cold sheets as seen from above was also in good agreement with schlieren photography experiments by Spangenberg and Rowland [85]. A direct comparison of the vertical gas flux and the temperature field showed that near the interface the low temperature areas in form of the net like lines are congruent with areas of high vertical flux. Further away from the interface this relationship weakens and the temperature field does not necessarily indicate where areas of high gas concentration are.

A detailed study of the transfer velocity K_L was carried out for four Schmidt numbers

ranging from $Sc = 20$ to $Sc = 500$. It could be shown that the process exhibits a very good Schmidt number scalability with the $Sc^{0.5}$ power law. From the transfer velocity K_L the renewal rates r for Dankwerts conceptual Surface Renewal Model could be calculated. The renewal rates were found to be in a similar range to the ones found by experiments in a gird stirred tank by Herlina [38]. This suggests that the gas transfer process in buoyant convection is an effective method as even though the flow is less turbulent there is a similar surface renewal rate as when generating mixing by grid stirring. The horizontally averaged vertical convective and diffusive fluxes were determined. It could be clearly shown that a transition takes place from diffusion only mass flux at the interface to a system dominated by convection further away from the interface (convection means advective mass transport in this context).

A statistical analysis was carried out so that the horizontally averaged mean and fluctuating concentration was determined. This enabled a detailed observation of the average boundary layer thickness, which can be defined as the depth where the concentration fluctuation has a maximum. Similar to the observations made by Jirka et al. [46] it was found that with the onset of the convection the boundary layer thickness reduces. As the convective flow developed, however, and the convective cells merged and changed in size and structure the average boundary layer thickness stayed almost constant.

Qualitative observations were made of the convective cell pattern merging. It was observed that the initial honeycomb-like convective cell structure changes over time and cells change in size and merge. Cells that are separated by warmer fluid seem to have a higher tendency to merge. The cell size near the interface and the plunging sheet like structures are in good agreement with experimental results [46, 85].

From the temperature gradient at the interface the heat flux was also monitored. A strong correlation between transfer velocity K_L and heat flux could be observed and the results found in this study are a good reference for experimental field measurements [78].

The technique provided in this work makes it possible for the first time to determine the major quantity of interest, the transfer velocity K_L , in a buoyant convectively driven flow *reliably and directly* without using empirical models for such high Schmidt numbers. This is

owed to resolving the gas convection-diffusion in the entire domain, which the technique of employing a WENO5 scheme combined with the dual meshing approach made possible.

6.2 Recommendations for further studies

In this study it has been shown that the gas flux near the interface is dominated by diffusion. The concentration boundary layer near the interface remains largely free from intrusion from turbulence in the bulk region for the convectively driven flow considered here. In natural water bodies also a combination of wind-shear and bottom-shear might occur simultaneously. Therefore, future studies could aim to exploit the effects of an introduction of wind-shear or bottom-shear (stirring) in addition to the buoyant convection. The results obtained in this work can provide an excellent reference and so the impact of the bottom or wind-shear on the transfer velocity K_L could be obtained. The WENO scheme method used in this study could be adopted for solving the gas transport in a fluid where the flow is driven by a combination of convection and some external force such as turbulence generated at the bottom. A greater understanding of which mixing mechanism (natural convection, bottom-shear or wind-shear) influences the gas transfer in a certain way could be gained from such further studies.

Bibliography

- [1] Ahlers, G., Grossmann, S., and Lohse, D. (2009). Heat transfer and large scale dynamics in turbulent rayleigh-bénard convection. *Reviews of Modern Physics*, 81(2):503.
- [2] Angelis, V. D., Lombardi, P., and Banerjee, S. (1997). Direct numerical simulation of turbulent flow over a wavy wall. *Physics of Fluids*, 9(8):2429–2442.
- [3] Atmane, M. and George, J. (2002). Gas transfer across a zero-shear surface: a local approach. *Geophysical Monograph Series*, 127:255–259.
- [4] Balachandar, S., Maxey, M. R., and Sirovich, L. (1989). Numerical simulation of high rayleigh number convection. *Journal of Scientific Computing*, 4:219–236. 10.1007/BF01061502.
- [5] Balsara, D. and Shu, C.-W. (2000). Monotonicity preserving weno schemes with increasingly high-order of accuracy. *J. Comput. Phys.*, 160(2):405–452.
- [6] Banerjee, S. (2007). Modeling of interphase turbulent transport processes. *Ind. Eng. Chem. Res.*, 46(10):3063–3068.
- [7] Banerjee, S., Lakehal, D., and Fulgosi, M. (2004). Surface divergence models for scalar exchange between turbulent streams. *International Journal of Multiphase Flow*, 30(7-8):963–977.
- [8] Bansal, M. (1973). Atmospheric reaeration in natural streams. *Water research*, 7(5):769–782.

-
- [9] Borges, R., Carmona, M., Costa, B., and Don, W. (2008). An improved weno scheme for hyperbolic conservation laws. *J. Comput. Phys.*, 227(6):3191–3211.
- [10] Broecker, W., Peng, T., and Beng, Z. (1982). *Tracers in the Sea*. Lamont-Doherty Geological Observatory, Columbia University.
- [11] Brubaker, J. (1987). Similarity structure in the convective boundary layer of a lake.
- [12] Brumley, B. and Jirka, G. (1987). Near-surface turbulence in a grid-stirred tank. *Journal of Fluid Mechanics*, 183(1):235–263.
- [13] Brumley, B. and Jirka, G. (1988). Air-water transfer of slightly soluble gases: Turbulence, interfacial processes and conceptual models. *Physicochem. Hydrodyn*, 10(3):295–319.
- [14] Calmet, I. and Magnaudet, J. (1997). Large-eddy simulation of high-schmidt number mass transfer in a turbulent channel flow. *Physics of Fluids*, 9(2):438–455.
- [15] Calmet, I. and Magnaudet, J. (1998). High-schmidt number mass transfer through turbulent gas liquid interfaces. *Int. J. of Heat and Fluid Flow*, 19(5):522–532.
- [16] Campbell, J. A. and Hanratty, T. J. (1983). Mechanism of turbulent mass transfer at a solid boundary. *AIChE Journal*, 29(2):221–229.
- [17] Canuto, C., Hussaini, M., Quarteroni, A., and Zang, T. (1988). Spectral methods in fluid mechanics. *Springer Ser. Comput. Phys.*, Springer-Verlag, New York, Berlin.
- [18] Chanson, H., Toombes, L., Moog, D., and Jirka, G. (2000). Stream reaeration in nonuniform flow: macroroughness enhancement. *Journal of Hydraulic Engineering*, 126(3):222–224.
- [19] Chu, C. and Jirka, G. (1992). Turbulent gas flux measurements below the air-water interface of a grid-stirred tank. *International journal of heat and mass transfer*, 35(8):1957–1968.
- [20] Curry, J., Herring, J., Loncaric, J., and Orszag, S. (1984). Order and disorder in two-and three-dimensional benard convection. *Journal of Fluid Mechanics*, 147(1):1–38.

-
- [21] Dankwerts, P. (1951). Significance of liquid-film coefficients in gas absorption. *Ind. Eng. Chem*, 43(6):1460–1467.
- [22] Deane, A. and Sirovich, L. (1991). A computational study of rayleigh-bénard convection. part 1. rayleigh-number scaling. *J. Fluid Mech*, 222:231–250.
- [23] DeAngelis, V. and Banerjee, S. (1999). Heat and mass transfer mechanisms at wavy gas-liquid interfaces. *Proceedings of TSFP-1*, pages 1249–1254.
- [24] Deardorff, J. (1972). Numerical investigation of neutral and unstable planetary boundary layers. *Journal of Atmospheric Sciences*, 29:91–115.
- [25] Deardorff, J. (1974). Three-dimensional numerical study of the height and mean structure of a heated planetary boundary layer. *Boundary-Layer Meteorology*, 7(1):81–106.
- [26] Deardorff, J., Willis, G., and Lilly, D. (1969). Laboratory investigation of non-steady penetrative convection. *Journal of Fluid Mechanics*, 35(01):7–31.
- [27] Eidson, T. M. (1985). Numerical simulation of the turbulent rayleighbnard problem using subgrid modelling. *Journal of Fluid Mechanics*, 158:245–268.
- [28] Grotzbach, G. (1982). Direct numerical simulation of laminar and turbulent benard convection. *J. Fluid Mech*, 119:27–53.
- [29] Gulliver, J. and Halverson, M. (1989). Air-water gas transfer in open channels. *Water Resources Research WREDAQ Vol. 25*, (8):1783–1794.
- [30] Handler, R., Saylor, J., Leighton, R., and Rovelstad, A. (1999). Transport of a passive scalar at a shear-free boundary in fully developed turbulent open channel flow. *PHYSICS OF FLUIDS*, 11(9).
- [31] Harriott, P. (1962). A random eddy modification of the penetration theory. *Chemical Engineering Science*, 17(3):149–154.
- [32] Harten, A., Engquist, B., Osher, S., and Chakravarthy, S. (1987). Uniformly high-order accurate essentially nonoscillatory schemes. *J. Comput. Phys.*, 71(2):231–303.

-
- [33] Harvey, A., Kaplan, S., and Burnett, J. (2005). Effect of dissolved air on the density and refractive index of water. *International Journal of Thermophysics*, 26(5):1495–1514.
- [34] Hasegawa, Y. and Kasagi, N. (2008). Systematic analysis of high schmidt number turbulent mass transfer across clean, contaminated and solid interfaces. *Int. J. of Heat and Fluid Flow*, 29(3):765–773.
- [35] Hasegawa, Y. and Kasagi, N. (2009). Hybrid dns/les of high schmidt number mass transfer across turbulent air-water interface. *Int. J. of Heat and Fluid Flow*, 52(3-4):1012–1022.
- [36] Haußecker, H., Reinelt, S., and Jähne, B. (1995). Heat as a proxy tracer for gas exchange measurements in the field: Principles and technical realization. *Air-Water Gas Transfer*, pages 405–413.
- [37] Henrick, A., Aslam, T., and Powers, J. (2005). Mapped weighted-essentially-non-oscillatory schemes: achieving optimal order near critical points. *J. Comput. Phys.*, 207(1):542–567.
- [38] Herlina (2005). *Gas Transfer at the Air-Water Interface in a Turbulent Flow Environment*. Universitaetsverlag Karlsruhe, ISBN 3-937300-74-0.
- [39] Herlina and Jirka, G. H. (2004). Application of lif to investigate gas transfer near the air-water interface in a grid-stirred tank. *Experiments in Fluids*, 37:341–349. 10.1007/s00348-004-0822-2.
- [40] Herlina, H. and Wissink, J. (2014). Direct numerical simulation of turbulent scalar transport across a flat surface. *Journal of Fluid Mechanics*, 744:217–249.
- [41] Herring, J. and Wyngaard, J. (1985). Convection with a simple chemically reactive passive scalar. In *5th Symposium on Turbulent Shear Flows*, volume 1, page 10.
- [42] Higbie, R. (1935). *The rate of absorption of a pure gas into still liquid during short periods of exposure*. THE UNIVERSITY OF MICHIGAN.

-
- [43] Jähne, B., Münnich, K., Dutzi, R., Huber, W., and Libner, P. (1987). On the parameters influencing air-water gas exchange. *Journal of Geophysical research*, 92(C2):1937–1949.
- [44] Jahne, B., Münnich, K., and Siegenthaler, U. (1979). Measurements of gas exchange and momentum transfer in a circular wind-water tunnel. *Tellus*, 31(4):321–329.
- [45] Jirka, G. et al. (2008). Experiments on gas transfer at the air–water interface induced by oscillating grid turbulence. *Journal of Fluid Mechanics*, 594(1):183–208.
- [46] Jirka, G., Herlina, H., and Niepelt, A. (2010). Gas transfer at the air-water interface: experiments with different turbulence forcing mechanisms. *Experiments in Fluids*, 49(1):319–327.
- [47] Jirka, G. and Ho, A. (1990). Measurements of gas concentration fluctuations at water surface. *Journal of Hydraulic Engineering*, 116(6):835–847.
- [48] Johnsen, E. and Colonius, T. (2006). Implementation of weno schemes in compressible multicomponent flow problems. *J. Comput. Phys.*, 219(2):715–732.
- [49] Jonas, T., Stips, A., Eugster, W., and Wüest, A. (2003). Observations of a quasi shear-free lacustrine convective boundary layer: Stratification and its implications on turbulence. *Journal of geophysical research*, 108(C10):3328.
- [50] Katsaros, K., Liu, W., Businger, J., and Tillman, J. (1977). Heat transport and thermal structure in the interfacial boundary layer measured in an open tank of water in turbulent free convection. *J. Fluid Mech*, 83(2):311–335.
- [51] Kawamura, H., Ohsaka, K., Abe, H., and Yamamoto, K. (1998). Dns of turbulent heat transfer in channel flow with low to medium-high prandtl number fluid. *International Journal of Heat and Fluid Flow*, 19(5):482 – 491.
- [52] Kerr, R. and Herring, J. (2000). Prandtl number dependence of nusselt number in direct numerical simulations. *Journal of Fluid Mechanics*, 419:325–344.

-
- [53] Kerr, R. M. (1996). Rayleigh number scaling in numerical convection. *Journal of Fluid Mechanics*, 310:139–179.
- [54] Komori, S., Nagaosa, R., Murakami, Y., Chiba, S., Ishii, K., and Kuwahara, K. (1993). Direct numerical simulation of three-dimensional open-channel flow with zero-shear gas–liquid interface. *Physics of Fluids A: Fluid Dynamics*, 5(1):115–125.
- [55] Kunugi, T., ichi Satake, S., and Ose, Y. (2001). Direct numerical simulation of carbon-dioxide gas absorption caused by turbulent free surface flow. *International Journal of Heat and Fluid Flow*, 22(3):245 – 251. `ice:titleTurbulent Heat and Mass Transfer - 3i/ce:titlei`.
- [56] Lakehal, D., Fulgosi, M., Yadigaroglu, G., and Banerjee, S. (2003). Direct numerical simulation of turbulent heat transfer across a mobile, sheared gas-liquid interface. *Journal of Heat Transfer*, 125(6):1129–1139.
- [57] Lee, M. (2002). Visualization of oxygen transfer across the air–water interface using a fluorescence oxygen visualization method. *Water research*, 36(8):2140–2146.
- [58] Lee, M. and Schladow, S. (2000). Visualization of oxygen concentration in water bodies using a fluorescence technique. *Water Research*, 34(10):2842–2845.
- [59] Lewis, W. and Whitman, W. (1924). Principles of gas absorption. *Industrial & Engineering Chemistry*, 16(12):1215–1220.
- [60] Liss, P. and Slater, P. (1974). Flux of gases across the air-sea interface.
- [61] Liu, X., Osher, S., and Chan, T. (1994). Weighted essentially non-oscillatory schemes. *J. Comput. Phys.*, 115(1):200–212.
- [62] Lombardi, P., Angelis, V. D., and Banerjee, S. (1996). Direct numerical simulation of near-interface turbulence in coupled gas-liquid flow. *Physics of Fluids*, 8(6):1643–1665.
- [63] MAGNAUDET, J. and CALMET, I. (2006). Turbulent mass transfer through a flat shear-free surface. *Journal of Fluid Mechanics*, 553:155–185.

-
- [64] Martin, M., Taylor, E., Wu, M., and Weirs, V. (2006). A bandwidth-optimized weno scheme for effective direct numerical simulation of compressible turbulence. *J. Comput. Phys.*, 220(1):270–289.
- [65] McCreedy, M. J., Vassiliadou, E., and Hanratty, T. J. (1986). Computer simulation of turbulent mass transfer at a mobile interface. *AIChE Journal*, 32(7):1108–1115.
- [66] Moog, D. and Jirka, G. (1994). Macro-roughness effects on stream reaeration. pages 994–998.
- [67] Moog, D. and Jirka, G. (1999). Air-water gas transfer in uniform channel flow. *Journal of hydraulic engineering*, 125(1):3–10.
- [68] Moog, D. and Jirka, G. (2002). Air-water gas transfer in uniform flows with large gravel-bed roughness. *Geophysical Monograph Series*, 127:371–375.
- [69] Münsterer, T. (1996). *LIF Investigation of the Mechanisms: Controlling Air-water Mass Transfer at a Free Interface*. PhD thesis.
- [70] Münsterer, T. and Jähne, B. (1998). Lif measurements of concentration profiles in the aqueous mass boundary layer. *Experiments in Fluids*, 25(3):190–196.
- [71] Münsterer, T., Mayer, H., and Jähne, B. (1995). Dual-tracer measurements of concentration profiles in the aqueous mass boundary layer. In *Air-Water Gas Transfer: 3rd International Symposium on Air-Water Gas Transfer*, pages 637–648.
- [72] Na, Y., Papavassiliou, D. V., and Hanratty, T. J. (1999). Use of direct numerical simulation to study the effect of prandtl number on temperature fields. *International Journal of Heat and Fluid Flow*, 20(3):187 – 195.
- [73] Nagaosa, R. (1999). Direct numerical simulation of vortex structures and turbulent scalar transfer across a free surface in a fully developed turbulence. *Physics of Fluids*, 11(6):1581–1595.

-
- [74] Nagaosa, R. and Saito, T. (1997). Turbulence structure and scalar transfer in stratified freesurface flows. *AIChE Journal*, 43(10):2393–2404.
- [75] O’Connor, D. and Dobbins, W. (1956). The mechanism of reaeration in streams. *J. sanit. Engng. Div., Am. Soc. civ. Engrs, SA*, 6:1–30.
- [76] Piller, M., Nobile, E., and Hanratty, T. (2002). Dns study of turbulent transport at low prandtl numbers in a channel flow. *Journal of Fluid Mechanics*, 458(1):419–441.
- [77] Sander, J., Simon, A., Jonas, T., and Wüest, A. (2000). Surface turbulence in natural waters: A comparison of large eddy simulations with microstructure observations. *Journal of Geophysical Research. C. Oceans*, 105:1195–1207.
- [78] Schladow, S., Lee, M., Hürzeler, B., and Kelly, P. (2002). Oxygen transfer across the air-water interface by natural convection in lakes. *Limnol. Oceanogr.*, 47(5):1394–1404.
- [79] Schwertfirm, F. and Manhart, M. (2007). Dns of passive scalar transport in turbulent channel flow at high schmidt numbers. *Int. J. of Heat and Fluid Flow*, 28(6):1204–1214.
- [80] Schwertfirm, F., Mathew, J., and Manhart, M. (2008). Improving spatial resolution characteristics of finite difference and finite volume schemes by approximate deconvolution pre-processing. *Computers and Fluids*, 37(9):1092–1102.
- [81] Shu, C.-W. and Jiang, G. (1996). Efficient implementation of weighted eno schemes. *J. Comput. Phys.*, 126(1):202–228.
- [82] Shu, C.-W. and Osher, S. (1988). Efficient implementation of essentially non-oscillatory shock-capturing schemes. *J. Comput. Phys.*, 77(1):439–471.
- [83] Smith, W. R. and Wissink, J. G. (2012). Parameterization of travelling waves in plane poiseuille flow. *IMA Journal of Applied Mathematics*, page hxs037.
- [84] Soloviev, A. and Schlüssel, P. (1996). Evolution of cool skin and direct air-sea gas transfer coefficient during daytime. *Boundary-Layer Meteorology*, 77(1):45–68.

-
- [85] Spangenberg, W. and Rowland, W. (1961). Convective circulation in water induced by evaporative cooling. *Physics of Fluids*, 4(6):743–750.
- [86] Suga, K. and Kubo, M. (2010). Modelling turbulent high schmidt number mass transfer across undeformable gasliquid interfaces. *International Journal of Heat and Mass Transfer*, 53(1516):2989 – 2995.
- [87] Takehara, K. and Etoh, G. (2002). A direct visualization method of co2 gas transfer at water surface driven by wind waves. *Geophysical Monograph Series*, 127:89–95.
- [88] Thackston, E. and Krenkel, P. (1969). Reaeration prediction in natural streams. *J. Sanitary Engrg. Div. Proc. ASCE 95(SA1)*, pages 65–93.
- [89] Thomson, J. (1882). On a changing tessellated structure in certain liquids. *Proc. Phil. Soc. Glasgow*, 13:464–468.
- [90] Toepler, A. (1864). *Beobachtungen nach Einer Nueun Optischen Methode*. M. Cohen and Son Pub.
- [91] Vaughan, W. and Weber, G. (1970). Oxygen quenching of pyrenebutyric acid fluorescence in water. a dynamic probe of the microenvironment. *Biochem.*, 9(3):464–473.
- [92] Verzicco, R. and Camussi, R. (1997). Transitional regimes of low-prandtl thermal convection in a cylindrical cell. *Physics of Fluids*, 9:1287.
- [93] Verzicco, R. and Camussi, R. (1999). Prandtl number effects in convective turbulence. *Journal of Fluid Mechanics*, 383:55–73.
- [94] Verzicco, R. and Camussi, R. (2003). Numerical experiments on strongly turbulent thermal convection in a slender cylindrical cell. *Journal of Fluid Mechanics*, 477:19–49.
- [95] Wang, L. and Lu, X. (2005). Large eddy simulation of stably stratified turbulent open channel flows with low-to high-prandtl number. *International journal of heat and mass transfer*, 48(10):1883–1897.

- [96] Wissink, J. (2004). On unconditional conservation of kinetic energy by finite-difference discretizations of the linear and non-linear convection equation. *Computers and Fluids*, 33(2):315–343.
- [97] Wolff, L. and Hanratty, T. (1994). Instantaneous concentration profiles of oxygen accompanying absorption in a stratified flow. *Experiments in fluids*, 16(6):385–392.
- [98] Wolff, L., Liu, Z., and Hanratty, T. (1991). A fluorescence technique to measure concentration gradients near an interface. In *Air-Water Mass Transfer*, pages 210–218. ASCE.
- [99] Woodrow Jr, P. and Duke, S. (2002). Lif measurements of oxygen concentration gradients along flat and wavy air-water interfaces. *Geophysical Monograph Series*, 127:83–88.
- [100] Zeytounian, R. K. (2003). Joseph boussinesq and his approximation: a contemporary view. *Comptes Rendus Mcanique*, 331(8):575 – 586.